Sensitivity of glacial isostatic adjustment induced rotational changes to the ice-load history

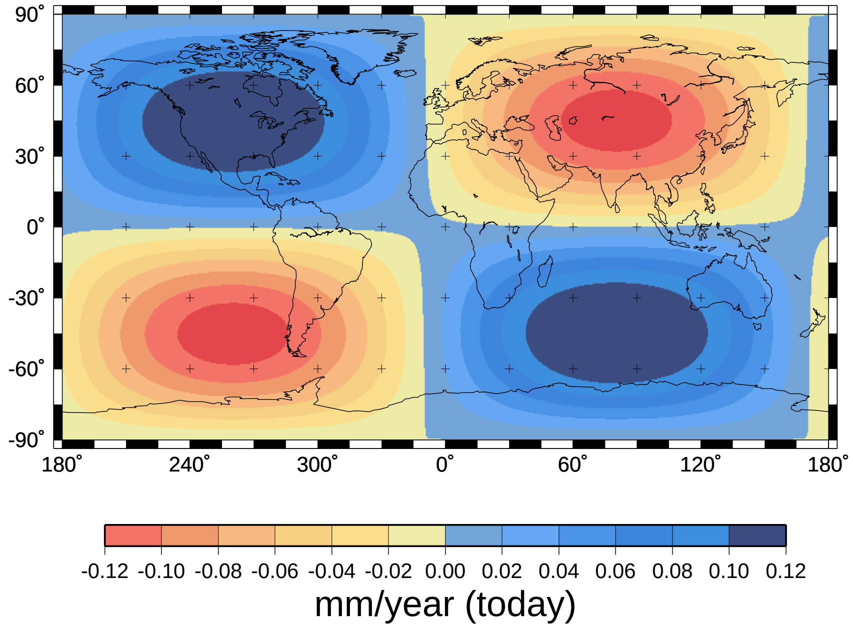

N.G. van Dael

TUDelft
Delft University of Technology

Sensitivity of glacial isostatic adjustment induced rotational changes to the ice-load history

N.G. van Dael

Delft, 7 December 2006

Astrodynamics & Satellite Systems
Faculty of Aerospace Engineering
Delft University of Technology
Kluyverweg 1, 2629 HS Delft
The Netherlands

Astrodynamics &
Satellite systems

Preface

The research I present in this thesis forms the concluding task of the Master of Science program of Aerospace Engineering at the Delft University of Technology. This master thesis work was carried out at the chair of Astrodynamics and Satellite Systems within the Department of Earth Observation and Space systems (DEOS) at the faculty of Aerospace Engineering. This project was done on individual basis, but it could not be completed successfully without the help of others. So I would like to acknowledge the following persons.

I would like to thank Dr. Jan Hagedoorn of GeoForschungsZentrum Potsdam for doing the benchmark on moments of inertia and the frequent correspondence which was necessary for completing this successfully. Special thanks go to Dr. Glenn Milne of Durham University for taking the effort of doing the first steps of the benchmark of the whole sea level code on a rotating Earth, which was unfortunately more tricky and time-consuming then we initially thought. I am also grateful to Dr. Jerry Mitrovica of the University of Toronto for answering questions elaborately and mostly on very short notice. But most of all I am grateful to my supervisors; Dr. Bert Vermeersen who was always there to guide me in the right way and Ir. Hugo Schotman for the clarifying discussions and for preventing me in comparing apples with peers.

I want to thank the students on the ninth floor whos companionship and humor contributed much to the pleasure of working on the thesis. I would also like to thank my family and housemates for all the support and sincere interest in my work. Finally, I thank all those who are not mentioned here, but who supported me during my research in any other way.

Delft, December 2006
Niek van Dael

Abstract

Since the planet Earth was formed, about 4.5 billion years ago, it has always been a complex and dynamic system due to internal and external forces. Examples of the manifestation of these forces on the surface of the Earth are tsunami's in South-East Asia (2004) and earthquakes in Pakistan (2005), continental drift and glacial isostatic adjustment (GIA) in the Baltic sea (Scandinavia). GIA is the response of the Earth due to growth and melting of ice sheets and is known to have effect on the orientation of the Earth rotation vector in both the direction and rotation rate. The perturbations due to changes in the orientation of the rotation vector has, in parts of the world further away from the formerly glaciated areas, a non-negligible contribution to the relative sea level and can not be neglected. This contribution can reach up to 0.14 mm/year for present-day relative sea level change where the rotational induced signal is a maximum.

In this study the effect of GIA induced change in the rotation vector is implemented self-consistently in an existing model that solves the sea level equation using a pseudo-spectral method on a spherically symmetric, incompressible, Maxwell-viscoelastic Earth model. This model is used to perform a sensitivity analysis of different ice-load histories and GIA induced rotational changes. The selected ice-load histories are the much used ICE-3G ice model and the more recently developed ICE-5G and RSES ice models. In the following step the prediction of the rotation observables are tested against the rotation observations in the hotspot reference frame.

All the ice models give a distinct rotation signal which differ with the rotational observations in the hotspot reference frame. The ICE-3G ice model has a difference of 20 percent with respect to the rotational observations, the RSES ice model shows a relative small discrepancy of about 10 percent and the ICE-5G model has a larger difference of 60 percent. This difference is most likely caused by the fact that compressibility effects are not taken into account, other forcings than GIA are neglected and possible recent deglaciation events are not included. Further the use of recently developed ice models and the hotspot reference frame has a significant effect on the results and conclusions of older mantle inversion research. For most mantle inversion studies this will result in a viscosity stratification with a lower lower mantle viscosity, which can have a difference of 20 to 40 percent.

Contents

Chapter 1

Introduction

Since the planet Earth was formed, about 4.5 billion years ago, it has always been a complex and dynamic system due to internal and external forces. Examples of the manifestation of these forces on the surface of the Earth are tsunami's in South-East Asia (2004) and earthquakes in Pakistan (2005), continental drift and postglacial rebound in the Baltic sea (Scandinavia) and Hudson bay (Canada). Earth science is the all-embracing term of sciences related to the planet Earth which ultimately leads to a better understanding of the processes that shape the planet as it is today. The science that studies the Earth, its composition, structure, physical properties, history and the processes that shape it, is known as geology.

The mechanical flow properties of our planet (also called rheology) can be determined by examining geodynamic processes. These geodynamic processes act on different timescales, from seconds for earthquakes up to millions of years for mantle convection. On the intermediate timescale we will find processes like glacial isostatic adjustment (GIA), which is the response of the Earth to periods of glaciation and deglaciation. Information on the rheological properties of the Earth over short timescales comes mainly from seismic waves. From this information it is possible to derive a spherically symmetric Earth model which holds information on density and rigidity at different depths.

The information on rheological properties of the Earth over long and transient timescales is derived from the Earth's response to surface loading and unloading, for example GIA. By studying the GIA process it is possible to derive the viscosity of the Earth at different depths. GIA has also effect on both the rate and orientation of the rotation vector of the Earth. In effect, this changes the centrifugal part of the gravity potential of the Earth, which has an effect on predictions of present-day observables as radial and horizontal displacement rates and changes in geoid height[1]. The perturbations due to changes in the orientation of the rotation vector has, in parts of the world further away from the uplifting areas, a non-negligible contribution to the observables and have to be taken into account when GIA is studied. So when the changes in the rotation are taken into account it is possible to derive a more accurate sea level distribution. But the changes in the orientation of the rotation vector can also be used to constrain the radial mantle viscosity profile of the Earth as result of the high correlation with the lower mantle viscosity which has been done frequently in the last decades.

In this study the GIA induced changes in the rotation vector will be implemented in an existing FORTRAN code that solves the sea level equation, based on the study of *Mitrovica and Peltier* [1991]. This will be done self-consistently, i.e. the effect on the potential field of the induced changes in the rotation vector has to be taken into account in the computation of the induced changes, as described in [*Milne and Mitrovica*, 1998]. This model will be used to perform a sensitivity analysis of different ice-load histories on GIA induced rotational changes. The selected ice-load histories are the much used ICE-3G ice model and the more recent ICE-5G and RSES ice models. The prediction

---

[1] the geoid is an equipotential surface that coincides with the mean ocean surface

of the rotation observables are subsequently tested against the rotational observations in the hotspot reference frame. Further this model will be used to investigate the effect of recent improvements on the results and conclusions of older research concerning the inference of mantle viscosity.

The structure of this report will be as follows. In chapter 2 an introduction to Earth rotation and GIA is given and in chapter 3 a mathematical model of the response of the Earth to ice age cycles is derived. Using these results, the sea level equation of a non-rotating Earth is determined in chapter 4, followed by a discussion on the Earth rotation theory and its implementation in the sea level equation in chapter 5. The input with respect to Earth- and ice models that are used in the simulations are given in chapter 6. The rotational behaviour of the Earth and the effect of different ice models will be treated in chapter 7. Finally in chapter 8 the conclusions and recommendations will be given.

Chapter 2

Earth rotation and Glacial Isostatic Adjustment

The rotation of the Earth is not regular and changes both in the position of the axis and rotation rate. These irregularities are caused by different internal and external forces over a wide range of time-scales. The most dominant forcing is glacial isostatic adjustment (GIA) which is the response of the Earth's shape and gravitational field to surface ice-mass loads. In section 2.1 the known motions of the rotation axis of the Earth will be presented, followed by a treatment of the GIA phenomenon in section 2.2.

2.1 Rotation of the Earth

The rotation of the Earth changes continuously and has elements of secular and periodic variation caused by numerous geophysical processes. This motion is complex and will be discussed in following section, followed by a review on the available observations of Earth rotation and a discussion on new developments in reference frames on which the the Earth rotation observations are evaluated.

2.1.1 Motions of the Earth's rotation axis

The position of the rotation axis changes on timescales that range from days to millions of years and can be divided into two main categories: displacement of the axis of rotation with respect to the fixed stars and a displacement of the axis of rotation with respect to a fixed position on the Earth's surface.

Displacements of the axis of rotation with respect to the fixed stars are e.g. precession and nutation. These displacements are the result of external forces like the gravitational interactions between the Earth and different celestial bodies in our solar system. The most dominant external forces are the gravitational torques of the Moon and Sun exerted on the spinning Earth's equatorial bulge[1]. Precession generally refers to the slow motion with a period of around 26,000 years and nutation is a small nodding motion with a period of 18.6 years and an amplitude of 284 m as depicted in figure 2.1.

Displacements of the axis of rotation with respect to a fixed position on the Earth's surface are the secular and periodic polar motion (see figure 2.2). These displacements are due to mass displacements in the interior of the Earth, at its surface and in the hydro- and atmosphere.

---

[1] ellipsoidal of the Earth as a result of flattening

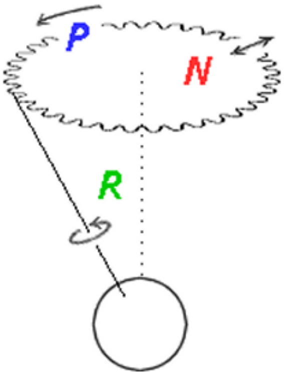

Figure 2.1 Precession (P), nutation (N) and rotation (R) of a rotating body.

Three periodic variations can be distinguished, namely an annual, Chandler and Markowitz wobble:

- the annual wobble is about 5 m per year with respect to the crust and is caused by seasonally varying winds.
- the Chandler wobble is the (Eulerian) free precession for a viscoelastic body with an average amplitude of 10 m with respect to the crust and a period of 433 days (14 months). The causes of the Chandler wobble are still debated for. A study done by *Gross* [2000] states that 2/3 is caused by a fluctuating pressure on the bottom of the ocean and for 1/3 is caused by fluctuations in the atmospheric pressure. The fluctuating pressure on the bottom of the ocean is mainly the result of temperature and salinity changes and wind-driven changes in the circulation of the oceans.
- the Markowitz wobble is relatively small with an average amplitude of 1 m and period of approximately 30 years. The mechanism responsible to generate such a wobble is still not identified and under discussion [*Mound*, 2005].

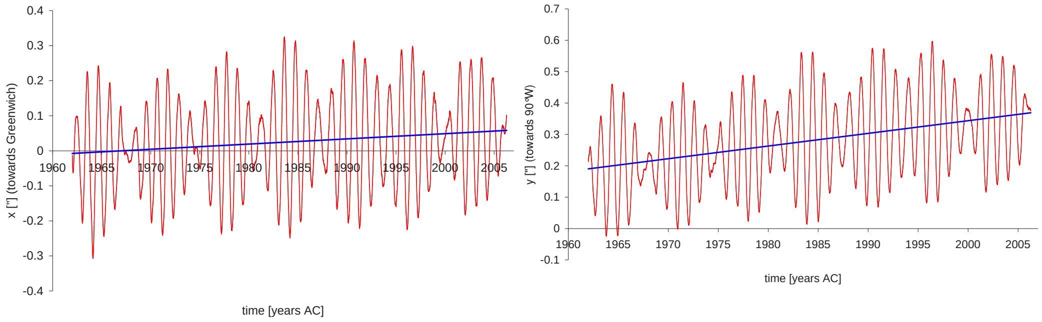

Figure 2.2 X (left) and y (right) component of observed polar motion from 1962 till March 2006 (1 " (arcsec) $\approx$ 31m). Periodic polar motion (red) and secular variation of polar motion (blue). Source: IERS.

The secular variation of polar motion is about 1 m per 10 year with respect to the crust and is believed to be the result of numerous causes: GIA, mantle convection, subducting slabs, mountain building, seismic activity (earthquakes), surface water fluctuations, groundwater storage variations and cryospheric changes. When polar motion is modeled using a reasonable Earth model and a forcing by the late-Pleistocene ice history it corresponds with the observed rotation rate and direction [*e.g.*, *Nakiboglu and Lambeck*, 1980; *Sabadini and Peltier*, 1981]. The direction of the secular variation of polar motion is about 79 °W and directed towards the Hudson's Bay region in Canada, which was the center of the largest Pleistocene ice sheet. The direction of the secular variation of polar motion suggests that the Pleistocene deglaciation causes the primary excitation, but it must be noted that there are other contributions. available observational data.

The rotation axis does not only change its position but also its rate of rotation, which has a direct effect on the length of day (LOD). The fluctuations in LOD occur on different time scales (see figure 2.3):

- short-time fluctuations (days till years) in LOD are the result of pressure distribution and zonal winds and are responsible for variations in the order of ms.
- decadal fluctuations (tens of years) are believed to be due to the transfer of angular momentum between the fluid core and solid mantle. This requires torque at the core mantle boundary and is possibly caused by a mechanism that generates pressure, inertial, topographic, viscous or electromagnetic coupling. These variations are in the order of 5-10 ms.
- a long-term secular trend which is mainly due to GIA and tidal exchange between the Earth and the Moon and the Earth and the Sun. Because the Earth is not perfectly elastic and the Earth is rotating faster around its axis then the Moon is rotating around the Earth this mechanism is responsible for a secular decrease in rotational velocity. Earth rotational observations show that 500 million years ago one year counted about 420 days and since then the LOD linearly increased with more or less 2 ms per century [*Lambeck*, 1980].

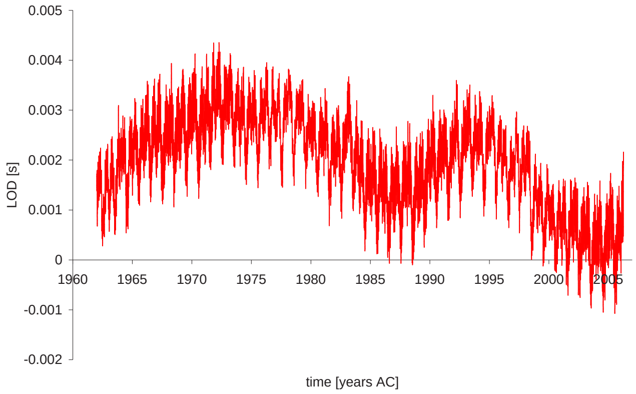

Figure 2.3 Observed LOD from 1962 till march 2006. Source: IERS.

2.1.2 Earth rotation observations

Throughout the ages the variable rotation of the Earth is recorded in several ways. There are generally three sources of information on the variable rotation, which depend on the time scale under consideration. The primary source is the record of about 150 year of observations collected by astronomers since the telescope was introduced till the use of satellites nowadays. Following the discovery of the Chandler wobble in 1891 the International Latitude Service (ILS) was established to observe the motion of the Earth's rotation pole, which was later superseded by the International Earth Rotation Service (IERS). The ILS used six observing stations to make regular optical astrometric observations of the latitude variation from 1899 till 1979. The error, introduced in the process of cataloging the stars, was decreased through the introduction of the Hipparcos star catalog, named after the Hipparcos astrometric satellite launched in 1989. Nowadays the Earth's orientation can also be obtained from various space-geodetic techniques including Lunar Laser Ranging (LLR), Satellite Laser Ranging (SLR), Global Positioning System (GPS), Doppler Orbit determination and Radiopositioning Integrated on Satellite (DORIS) and Very Long Baseline Interferometry (VLBI). The permanent monitoring of the Earth's rotation requires the coordinated use of VLBI and satellite techniques. VLBI provides the absolute reference for the determination of universal time, precession and nutation. The satellite techniques (LLR, SLR, GPS) provide the daily interpolation and the short-term prediction of universal time in the highly accurate but less frequent VLBI reference values. The combination of all the independent space-geodetic Earth orientation measurements is gathered in SPACE96 [*Gross*, 1997] and the more recent SPACE2001 [*Gross*, 2002]. Figure 2.4 shows the data of three polar motion series.

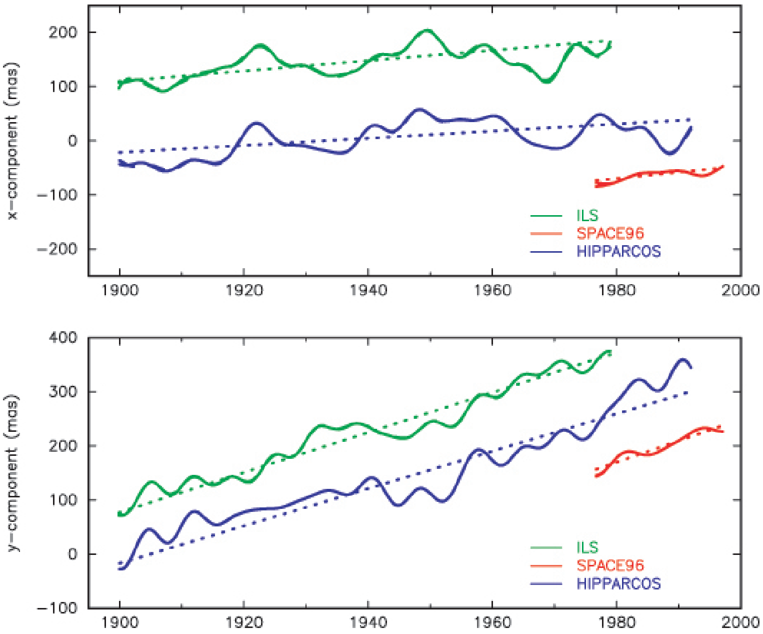

Figure 2.4 x and y component of different smoothed polar motion series. The x-component is defined positive towards Greenwich meridian and the y-component is defined positive towards 90 °E and the values are given in milliarcseconds (mas). For clarity the ILS series have been shifted up by 100 mas and the SPACE96 series have been shifted down by 100 mas [*Gross and Vondrák*, 1999].

Secondly historical records from old cultures are used which date back to 1000 BC and earlier. These records contain observations of eclipses, conjunctions and other configurations of celestial bodies. These observations are used to investigate the LOD.
Thirdly fossil records are used to estimate respectively the position of the rotation axis and the rotation rate during the geological past. Fossil records (e.g. corals, molluscs and stromalites) contain information on daily and seasonal variations which can be linked directly to the changing rotation. This information can be retrieved by analyzing their physical and chemical properties of different layers or growth marks.

2.1.3 Reference frame

Estimates of the polar motion over the past century usually neglect plate motions or are relative to the mean lithosphere. The secular shift of the rotation axis with respect to the plate it points through is also called apparent polar wander (APW) and the secular shift of the rotation axis with respect a mean lithosphere or mean lower mantle is called true polar wander (TPW). Early observations from ILS were not corrected for plate motion [*e.g., McCarthy and Luzum*, 1996; *Gross and Vondrák*, 1999]. But to interpret observations of the polar motion correctly it has to be considered relative to the mean solid Earth and plate motions need to be taken into account. Also the mean lithosphere is not a good reference frame because it still moves relative to the solid Earth. One solution is to link the reference frame of the solid Earth to the lower mantle instead of the lithosphere, because the lower mantle comprises 2/3 of the solid Earth's volume. *Argus and Gross* [2004] suggest to use the hotspot-reference frame because hotspots are thought to originate in and move slowly relative to the lower mantle [*Steinberger and O'Connell*, 1998; *Steinberger*, 1998]. Hotspots are rather concentrated pointlike places on the Earth's surface which show a higher surface heat flow than the average value and often pours out large quantities of basaltic rock. It is generally thought that these hotspots are associated with rising plumes of hot material originating from the mantle. When the plates of the Earth move with respect to the mantle, a track of basaltic rock outpourings will remain and create for example the Hawaiian Ridge. When the hotspot reference frame together with the Hipparcos star catalog is used the direction of the secular variation of polar motion will change 11 ° counterclockwise and the spin axis motion will differ 15% as can been seen in table 2.1. The change in direction of the secular variation of polar motion can be seen in figure 2.5. If the secular shift of the rotation axis with respect to the deep mantle is considered, the motion is referred to as true polar wander (TPW).

model	ILS		Hipparcos	
	speed $[^\circ Myr^{-1}]$	path [longitude °W]	speed $[^\circ Myr^{-1}]$	path [longitude °W]
uncorrected for plate motion[1]	0.92	75.0	-	-
uncorrected for plate motion[2]	1.06	75.5	-	-
mean lithosphere[2]	0.98	79.9	0.98	79.2
hotspots[3]	1.12	69.1	1.12	68.4

Table 2.1 Estimates of the motion of the spin axis over the past century. Source: 1) *McCarthy and Luzum* [1996], 2) *Gross and Vondrák* [1999], 3) *Argus and Gross* [2004].

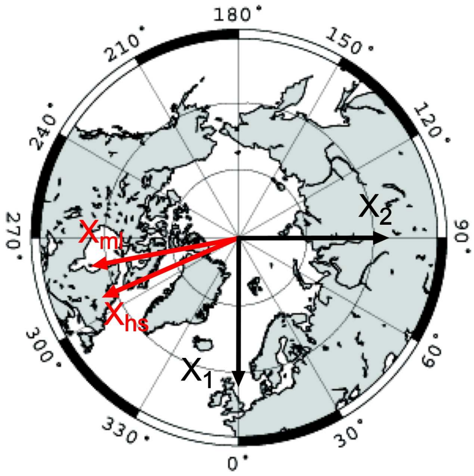

Figure 2.5 secular variation of polar motion. Where X_1 is the axis aligned with the Greenwich longitude, X_2 is the axis in the direction of $90\,^\circ E$ of X_1, X_{ml} is the spin axis motion relative to the mean lithosphere and X_{hs} is the spin axis motion relative to the hotspots.

2.2 Glacial isostatic adjustment

In the global process of GIA the Earth's shape and gravitational field are modified in response to the large scale changes in surface mass load as result of the ice ages. It is commonly used to give more insight in the viscosity structure of the Earth. There is a large interest in studying the response of the planet to these ice ages because of the geological, geophysical and astronomical data which record them are of high quality. These data are capable of providing constraints upon the viscoelastic properties of the interior of the Earth. In this section first the mechanism of glacial isostatic adjustment is discussed followed by a more detailed discussion on the elements that determine the behaviour of GIA, namely the ice ages and the structure and composition of the Earth.

2.2.1 Mechanism of glacial isostatic adjustment

GIA is an important forcing mechanism in case of TPW and will be the only mechanism considered in this study. The term isostasy was first mentioned by Dutton in 1889 to describe the compensated state of the Earth's topography. This idea was already suggested by Pratt and Airy in 1855 who used it to describe the compensation of mountains by unobservable roots. The term isostasy can also be interpreted as "the compensation of applied external surface loads (continental glaciers and ice sheets) by variations in Earth's external shape and internal density distribution" [*Peltier*, 2004]. Where this definition refers to a compensation steady state, glacial isostatic adjustment (GIA) is the dynamic process of elastic and viscous deformation to loading and unloading of the Earth by ice formation and removal. At the end of the nineteenth century observers began to relate the raised beaches in Scandinavia and the tilting of the Great Lake in Canada to GIA, and it was realized that viscous flow must occur in the mantle of the Earth. Already in the 1930's viscosity estimates for the mantle were produced using simple shorelines, and later on estimates for the relaxation time were made [*Lambeck*, 1988]. Nowadays GIA still accounts for a maximum uplift at the center of the former glaciated areas of about 1 cm per year for Scandinavia and up to 2 cm per year for Canada [*Milne et al.*, 2001].

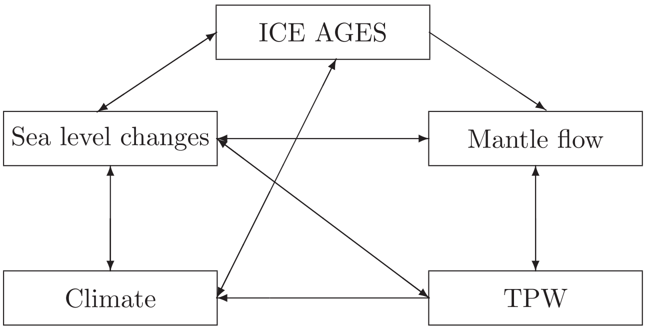

Figure 2.6 Simplified interaction between different components of GIA.

The growing and melting of ice sheets is part of a complex geophysical system that involves sea level, climate and wander of the rotation axis with respect to the Earth's surface. The changing ice sheets do not only have local effects, like the warping and tilting of land underneath and around it, but also global effects. These global effects are caused by the redistribution of mass, e.g. sea level and mantle flow. The melting of the ice also has indirect effects, because the water salinity and temperature and wind changes the ocean circulation, transfer of heat and moisture, and thus the climate. The changing climate and sea level on its turn affect the dynamics of the ice sheets and ice topography which influences mantle flow. This redistribution of mass under and on the surface of the Earth changes the moments of inertia of the Earth, which change the inertia tensor. The change in inertia tensor results in a movement of Earth's rotation pole with respect to mean solid Earth (TPW) and a change in the length of a day (rate of rotation). The change in Earth rotation affects both the sea level and climate again (see figure 2.6).

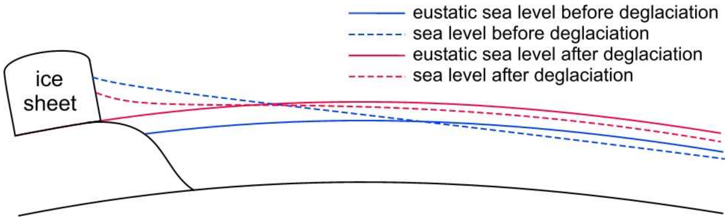

Figure 2.7 Schemetic drawing of the effect of self-gravitation on sea level.

The melted ice is not equally (eustatically) distributed over the oceans. This is the result of the physical property that mass attracts other masses around it, see figure 2.7. This effect is called self-gravitation and has to be taken into account. The following example illustrates the effect of self-gravitation on sea level rise: if all the Greenland ice were concentrated on the southern tip of Greenland and were to melt, then the effect of self-gravitation would cause a sea level drop at the coast of Iceland, a smaller than eustatic rise at the coast near New York and a larger than eustatic rise at the coast of Australia [*Sabadini and Vermeersen*, 2004].

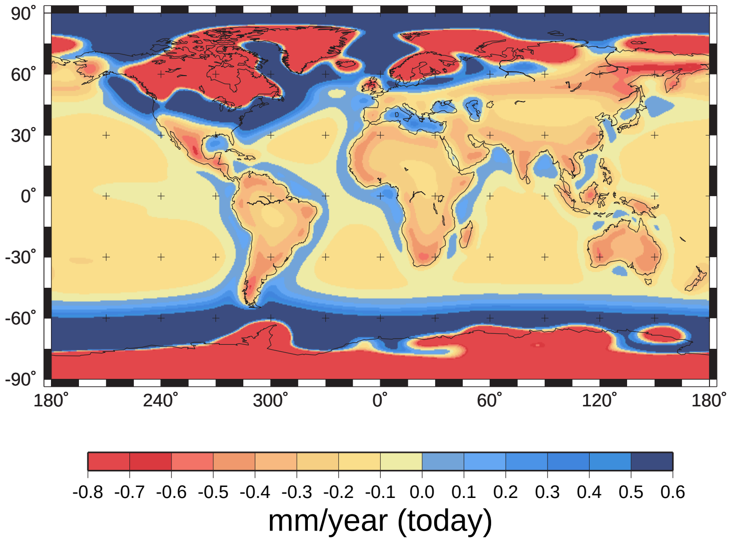

Figure 2.8 Global predictions of the present-day rate of change of relative sea level for a non-rotating Earth.

When an ice sheet melts this results in a eustatic sea level rise but also complex processes take place as seen in figure 2.8. It must be noted here that the present-day relative sea level, which is defined as the difference between the solid Earth and geoid, is also defined on land. Some of these distinct processes can be globally divided in near- and far field effects, which will be discussed below.

Near field GIA effects

In the near field (areas surrounding melting ice sheets) two effects can be distinguished that are mainly dominated by the radial response of the solid Earth. First of all there is a large postglacial relative sea level fall near the melting ice sheets. This is the result of the upward radial response of the sea floor due to the melting of the ice (rebounding effect) and the decreasing effect of self-gravitation. This postglacial relative sea level fall is bigger than the present-day sea level rise as result of the melting of the ice sheets and results in a present-day relative sea level fall of 1 to 2 cm a year as can be seen in figure

2.9 at (1). It must be noted that figure 2.9 is a simplified representation and the effects of self-gravitation and deformation have to be taken into account to obtain a more realistic picture. Secondly, some distance further away from the melting ice sheets there is a clear postglacial relative sea level rise, which is the consequence of the decreasing effect of self-gravitation and due to the subsidence of the peripheral bulges[2] that result in a downward radial response of the solid Earth. Together with the present-day sea level rise this results in a relative sea level rise with a maximum present-day value of 5 mm per year as can be seen in figure 2.9 at (2).

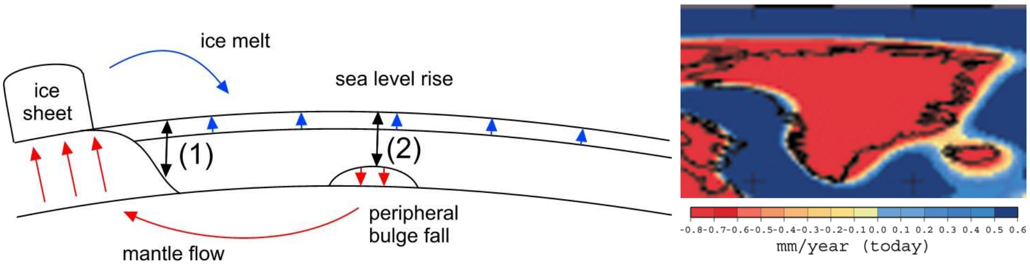

Figure 2.9 Near field GIA effects. Left: schematic drawing of the near field effects without self-gravitation and deformation effects. Right: present-day rate of change of relative sea level and near field effects at Greenland.

Far field GIA effects

In the far field (near continents and on the oceans) also two effects can be distinguished. First there is a relative postglacial sea level fall on the oceans, presently smaller than 1 mm per year, which is the result of the movement of ocean mass to the regions vacated by the subsiding peripheral bulges. This leads to a subsidence of the geoid and to a postglacial relative sea level fall greater than the relative sea level rise due to the present-day melting of ice. This process has also been called ocean syphoning [*Mitrovica et al.*, 2001] and is explained in figure 2.10.

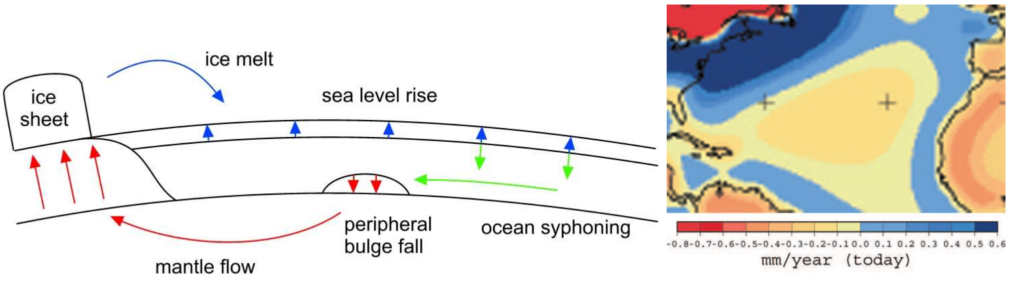

Figure 2.10 Far field GIA effects. Left: schematic drawing of ocean syphoning without self-gravitation and deformation effects. Right: present-day rate of change of relative sea level and ocean syphoning effect at the Atlantic Ocean.

Secondly, due to the offshore present-day relative sea level rise near continents and subsequent increased sea-load, the continent is levered which gives an offshore region of relative sea level rise of smaller than 1 mm per year and an onshore region of relative sea level fall of more than 1 mm per year. This phenomenon is known as continental levering [*Mitrovica et al.*, 2001], see figure 2.11.

The geodynamic timescale of GIA processes (10^3 - 10^5 years) is intermediate between the short timescales of seismic activity, Earth tides and rotation period (10^{-3} - 10^1 years) and the long timescales of mantle convection and other tectonic processes (10^6 - 10^8 years). The short timescales refer to a high frequency elastic response of the Earth and the long timescales to a low frequency viscous response of the Earth. Because

---

[2] rings of mantle material around an ice sheet formed during the growing of the ice sheet which introduced a flow of mantle material from beneath the ice sheet

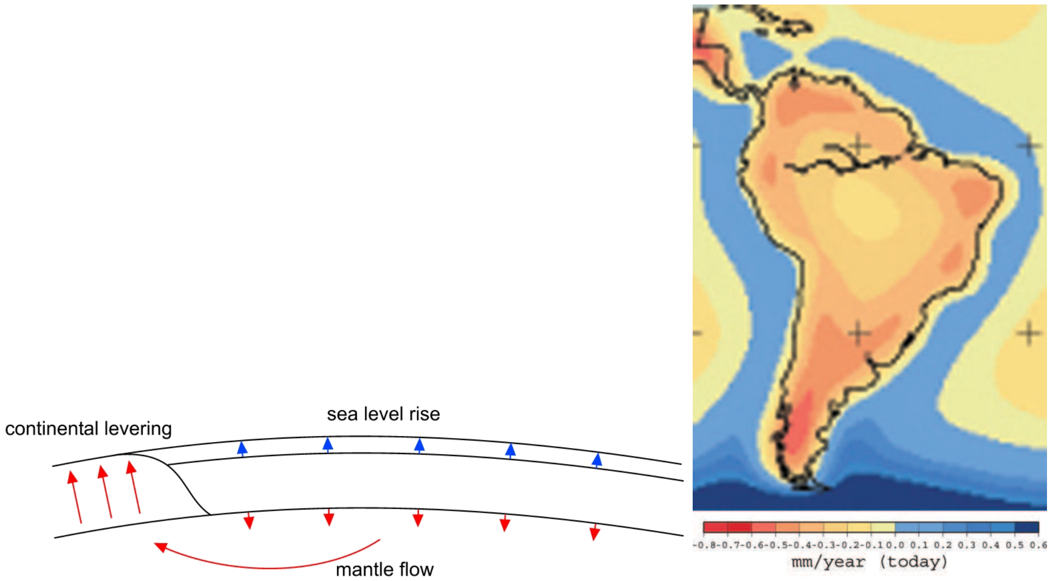

Figure 2.11 Far field GIA effects without self-gravitation and deformation effects. Left: schematic drawing of continental levering. Right: present-day rate of change of relative sea level and continental levering at South America.

the geodynamic timescale of GIA is intermediate it is also referred to as a (transient) viscoelastic response. From the GIA process the response of the Earth to a surface load can be determined. If the response of the Earth can be put into a model and the glacial history and sea level are considered known, it is possible to derive the internal properties of the Earth, in particular the viscosity. How the response of the Earth to a surface load is integrated into a mathematical model will be discussed in the next chapter. The response of GIA is dependent on loading during the ice ages and the structure and composition of the Earth. These will be treated in the next section.

2.2.2 Ice ages

The very existence of ice ages had been a long time unknown, until Bernard Kuhn in 1787 found the first evidence of glaciation in his research of boulders in the Swiss Jura. Numerous theories have been developed and until this date there is still a lot of controversy about them. The general consensus is that the ice ages are caused by a combination of four factors: change in atmospheric composition (CO_2 and methane), changes in the Earth's orbit around the sun (Milankovitch's theory), changes in the solar output, and the arrangement of continents [*Imbrie and Imbrie*, 1979]. Proof of ice ages can be found in different scientific disciplines: glaciology (ice cores), geology (marine and terrestrial sediments), biology (e.g. tree rings) and history (different kinds of records). This data can be used to create an ice model as will be discussed in section 6.2.

The earliest well-documented ice age, and probably the most severe of the last 1 billion years, occurred from 800 to 600 million years ago (the Cryogenian period) and it has been suggested that it produced a frozen Earth in which permanent sea ice extended to or very near the equator (http://en.wikipedia.org/wiki/Ice_age). A minor ice age occurred from 460 to 430 million years ago, during the Late Ordovician Period. There were extensive polar ice caps at intervals from 350 to 260 million years ago, during the Carboniferous and early Permian Periods. The present ice age began 40 million years ago with the growth of an ice sheet in Antarctica, but intensified during the Pleistocene (starting around 2 million years ago) with the spread of ice sheets in the Northern Hemisphere. Since then, the world has seen cycles of glaciation with ice sheets advancing and retreating on 40,000 and 100,000 year time scales. With the help of isotopes and ^{14}C radiocarbon dating of sea level data it is now generally known that the last glacial maximum occurred about 18,000 radiocarbon years (equivalent to 21,000 calendar years) ago [*Tushingham and Peltier*, 1991]. Between present day and the last glacial maximum a total ice mass of about 4.5×10^{19} kg has been melted, which led to an equivalent eustatic sea level rise of about 120 m. During this last glacial maximum (LGM) large parts of northern Europe, Asia and Canada were covered by large ice masses up to 3500 m high.

2.2.3 Structure and composition of the Earth

At the Earth's surface, oceans and mountains contribute to a diverse scenery but inside the Earth a dominant radial structure is present as a result of gravitation. The knowledge of the radial structure comes from indirect measurements, like the measurement of arrival times of seismic body waves and corresponding velocities. These body waves can be divided into two categories: pressure and shear. The velocity of the pressure waves is the highest of the two (5-13 km/s) and mostly dependent on the compressibility of the material. The velocity of the shear waves is lower than the pressure waves (2-7 km/s) and mostly dependent on the rigidity of the material. Finally the surface waves are the slowest but also cause the most damage on the surface of the Earth. After a seismic wave is triggered it can be measured by seismic stations directly and indirectly, because they are reflected at the boundaries between different layers of the Earth. By analyzing the travel time it is possible to determine the internal density profile of the Earth (figure 2.12). *Dziewonski and Anderson* [1981] derived the Preliminary Reference Earth Model (PREM), which contains a commonly applied radial variation of the elastic properties. To understand and explain geological processes two different concepts of layering for the outer part of the Earth are used: compositional layering (crust and mantle) and mechanical layering (lithosphere and asthenosphere). These concepts are explained in more detail below.

Crust and upper mantle
The crust is a thin layer with a diverse chemical composition which is positioned above the upper mantle. The crust has a clear distinction between continental and oceanic crust. The oceanic crust is created at the midoceanic ridges from rising mantle material and spreads out until it meets the continental plate and subducts beneath it at active margins. This is why the oceanic crust has an average age of 80 million years compared up to 2 billion years for continental crust [*Schubert et al.*, 2001]. The thickness of oceanic crust varies between roughly 2 km at the midoceanic ridge till 37 km in the direction of the continents and is composed of sediments and a volcanic layer with a rather uniform constitution of basaltic rock. The continental crust varies between 20 and 70 km (beneath mountains) and is thicker than the oceanic crust because it is not recycled into the Earth's interior. The continental crust contains more silicates than the oceanic crust and is therefore more deformable and has a lower density. The crust is separated from the upper mantle by the Mohorovicic (Moho) discontinuity at 19 km, which is a weighted average of continents and oceans. The Moho is characterized by an increase in seismic velocities. The Moho is marked as a chemical boundary because it represents a change in chemical composition between two layers. The upper mantle reaches until the seismic discontinuity at 670 km and can be split into a shallow upper mantle and a transition zone. The shallow upper mantle reaches until 400 km where a seismic discontinuity is present, which is the result of a phase change from the silicate olivine to wadsleyite. The transition zone is characterized by a sharp increase in density and reaches until the seismic discontinuity at 670 km.

Lithosphere and asthenosphere
The lithosphere is the rigid outer layer of the Earth and differs from the underlying asthenosphere in terms of its mechanical (or rheological) properties rather than its chemical composition. Under the influence of the low-intensity, long-term stresses the lithosphere responds practically as a rigid (elastic) shell while the asthenosphere behaves as a highly viscous fluid. The lithosphere includes the crust and the uppermost part of the upper mantle. Its thickness reaches from a few kilometers at midoceanic ridges and thickens to about 100 - 150 km under the older parts of ocean basins and up to 250 - 300 km under

continental areas. The asthenosphere includes the part immediately below the lithosphere until the viscosity increases again.

Lower mantle
The lower mantle begins at a depth of 670 km where a seismic discontinuity is present that is the result of a phase change from spinel to perovskite and magnesiowustite. Many geophysicists thought that the subducted lithospheric slabs were unable to penetrate across the discontinuity because of the lack of seismicity below it. They concluded that two chemically distinct layers were present and the boundary was referred to as a chemical boundary. More recent research [*e.g.*, *Hilst et al.*, 1997] indicates that some slabs are delayed at 670 km, but eventually sink into the lower mantle, which suggests that partly a phase change boundary is present. The lower mantle extends to the core-mantle boundary at a depth of 2900 km, but little is known of this boundary. A few hundred kilometers from the core-mantle boundary a sharp increase in seismic velocity is observed which is the result from the interaction between the core and mantle. This is called the D” layer which is interpreted as a hot boundary layer where heat is conducted from out of the core. Because of its steep thermal gradients it is thought that the D” layer plays an important role in the creation of mantle plumes.

Core
The outer core is found to be fluid because no shear waves propagate through it. The main constituents are molten iron and nickel, which by movement around the solid inner core drives the Earth’s magnetic field. The seismic boundary which separates the fluid outer core from the solid inner core is located at a depth of about 5200 km.

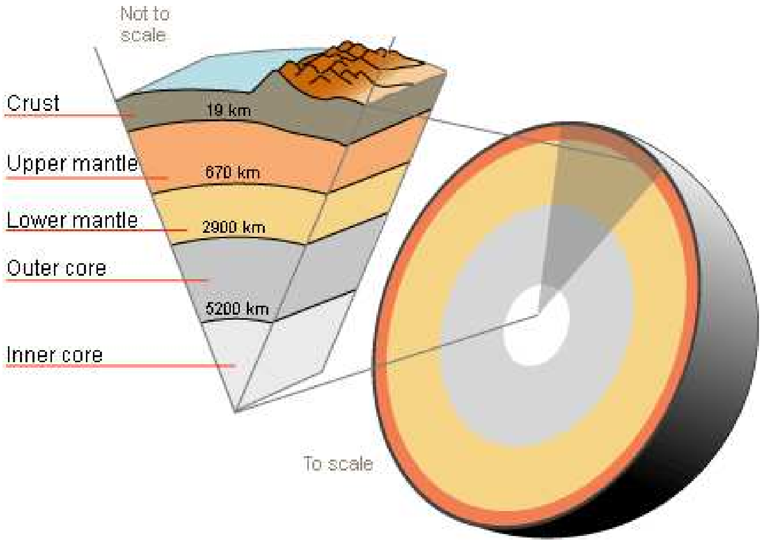

Figure 2.12 Compositional layering of a symmetric radial Earth model. Source: http://wikipedia.org/wiki/Earth’s_core.

Chapter 3

Rheology of the Earth

To simulate the effects of GIA, the response of the Earth to a surface load is integrated into a mathematical model. As mentioned before in the previous chapter, the geodynamic timescale of the GIA process is intermediate and in this case a viscoelastic response model is assumed. The behaviour of the viscoelastic response model will be studied using rheological models. In section 3.1 the response of a viscoelastic body is determined. Together with the equation of momentum and the Poisson equation this will form the basis of the normal-mode theory. The normal mode theory is a well known and commonly used theory to simulate the responses of a viscoelastic Earth to surface loads and is derived in the seventies and eighties by *Peltier* [1974; *Wu* [1978; *Wu and Peltier* [1982; *Sabadini et al.* [1982]. In section 3.2 the normal-mode theory will be derived for an incompressible, self-gravitating, spherically symmetric Earth model with a Maxwell-viscoelastic rheology.

3.1 Response models

In this section the response of a viscoelastic body is determined, but first the basic elastic and viscous response models will be derived in section 3.1.1 and 3.1.2. These models will be combined in a viscoelastic response model in section 3.1.3.

3.1.1 Elastic response model

The elasticity theory describes the immediate short term response (in the range of seconds to years) of materials. In this study the stress of elastic materials is considered linearly proportional to the strain and the material is fully recoverable. The behaviour can also be compared with a spring which is also fully recoverable after a load has been applied to it. The Earth materials of which the behaviour can be considered elastic are rocks at low pressure and temperature (e.g. in the lithosphere) and also materials in the mantle for stresses at seismic frequencies.

Now consider an infinitesimal cube with the sides oriented in the coordinate directions x_1, x_2, x_3. A component of the stress tensor σ_{ij} acts on the plane normal to the i-direction and in the j-direction. The normal stresses are the elements for which $i = j$ and the shear stresses are the elements for which $i \neq j$. The generalized form of Hooke's law for infinitesimal stress and strain is [*Ranalli*, 1995]:

$$\sigma_{ij} = \sum_{k=1}^{3} \sum_{\ell=1}^{3} C_{ijkl} \epsilon_{kl} \tag{3.1}$$

where σ_{ij} is the stress, C_{ijkl} the material constants tensor with the elastic properties of materials and ϵ_{kl} is the strain. Now assume that the material is homogeneous and isotropic, then the material constant tensor C_{ijkl} can be simplified to two independent coefficients. Then equation 3.1 will become:

$$\sigma_{ij} = \lambda \sum_{k=1}^{3} \epsilon_{kk}\delta_{ij} + 2\mu\epsilon_{ij} \tag{3.2}$$

where δ_{ij} is the Kronecker delta, λ and μ are the elastic material constants generally known as the *Lamé* parameters. The parameter μ is also known as the rigidity or shear modulus.

3.1.2 Viscous response model

The counterpart of the elasticity theory is the viscosity theory, which describes the long term response (in the range of thousands to billions of years) of materials. On large timescales solid materials can be considered as fluids and the behaviour can be compared to a dashpot. The Earth materials of which the behaviour can be considered viscous at longer geological timescales are in the mantle, below the lithosphere.

In a Newtonian fluid, where the strain rate is linearly proportional to the stress, the constitutive equations are given by [*Ranalli*, 1995]:

$$\sigma_{ij} = -p\delta_{ij} + C'_{ijkl}\dot{\epsilon}_{ij} \tag{3.3}$$

where p is the fluid pressure for the fluid at rest, C'_{ijkl} is the material constants tensor with the viscous properties of materials and $\dot{\epsilon}_{ij}$ is the strain rate. As in section 3.1.1 the tensor C'_{ijkl}, assuming isotropic bodies, can be reduced to two parameters which gives:

$$\sigma_{ij} = -p\delta_{ij} + \lambda'\dot{\theta}\delta_{ij} + 2\eta\dot{\epsilon}_{ij} \tag{3.4}$$

where λ' and η are the viscous material constants and η is referred to as the dynamic or Newtonian viscosity.

3.1.3 Viscoelastic response model

The elastic and viscous response models discussed in the last two sections will now be combined to a linear viscoelastic response model. For demonstration purposes one-dimensional and only shear components are taken into account (the full 3D viscoelastic response model is given in section 3.2. The linear elastic model for shear components is:

$$\sigma = 2\mu\epsilon \tag{3.5}$$

where μ is the rigidity. Now also assume a viscous model of a Newtonian body:

$$\sigma = 2\eta\dot{\epsilon} \tag{3.6}$$

where η is the Newtonian viscosity.

Several linear rheological models exist which couple the elastic response (represented by a spring) and the viscous response (represented by a dashpot). Some models are visualized in figure 3.1 and discussed below: (a) Kelvin model: the dashpot and spring are linked in a parallel circuit. The rheological equation is obtained by the superposition of the stresses of the elastic and viscous elements:

$$\sigma = 2\mu_k\epsilon + 2\eta_k\dot{\epsilon} \tag{3.7}$$

Using the method of 'variation of a constant' and assuming that the stress in the system equals to $\sigma = \sigma_0$ and the initial conditions of $\epsilon = 0$ and $t = 0$ the strain is [*Ranalli*, 1995]:

$$\epsilon(t) = \frac{\sigma_0}{2\mu}(1 - e^{-t/\tau_k}) \tag{3.8}$$

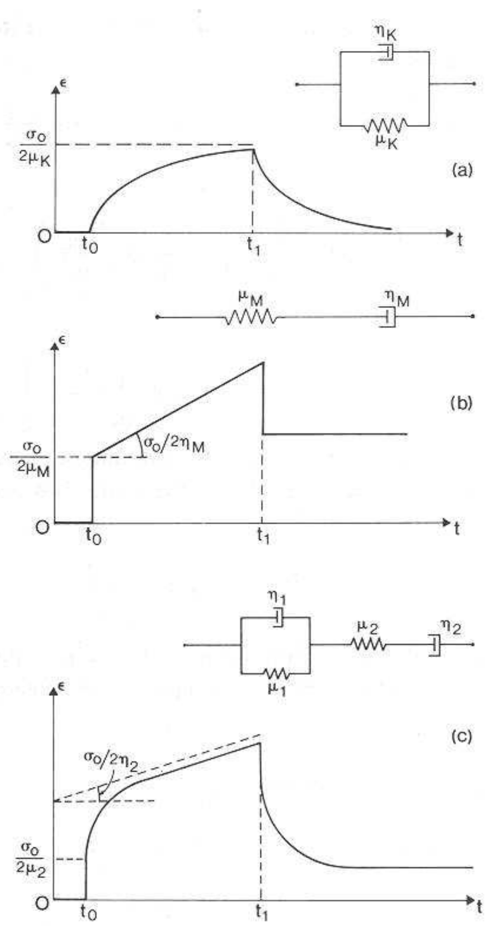

Figure 3.1 Rheological models and strain-time diagrams for (a) Kelvin, (b) Maxwell and (c) Burger bodies. On t_0 the load is introduced and on t_1 the load is removed. Source: [*Ranalli*, 1995].

where $\tau_k = \eta/\mu$ is the Kelvin retardation time.

When the system is loaded, the response of the spring is delayed by the viscous dashpot and after removal of the load the body reaches its initial position after infinite time.

(b) Maxwell model: the dashpot and spring are linked in a series circuit. The rheological equation is obtained by the superposition of strain rates:

$$\dot{\epsilon} = \dot{\epsilon}_{spring} + \dot{\epsilon}_{dashpot} = \frac{\dot{\sigma}}{2\mu_M} + \frac{\sigma}{2\eta_M} \tag{3.9}$$

When the strain rate is kept constant ($\dot{\epsilon} = 0$) and the stress in the system equals to $\sigma = \sigma_0$ the stress will be:

$$\sigma = \sigma_0 e^{-t/\tau_M} \tag{3.10}$$

where $\tau_M = \eta/\mu$ is the Maxwell relaxation time. Equation 3.10 shows that a Maxwell model has an exponential stress relaxation with a relaxation time of τ_M. When the load is removed first the instantaneous elastic response takes place and then the irreversible viscous response. The Maxwell relaxation time indicates at what time a material shows a transition from predominantly elastic behaviour to viscous behaviour [*Vermeersen*, 2004].

(c) Burgers model: the Kelvin and Maxwell model linked in a series circuit. The sum of the total strain is used to combine the both models. Take the time derivative of the Kelvin rheological equation (equation 3.7) and use the total strain ($\epsilon = \epsilon_1 + \epsilon_2$), where ϵ_1

and ϵ_2 are related to the Kelvin and Maxwell elements, to obtain the following equation:

$$\dot{\sigma} = 2\mu_k(\dot{\epsilon} - \dot{\epsilon}_2) + 2\eta_k(\ddot{\epsilon} - \ddot{\epsilon}_2) \tag{3.11}$$

Under constant stress ($\sigma = \sigma_0$) this gives for the strain:

$$\epsilon(t) = \frac{\dot{\sigma_0}}{2\mu_2} + \frac{\sigma_0}{2\mu_1}\left[1 - e^{-\mu_1/\eta_1 \cdot t}\right] + \frac{\sigma_0}{2\mu_2}t \tag{3.12}$$

When the load is removed an instantaneous elastic recovery will take place, followed by a transient creep and ultimately a steady-state creep. The transient creep is the result of the Kelvin part of the model and the steady-state creep the result of the Maxwell part of the model.

It would make most sense to use the Burgers model, but there is no general agreement whether the transient behaviour can be neglected or not. *Peltier et al.* [1981] found no evidence that it should be included, but *Sabadini et al.* [1985] and *Karato* [1989] concluded that transient rheology is compulsory when describing the GIA process. Because of the disagreement the transient rheology is still not included in GIA studies. The simplest model to describe the observed GIA is the Maxwell model. Figure 3.2 shows characteristic timescales for several geophysical phenomena in respect to the Maxwell relaxation time. The Maxwell relaxation time separates the regimes of mantle creep for anelastic deformation and steady-state flow.

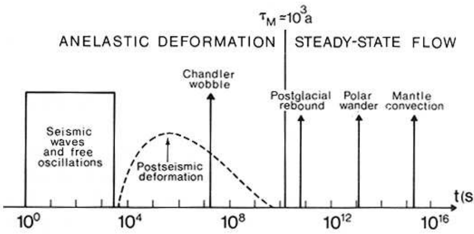

Figure 3.2 Characteristic time-scales of mantle deformation processes. Source: [*Ranalli*, 1995].

The use of linear Newtonian rheology models for describing GIA phenomenon is still a matter of debate in geophysics. There are studies referring to experimental results [*e.g.*, *Melosh*, 1980] indicating that non-linear rheology (non-Newtonian viscosity) should be used. In this case the behaviour of materials is represented by a power-law. The conclusions of *Sabadini and Vermeersen* [2004] p.2 is "that there is no unambiguous evidence in either the postglacial rebound event or in other types of geodynamic data which absolutely requires a nonlinear viscoelastic rheology".

3.2 Normal mode analysis

In this section the Maxwell viscoelastic response of the Earth will be extended to obtain the response of a multi-layer, spherically symmetric Earth. To derive this theory we will start with the following three equations: the equation of conservation of momentum, Poisson equation and the stress-strain rate relationship for a Maxwell model. These equations will give a set of coupled differential equations that can be solved using different methods. Generally there are two widely used methods. The first is the normal mode theory which obtains the viscoelastic response of a 2D or 3D, self-gravitating, linear viscoelastic spherical Earth model in an analytical way [*e.g.*, *Peltier*, 1974; *Sabadini et al.*, 1982; *Vermeersen et al.*, 1997]. *Tromp and Mitrovica* [1999] also derived a normal mode theory for an aspherical Earth model. The second is the finite-element method [*e.g.*, *Gasperini and Sabadini*, 1989; *Wu and Kaufmann*, 1998; *Forno et al.*, 2005] which obtains the viscoelastic response of a linear or non-linear viscoelastic Earth model with arbitrary 2D and 3D

viscosity structure using numerical integration techniques. Other methods are the spectral finite-difference method [*Martinec*, 1999] and a perturbation approach in Cartesian geometry [*Kaufmann and Wolf*, 2005].
A straightforward method is the finite-element method, with this method it is possible to solve the deformation, stress field and gravity field from three differential equations using numerical integration techniques and applying appropriate initial, boundary and continuity conditions. The advantages of the finite-element method over normal mode theory are that more complex models can be handled (which can include non-linear rheology and lateral variations) and regional models are easier to use. The disadvantage is that it is difficult to check the results for a global model and there is less physical insight in the mechanism of relaxation. The normal mode theory will be used in the rest of the thesis. First the three differential equations will be derived.

Assume the conservation of momentum of a free self-gravitation Earth without forcing or loading on its surface or interior. For this case the linearized equation of momentum can be derived which includes terms of stress, advection of (hydrostatic) pre-stress, self-gravitation and compressibility [*Sabadini and Vermeersen*, 2004]:

$$\nabla \cdot \boldsymbol{\sigma_1} - \nabla(\rho_0 g \boldsymbol{u} \hat{\boldsymbol{e}}_r) - \rho_0 \nabla \phi_1 - \rho_1 g \hat{\boldsymbol{e}}_r = 0 \tag{3.13}$$

where $\boldsymbol{\sigma}$ is the stress, ρ the density, g the gravity, $\boldsymbol{u}$ the displacement vector, $\hat{\boldsymbol{e}}_r$ the unit vector in radial direction and ϕ the potential field. The subscript 0 denotes the initial (reference) state and the subscript 1 denotes the (infinitesimal) perturbed state. The perturbed gravitational potential ϕ_1 for a compressible Earth satisfies Poisson's equation [*Sabadini and Vermeersen*, 2004]:

$$\nabla^2 \phi_1 = 4\pi G \rho_1 \tag{3.14}$$

in which G denotes the universal gravitational constant. In the case of incompressibility ($\rho_1 = 0$) the equation is known as Laplace's equation:

$$\nabla^2 \phi_1 = 0 \tag{3.15}$$

The stress-strain rate relationship for a 3D Maxwell model is obtained by combining equations 3.2, 3.6 and 3.9 from the previous section:

$$\dot{\sigma}_{ij} + \frac{\mu}{\eta}\Big(\sigma_{ij} - \frac{1}{3}\sum_{k=1}^{3} \sigma_{kk}\delta_{ij}\Big) = 2\mu\dot{\epsilon}_{ij} + \lambda \sum_{k=1}^{3} \dot{\epsilon}_{kk}\delta_{ij} \tag{3.16}$$

The time-dependent viscoelastic response can be determined by applying the correspondence principle deduced by *Lee* [1989] and *Biot* [1954]. The correspondence principle assumes that the Laplace transformed rheological equations of a viscoelastic body are identical with the equations for an elastic body with the same geometry. So the Laplace transformed solutions are calculated with the standard elastic analysis and inverted into the time dependent response. The Laplace transformed stress-strain rate relationship of equation 3.17 is:

$$(s + \frac{\mu}{\eta})\tilde{\sigma}_{ij}(s) - \frac{1}{3}\frac{\mu}{\eta}\sum_{k=1}^{3} \tilde{\sigma}_{kk}(s)\delta_{ij} = 2\mu s\tilde{\epsilon}_{ij}(s) + \lambda s \sum_{k=1}^{3} \tilde{\epsilon}_{kk}\delta_{ij} \tag{3.17}$$

where s is the Laplace variable and the tilde denotes the Laplace transformed variable. Equation 3.17 can also be written as the equivalent elastic or Hookean rheological equation:

$$\tilde{\sigma}_{ij}(s) = \tilde{\lambda}(s)\sum_{k=1}^{3} \tilde{\epsilon}_{kk}(s)\delta_{ij} + 2\tilde{\mu}(s)\tilde{\epsilon}_{ij}(s) \tag{3.18}$$

with the Laplace transformed *Lamé* parameters defined as:

$$\tilde{\mu}(s) = \frac{\mu s}{s + \mu/\eta}, \qquad \tilde{\lambda}(s) = \frac{\lambda s + \mu k/\eta}{s + \mu/\eta} \tag{3.19}$$

The equation of momentum, Poisson's equation and the stress-strain rate relationship for a Maxwell model form a coupled set of three second-order differential equations. Now the displacements, potential perturbation and dilatation ($\nabla \cdot \boldsymbol{u}$) are expanded in spherical harmonics. Only taking into account the spheroidal solution (no toroidal or azimuthal dependence), assuming incompressibility ($\nabla \cdot \boldsymbol{u} = 0$), surface loading and homogeneity of each layer, the 3 second order differential equations will be reduced to 6 first order differential equations, and can be written as:

$$\frac{d}{dr}\boldsymbol{y_\ell}(r,s) = \boldsymbol{A}_\ell(r,s) \cdot \boldsymbol{y_\ell}(r,s) \tag{3.20}$$

where ℓ is the spherical harmonic degree, $\boldsymbol{A_\ell}$ is the system matrix and $\boldsymbol{y_\ell}(r,s)$ is the spheroidal solution vector defined as $\boldsymbol{y_\ell} = (U_\ell, V_\ell, \sigma_{r,\ell}, \sigma_{\theta,\ell}, \phi_\ell, Q_\ell)^T$ [*Wu and Peltier*, 1982].The spheroidal solution vector contains scalar harmonic coefficients of respectively the radial and tangential displacement, radial and tangential stress, perturbation of the gravitational potential and a coefficient referred to as the potential stress.

For each homogeneous layer (with constant material parameters and gravity) the solution can be written as:

$$\boldsymbol{y_\ell}(r,s) = \boldsymbol{Y}_\ell(r,s)\boldsymbol{C}_\ell(r) \tag{3.21}$$

in which $\boldsymbol{Y}_\ell(r,s)$ is the fundamental matrix defined by *Sabadini and Vermeersen* [2004] in equation 1.74 and $\boldsymbol{C}_\ell(r)$ a 6-component vector integration constant. The solution vector can be determined from the fundamental matrix for only one layer of a spherical Earth model. When a multi-layer model is considered the top layer will be linked to the layer below by assuming continuity of the components of the solution vector. The solution vector at the surface of the Earth can now be related to the boundary conditions at the core-mantle boundary as illustrated by *Sabadini and Vermeersen* [2004] in equation 1.95. Each layer is bounded by either another viscoelastic layer, internal or an external layer and the internal boundary conditions between two viscoelastic layers are: constant parameters in each layer, during deformation there will be no cavitation or slip, and no material crosses the boundary.

For the situation where no loading occurs, the so-called constrained parameters of the solution vector $(\sigma_{r,\ell}, \sigma_{\theta,\ell}, Q_\ell)$ are zero at the surface. Then the solution of the equation that links the solution vector of the surface to the boundary condition at the core-mantle boundary are the roots of the so-called secular equation (equation 1.106 of [*Sabadini and Vermeersen*, 2004]). These solutions ($s = s_k$ with $k = 1, 2, ..K$) are the inverse relaxation times belonging to a particular relaxation mode (k) of the Earth model. These modes emerge between distinct boundaries in the Earth model due to a density discontinuity or more specifically a change in Maxwell relaxation time. Known modes are: $M0$ (surface boundary), $L0$ (between lithosphere and viscoelastic mantle boundary), Mi with i=1,2,..(buoyancy mode, between two viscoelastic layers with different density), Ti with i=1,2,.. (transient mode, between two viscoelastic layers with different Maxwell times) and $C0$ (between lowermost mantle layer and inviscid core). The solution of the secular equation can be found using a root-solving procedure, which first splits the s-domain in discrete intervals (grid-spacing) followed by a systematic search for the roots in the intervals (bisection algorithm).

In order to retrieve the complete response of the Earth also the strength of each mode has to be taken into account. The strength of the mode can be derived by applying surface loading (e.g. point mass, tidal loading) or internal loading (e.g. earthquakes, subduction). The constrained parameters of the solution vector now correspond to the boundary condition of the loading case under consideration. Using the boundary condition, the so-called unconstrained parameters of the solution vector $(U_\ell, V_\ell, \phi_\ell)$ at the surface can be determined in the Laplace domain. The inverse Laplace transform to the time domain is carried out by applying complex contour integration introduced by

[*Wu*, 1978]. In case of surface loading, the solution of the constrained parameters at the surface of the Earth are usually expressed in dimensionless load Love numbers. These Love numbers are named after A.E.H. Love, who first introduced them to describe the elastostatic case in which the "load" was associated with the variations of the gravity field responsible for the solid-Earth tides. The dimensionless Love numbers in the time domain are defined by [*Peltier*, 1974] as:

$$\frac{M_e}{a}\begin{pmatrix} U_\ell(a,t) \\ V_\ell(a,t) \\ -\phi_\ell(a,t)/g \end{pmatrix} = \begin{pmatrix} h_\ell(t) \\ \ell_\ell(t) \\ 1+k_\ell(t) \end{pmatrix} = \begin{pmatrix} h_\ell^E \\ \ell_\ell^E \\ 1+k_\ell^E \end{pmatrix} \delta(t) + \sum_{k=1}^{K} \begin{pmatrix} r_k^\ell \\ r''^{\ell}_k \\ r'^{\ell}_k \end{pmatrix} e^{-s_k^\ell t} \tag{3.22}$$

where a is the mean radius of the Earth, M_e the mass of the Earth, g the average surface gravitational acceleration, $h_\ell(t)$ and $\ell_\ell(t)$ are the Love numbers of respectively radial and horizontal displacement. The final Love number is $1+k_\ell(t)$ which is the geopotential perturbation due to Earth deformation (k_ℓ) and direct effect of the load. The first term on the right-hand side of equation 3.22 represents the immediate elastic response part and the second term describes the viscoelastic response part (note that the viscouselastic response has a non-zero contribution at the instant the load is applied). The immediate elastic response part is described by the elastic love numbers ($h_\ell^E, \ell_\ell^E, k_\ell^E$) which are multiplied by the Dirac delta response function δ. The viscoelastic response is characterized by a set of K individual modes of exponential decay. Each mode is defined by an inverse decay time (s_k^ℓ) and amplitude ($r_k^\ell, r''^{\ell}_k, r'^{\ell}_k$), that both depend on the viscoelastic profile of the used Earth model.

Chapter 4

Postglacial sea level on a non-rotating Earth

The corner stone of the modern theory of glacial isostatic adjustment (GIA) is the sea level equation. With the use of relative sea level data from regions once covered with ice it is possible to reconstruct the ice-load history since the last glacial maximum (LGM)). The relationship between sea level and ice melting and growing seems straightforward but is more complex due to effects like mantle flow or true polar wander (TPW). The basic sea level equation by *Farrell and Clark* [1976] will be treated in section 4.1. In section 4.2 the load induced sea level equation will be presented in which the dimensionless Love numbers derived in the previous chapter 3 will be used. The techniques for solving the sea level will be treated in section 4.3.

4.1 GIA and the sea level equation

The interaction between GIA and sea level is complex, because of the coupling between the sea level, (continental) ice, mantle flow, true polar wander and climate as described in section 2.2. In GIA studies the effect of climate is left out of the equation and we will discuss the TPW in chapter 5. *Farrell and Clark* [1976] derived the primitive form the sea level equation which provided a theoretical framework for predicting gravitationally self-consistent, post-glacial sea level changes, and is the standard reference for modern analysis of the GIA process:

$$S = \rho_I \frac{\phi}{g} * L + \rho_w \frac{\phi}{g} * S + C \tag{4.1}$$

where S is the change in sea level, L the change in continental ice mass, ϕ the Green's function for variation in the gravitational potential, g the surface gravity, ρ_I the density of ice and ρ_w the density of water. The asterisk represents time convolution and the constant C is present to assure that the sea level change conserves mass. Sea level change itself is the result of the change in load induced by the ice mass and sea level, which can be solved in an iterative manner.

4.2 Sea level equation on a non-rotating Earth

The load-induced sea level equation will be determined for a non-rotating, self-gravitating, Maxwell viscoelastic Earth model [*Farrell and Clark*, 1976]. Time-dependent continent margins and near-field water dumping, described by [*Milne et al.*, 1999], will not be treated in this study. The formalism is generally based upon [*Milne and Mitrovica*, 1998] and [*Mitrovica and Peltier*, 1991]. From now on the superscripts L and T are used to distinguish between parameters associated with the surface mass loading (discussed in this chapter) and the rotational potential (discussed in chapter 5), respectively. The sea level can be described by the difference between the geoid G (which is the equipotential surface corresponding to the sea level) and the topography/bathymetry. So the change in sea level can be defined as the relative change between the spatial and time-dependent load-induced geoid anomaly $G(\theta,\psi,t)$ and the load-induced radial displacement of the topography/bathymetry $R(\theta,\psi,t)$ multiplied by the ocean function [*Munk and MacDonald*, 1960]:

$$S = C(\theta,\psi)(G^L(\theta,\psi,t) - R^L(\theta,\psi,t)) \tag{4.2}$$

where θ represents the co-latitude, ψ the east-longitude, t the time and $C(\theta,\psi) = 1$ in case of oceans and $C(\theta,\psi) = 0$ in case of land. At this point the ocean-function is assumed to be time-independent. In order to calculate the perturbations in both the geoid and solid surface the impulse response of a Maxwell viscoelastic Earth model to a load will be described by dimensionless surface load Love numbers. These Love numbers (defined in chapter 3) are used to construct impulse response Green's functions for the gravitational potential perturbation of the undeformed surface $\Phi^L(\gamma,t)$ and the radial displacement of the solid surface $\Gamma^L(\gamma,t)$. $\Phi^L(\gamma,t)$ can also be described as the potential perturbation due to mass redistribution in the planetary interior. The Legendre polynomial expansion of Green's functions are [*Mitrovica and Peltier*, 1991]:

$$\Phi^L(\gamma,t) = \frac{ag}{M_e}\sum_{\ell=0}^{\infty}\left\{\delta(t) + k_\ell^{L,E}\delta(t) + \sum_{k=1}^{K} r'^{\ell,L}_k e^{-s_k^\ell t}\right\}P_\ell(cos\gamma) \tag{4.3}$$

$$\Gamma^L(\gamma,t) = \frac{a}{M_e}\sum_{\ell=0}^{\infty}\left\{h_\ell^{L,E}\delta(t) + \sum_{k=1}^{K} r^{\ell,L}_k e^{-s_k^\ell t}\right\}P_\ell(cos\gamma) \tag{4.4}$$

where γ represents the angular distance between the impulse load point and the observation point. The first Dirac delta function on the right-hand side of equation 4.3 resembles the direct effect of the impulse surface load on the Earth's gravitational potential. The P_ℓ are Legendre functions which are part of the spherical harmonics explained later. Now the surface load, $L(\theta,\psi,t)$, to which the viscoelastic Earth is exposed, is introduced. This function represents a model of the spatio-temporal variation in the ice-ocean mass exchange. The surface load can be separated into contributions from the (land)ice sheets and from the associated sea level variations as shown below:

$$L(\theta,\psi,t) = \rho_i I(\theta,\psi,t) + \rho_w S(\theta,\psi,t) \tag{4.5}$$

where ρ_i is the average density of ice, ρ_w the average density of water and $I(\theta,\psi,t)$ and $S(\theta,\psi,t)$ are functions which describe chronological and spatial changes in ice and ocean height. The solid surface radial displacement is calculated by convolving Green's function (equation 4.4) and the surface load in both time and space. This gives for the solid surface radial displacement:

$$R^L(\theta,\psi,t) = \int_{-\infty}^{t}\iint_{\Omega} a^2 L(\theta',\psi',t')\Gamma^L(\gamma',t-t')d\Omega' dt' \tag{4.6}$$

where Ω represents the entire surface of the Earth, $L(\theta',\psi',t')$ is the surface load specified in equation 4.5 and $\Gamma^L(\gamma',t-t')$ is the Green's function of the radial displacement defined in equation 4.4 [*Peltier*, 1974]. The geoid anomaly is constructed in the same way as the solid surface radial displacement:

$$\begin{aligned} G^L(\theta,\psi,t) &= \frac{\Phi(\theta,\psi,t) + \Delta\Phi(t)}{g} \\ &= \frac{1}{g}\int_{-\infty}^{t}\iint_{\Omega} a^2 L(\theta',\psi',t')\Phi^L(\gamma',t-t')d\Omega' dt' + \frac{\Delta\Phi^L(t)}{g} \end{aligned} \tag{4.7}$$

where Φ^L is the Green's function of the potential perturbation defined in equation 4.3

[*Peltier*, 1976b] and $[\Delta\Phi^L(t)]/g$ is a global uniform shift of the geoid which changes in time and is determined by surface load mass conservation. The surface load mass conservation is based upon the assumption that the total volume between the three dimensional geoidal and solid Earth surface over the oceans is equal to the volume of water exchanged between the ice sheets and oceans. This gives:

$$\frac{\Delta\Phi(t)}{g} = -\frac{M_I(t)}{\rho_w A_0} - \frac{1}{A_0}\left(\int_{-\infty}^{t} \iint_{\Omega_o} L(\theta',\psi',t') \Big\{ \frac{\Phi(\gamma,t-t')}{g} - \Gamma(\gamma,t-t') \Big\} d\Omega' dt' \right) \tag{4.8}$$

where M_I is the total melted ice mass, Ω_o represents the surface of the oceans and A_0 is the area of all the oceans, that is assumed to be constant. The first term on the right-hand side of equation 4.8 represents the eustatic sea level change which is the sea level change when assumed that the distribution of water is spatially independent. The second term on the right-hand side is an integrated measure of the distance between the geoid and the Earth's solid surface and is responsible for ocean syphoning (see section 2.2.1) over the oceans. Constructing the sea level defined in equation 4.2 from the difference between the geoid anomaly (equation 4.6) and surface radial displacement (equation 4.7) gives:

$$\begin{aligned} S(\theta,\psi) &= C(\theta,\psi,t)[G^L(\theta,\psi,t) - R^L(\theta,\psi,t)] \\ &= C(\theta,\psi)\Bigg[\int_{-\infty}^{t} \iint_{\Omega} a^2 L(\theta',\psi',t') \Big\{ \frac{\Phi^L(\gamma,t-t')}{g} \\ &\qquad - \quad \Gamma^L(\gamma,t-t') \Big\} d\Omega' dt' + \frac{\Delta\Phi^L(t)}{g} \Bigg] \end{aligned} \tag{4.9}$$

This is the sea level equation for a non-rotating Earth model. To solve the temporal convolution in the sea level equation a discretization in time is needed. The surface load from equation 4.5 is therefore modeled as a series of Heaviside loading increments (e.g. [*Farrell and Clark*, 1976]. This gives:

$$L(\theta,\psi,t) = \sum_{n=1}^{N} [\rho_i \delta I^n(\theta,\psi) + \rho_w \delta S^n(\theta,\psi)] H(t-t_n) \tag{4.10}$$

where $H(t)$ is the Heaviside step function. This special form of equation 4.10 allows for an analytical solution for the time convolution in equation 4.9. Combining equation 4.3, 4.4, 4.5 and 4.9 gives:

$$\begin{aligned} S(\theta,\psi,t) = C(\theta,\psi)\Bigg[& \iint_{\Omega} a^2(\rho_i I(\theta',\psi',t) + \rho_w S(\theta',\psi',t)) Z^{L,E}(\gamma) d\Omega' \\ + & \sum_{n=1}^{N} H(t-t_n) \iint_{\Omega} a^2[\rho_i \delta I^n(\theta',\psi') + \rho_w \delta S^n(\theta',\psi')] \\ \times & \; Z^{L,NE}(\gamma,t-t_n) d\Omega' + \frac{\Delta\Phi^L(t)}{g} \Bigg] \end{aligned} \tag{4.11}$$

in which:

$$Z^{L,E}(\gamma) = \frac{a}{M_e} \sum_{\ell=0}^{\infty} E_\ell^L P_\ell(cos\gamma) \tag{4.12}$$

$$Z^{L,NE}(\gamma,t-t_n) = \frac{a}{M_e} \sum_{\ell=0}^{\infty} \beta_\ell^L(t-t_n) P_\ell(cos\gamma) \tag{4.13}$$

where E_ℓ^L includes all the contributions of the elastic love numbers:

$$E_\ell^L = 1 + k_\ell^{L,E} - h_\ell^{L,E} \tag{4.14}$$

and β_ℓ^L contains all the information on the viscous behaviour of a specific Earth model:

$$\beta_\ell^L(t-t_n) = \sum_{k=1}^{K} \frac{({r'}_k^{\ell,L} - r_k^{\ell,L})}{s_k^\ell}\,[1-e^{-s_k^\ell(t-t_n)}] \tag{4.15}$$

where the first and second term on the right-hand side refer to respectively the elastic (superscript E) and non-elastic (superscript NE) response to a surface load.

4.3 Solving the sea level equation for a non-rotating Earth

Previously the load was modeled as a series of Heaviside loading increments to solve for the temporal convolution in the sea level equation. This has the result that the sea level equation, formulated in equation 4.11, can be solved by defining also the sea level equation as a series of Heaviside increments in time. So $\delta S(\theta,\psi,t_n)$ has to be determined for successive values of n. When the j^{th} Heaviside increment is considered, the increment is defined as the difference in sea level between two successive time steps t_j and t_{j-1}:

$$\delta S(\theta,\psi,t_j) = S(\theta,\psi,t_j) - S(\theta,\psi,t_{j-1}) \tag{4.16}$$

which gives for the sea level at the j^{th} increment:

$$S(\theta,\psi,t_j) = S(\theta,\psi,t_{j-1}) + \delta S(\theta,\psi,t_j) \tag{4.17}$$

where $S(\theta,\psi,t_j)$ is the sea level to be determined, $S(\theta,\psi,t_{j-1})$ is known from the previous calculation and $\delta S(\theta,\psi,t_j)$ is determined iteratively. The first guess of the iteration is given by the eustatic sea level change (e.g. [*Mitrovica and Peltier*, 1991]):

$$[\delta S^n(\theta,\psi)]^{i=1} = -\rho_i\Big\{\iint_\Omega \delta I^n(\theta,\psi)d\Omega\Big\}\frac{C(\theta,\psi)}{\rho_w A_0} \tag{4.18}$$

There are three approaches for solving the sea level equation and especially solving the surface convolution integral. The convolution can be solved in the spatial or spectral domain. Here the pseudo-spectral approach will be used to calculate the solution of the sea level equation, which performs the calculation both in the spectral and spatial domain. To give an overview also the spatial and spectral approach will also be discussed briefly in the next paragraphs.

4.3.1 Spatial approach

The gravitationally self-consistent spatial solutions of the sea level equation are based upon the "discretized formulation" defined by [*Peltier*, 1976b], [*Peltier et al.*, 1978] and [*Wu and Peltier*, 1983] and uses both Green function and finite disc techniques. This technique discretizes ocean surfaces using circular discs of varying radius where the resolution is increased at continental shorelines. The convolution over the Earth's surface is performed in the space domain using a large set of interaction coefficients. It is very straightforward to use the spatial approach, but it is not the preferred solution because the resolution on a global scale is scattered, and it requires relatively a lot of computing power.

4.3.2 Spectral approach

In case of the spectral approach the convolution over the Earth's surface is performed in the spectral domain [*e.g.*, *Mitrovica and Peltier*, 1991]. The spectral approach gives an uniform distribution of global resolution that depends upon the truncation level of the spherical harmonic expansion. The sea level equation is rewritten into a series expansion in spherical harmonics as shown below.

Assume a field $\mathscr{X}(\theta,\psi)$ defined on a surface of a sphere which can be spectrally decomposed into terms of spherical harmonic expansion:

$$\mathscr{X}(\theta,\psi) = \sum_{\ell,m} \mathscr{X}_{\ell,m} Y_{\ell,m}(\theta,\psi) \tag{4.19}$$

where

$$\sum_{\ell,m} = \sum_{\ell=0}^{\infty} \sum_{m=-\ell}^{\ell} \tag{4.20}$$

and $Y_{\ell,m}$ are the normalized surface spherical harmonics that satisfy the following normalization for the basis functions:

$$\iint_{\Omega} Y^{\dagger}_{\ell',m'}(\theta,\psi) Y_{\ell,m}(\theta,\psi) sin\theta \, d\theta d\psi = 4\pi \delta_{\ell',\ell} \delta_{m',m} \tag{4.21}$$

where † is the complex conjugate. This normalization is much used by Mitrovica and Peltier. Extra care should be taken when the sea level theory is incorporated in existing theory, because different types of normalization are commonly used. Much used normalizations are the fully normalization applied by [*e.g.*, *Sneeuw*, 1994; *Heiskanen and Moritz*, 1967] and also used on the Department of Earth Observation and Space systems:

$$\iint_{\Omega} Y^{\dagger}_{\ell',m'}(\theta,\psi) Y_{\ell,m}(\theta,\psi) sin\theta \, d\theta d\psi = \frac{4\pi}{2-\delta_{m0}} \delta_{\ell',\ell} \delta_{m',m} \tag{4.22}$$

or the 1-normalization used by *Martinec and Hagedoorn* [2005]:

$$\iint_{\Omega} Y^{\dagger}_{\ell',m'}(\theta,\psi) Y_{\ell,m}(\theta,\psi) sin\theta \, d\theta d\psi = \delta_{\ell',\ell} \delta_{m',m} \tag{4.23}$$

This results in:

$$\begin{aligned} [Y_\ell^m(\theta,\psi)]_{fully-normalized} &= \sqrt{2-\delta_{m0}} [Y_\ell^m(\theta,\psi)]_{Mitrovica-normalized} \\ &= \sqrt{\frac{2-\delta_{m0}}{4\pi}} [Y_\ell^m(\theta,\psi)]_{1-normalized} \end{aligned} \tag{4.24}$$

The spatial convolution in 4.11 can now be done analytically by using the spectral decomposition and normalization [*e.g.*, *Mitrovica and Peltier*, 1991; *Mitrovica and Milne*, 1998]:

$$\iint_{\Omega} \mathscr{X}(\theta,\psi) P_\ell(cos\gamma) \, d\Omega' = \frac{4\pi}{(2\ell+1)} \sum_{m=-\ell}^{\ell} \mathscr{X}_{\ell,m} Y_{\ell,m}(\theta,\psi) \tag{4.25}$$

This gives the following sea level equation in the spectral domain for a Maxwell viscoelastic, non-rotating Earth model excited by a Heaviside loading history [*Mitrovica and Peltier*, 1991; *Mitrovica and Milne*, 1998]:

$$\begin{aligned} &\sum_{\ell,m} S_{\ell,m}(t) Y_{\ell,m}(\theta,\psi) = \\ &\qquad C(\theta,\psi) \sum_{\ell,m} \Bigg\{ E_\ell^L T_\ell (\rho_i I_{\ell,m}(t) + \rho_w S_{\ell,m}(t)) + T_\ell \sum_{n=1}^{N} (\rho_i \delta I^n_{\ell,m} \\ &\qquad + \quad \rho_w \delta S^n_{\ell,m}) \beta_\ell^L (t-t_n) H(t-t_n) + \frac{\Delta\Phi^L(t)}{g} \delta_{\ell,0} \delta_{m,0} \Bigg\} Y_{\ell,m}(\theta,\psi) \end{aligned} \tag{4.26}$$

where T_ℓ holds all the dimensional parameters:

$$T_\ell = \frac{4\pi a^3}{M_e(2\ell+1)} \tag{4.27}$$

and $I_{\ell m}$, $S_{\ell m}$, $\delta I_{\ell m}$ and $\delta S_{\ell m}$ are respectively the spherical harmonic coefficients of the total and Heaviside increments of the ice and sea load functions. A purely spectral method is derived by *Dahlen* [1976] for determining the equilibrium ocean tide of an elastic planet. This theory is extended to the to the viscoelastic case by *Mitrovica and Peltier* [1991]. Due to complicated spatial convolutions and gridding schemes, as result of the multiplication of the ocean function with the sea level equation in the spherical harmonic domain, a truncation level of about degree 30 (which equals to a maximum resolution of 667 km at the equator) can be reached with this approach. A truncation level of 30 is not sufficient enough to accurately determine the sea level, especially near irregular ice-sheets and continental margins, so the pseudo-spectral approach was developed.

4.3.3 Pseudo-spectral approach

Rewrite equation 4.26 to the form of equation 4.16 and we obtain the increment in sea level between time t_j and t_{j-1}:

$$\begin{aligned}
&\sum_{\ell,m} \delta S^j_{\ell,m} Y_{\ell,m}(\theta,\psi) = \\
&\qquad -\sum_{\ell,m} S_{\ell,m}(t_{j-1}) Y_{\ell,m}(\theta,\psi) + C(\theta,\psi)\sum_{\ell,m}\Bigg\{ E^L_\ell T_\ell \Big(\rho_i I_{\ell,m}(t_j) \\
&\qquad +\rho_w S_{\ell,m}(t_{j-1}) + \rho_w \delta S^j_{\ell,m}\Big) + T_\ell \sum_{n=1}^{N} (\rho_i \delta I^n_{\ell,m} + \rho_w \delta S^n_{\ell,m}) \beta^L_\ell (t_j - t_n) \\
&\qquad \times H(t-t_n) + \frac{\Delta\Phi^L(t_j)}{g}\delta_{\ell,0}\delta_{m,0}\Bigg\} Y_{\ell,m}(\theta,\psi)
\end{aligned} \tag{4.28}$$

To calculate the sea level, the sea level increment, defined in equation 4.28, will be used for an iterative algorithm. Introduce the (iteration) index i and assume that $[\delta S^j_{lm}]^i$ is the approximation and $[\delta S^j_{lm}]^{i+1}$ is the improved estimate of δS^j_{lm}. Also a shorter notation is introduced:

$$\begin{aligned}
\sum_{\ell,m} [\delta S^j_{\ell,m}]^{i+1} Y_{\ell,m}(\theta,\psi) &= -\sum_{\ell,m} S_{\ell,m}(t_{j-1}) Y_{\ell,m}(\theta,\psi) \\
&\quad + C(\theta,\psi)\Big[\sum_{p,q} [R_{p,q}(t_j)]^i Y_{p,q}(\theta,\psi) + \big[\frac{\Delta\Phi^L(t_j)}{g}\delta_{p,0}\delta_{q,0}\big]^i\Big]
\end{aligned} \tag{4.29}$$

where

$$\begin{aligned}
[R_{p,q}(t_j)]^i &= E^L_p T_p \big(\rho_i I_{p,q}(t_j) + \rho_w S_{p,q}(t_{j-1}) + \rho_w [\delta S^j_{p,q}]^i\big) \\
&\quad + T_p \sum_{n=1}^{N} \beta^L_p (t_j - t_n)(\rho_i \delta I^n_{p,q} + \rho_w \delta S^n_{p,q})
\end{aligned} \tag{4.30}$$

$R_{p,q}$ in spherical coordinates will have the following representation:

$$R^i(\theta,\psi,t_j) = \sum_{p,q} [R_{p,q}(t_j)]^i Y_{p,q}(\theta,\psi) \tag{4.31}$$

Now RO is introduced as the projection of R onto the ocean function in the spatial domain. The transformation from the spectral to the spatial domain is done using the Fast Fourier Transform in the the longitudinal direction on a fixed latitude. Then the solution is integrated in the latitudinal direction using the Gaussian quadrature [*Sneeuw*, 1994]. In the final step R is transformed back again to the spectral domain by summation over degree (for fixed order) followed by an inverse Fourier Transform:

$$\begin{aligned} RO^i(\theta,\psi,t_j) &= C(\theta,\psi)\,\sum_{p,q}[R_{p,q}(t_j)]^i Y_{p,q}(\theta,\psi) \\ &= C(\theta,\psi)\;R^i(\theta,\psi,t_j) \\ &= \sum_{\ell,m}[RO_{\ell,m}(t_j)]^i\;Y_{\ell,m}(\theta,\psi) \end{aligned} \tag{4.32}$$

Now use 4.32 to rewrite equation 4.29 to the spectral domain:

$$[\delta S^j_{\ell,m}]^{i+1} = -S_{\ell,m}(t_{j-1}) + [RO_{\ell,m}(t_j)]^i + \left[\frac{\Delta\Phi(t_j)}{g}\right]^i C_{\ell,m} \tag{4.33}$$

where the ocean function in spherical coordinates is:

$$\sum_{\ell,m} C_{\ell,m}Y_{\ell,m} = C(\theta,\psi) \tag{4.34}$$

and the global uniform shift of the geoid of equation 4.8 is:

$$\left[\frac{\Delta\Phi(t_j)}{g}\right]^i = \Big(-\frac{\rho_i}{\rho_w}I_{0,0}(t_j) - [RO_{0,0}(t_j)]^i\Big)(C_{0,0})^{-1} \tag{4.35}$$

Equation 4.33 provides the iterative pseudo-spectral solution to the sea level equation. This technique is summarized in figure 4.1. To start the iterative process a first guess of the solution has to be provided, which in this case is based upon the eustatic sea level change. Equation 4.18 in spherical coordinates is written as:

$$[\delta S^j_{\ell,m}]^{i-1} = -\left\{\frac{\rho_i}{\rho_w}\frac{4\pi a^2}{A_0}\delta I^j_{0,0}\right\}C_{\ell,m} \tag{4.36}$$

A level of convergence is defined to determine the relative difference in solution of two successive iterations:

$$\zeta^{i+1} = \sum_{\ell,m}\frac{|[\delta S^j_{\ell,m}]^{i+1}| - |[\delta S^j_{\ell,m}]^i|}{|[\delta S^j_{\ell,m}]^i|} \tag{4.37}$$

If $\zeta < 10^{-2}$ is assumed no more then two or three iterations are needed. This technique, introduced by *Mitrovica and Peltier* [1991], is called pseudo-spectral because all the computations are performed in the spectral domain except the projection of $R^i(\theta,\psi,t)$ on the ocean function. This technique avoids the use of complicated spatial convolutions and gridding schemes as used in the purely spectral method, which is the result of the multiplication of the ocean function with the sea level equation in the spherical harmonic domain. This allows for much higher truncation levels then 30 and nowadays maximum truncation levels are reached well above 256.

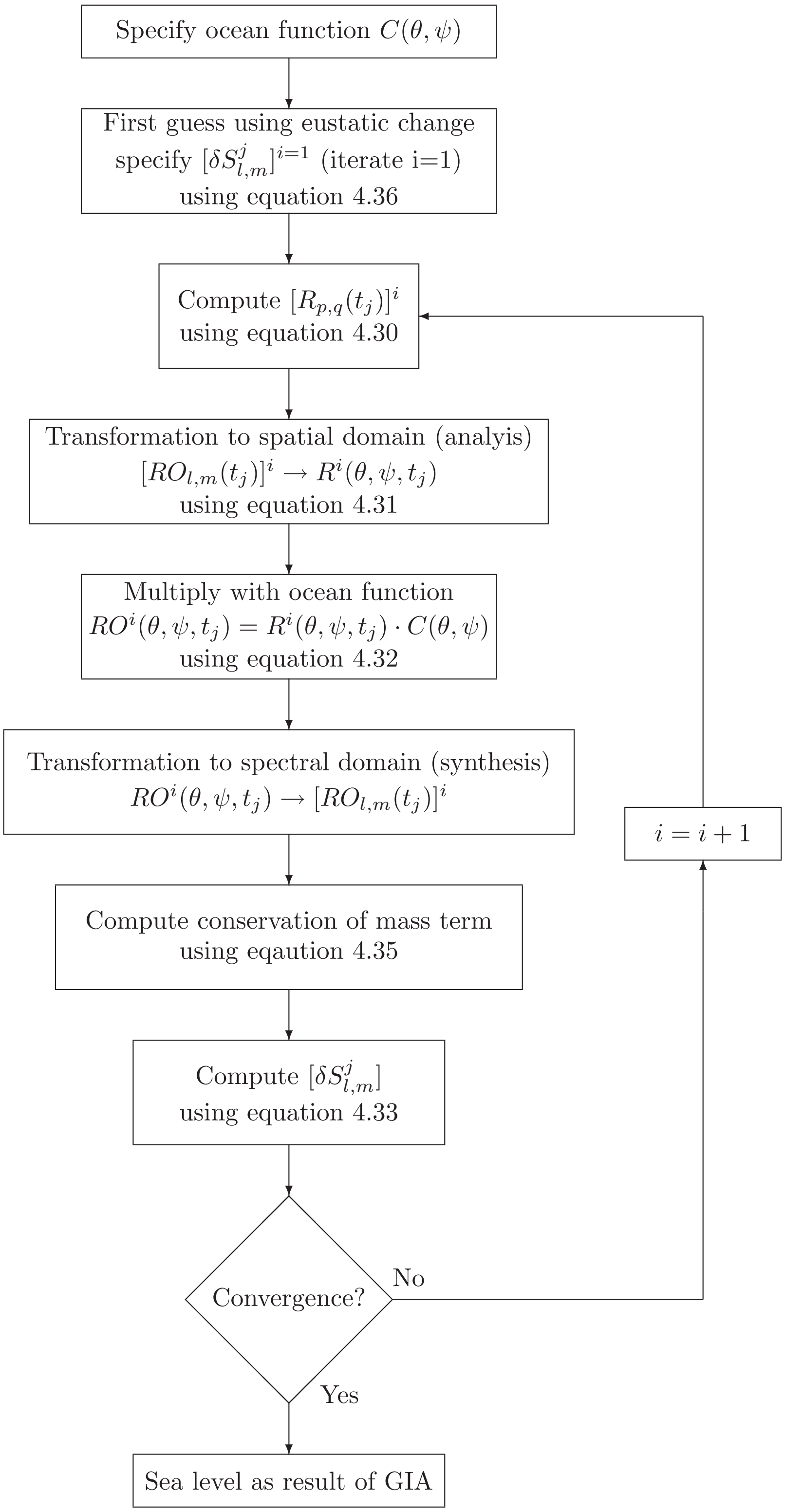

Figure 4.1 Pseudo-spectral solution to the sea level equation. Redrawn from: [*Mitrovica and Peltier*, 1991].

Chapter 5

Postglacial sea level on a rotating Earth

Although the effect of Earth rotation on sea level change is small, the perturbations due to changes in the orientation of the rotation vector can in some parts of the world be as large as the signal using a non-rotating Earth model [*Mitrovica et al.*, 2001]. *Nakada* [2000, 2002] introduced a paradox, namely that the predictions of present-day TPW speed for the case of a viscoelastic lithosphere did not converge to the predictions on an elastic lithosphere. This paradox was solved by *Mitrovica et al.* [2005], who introduced a revised rotation theory. In section 5.1 the classical Earth rotation theory and revised rotation theory will be discussed, followed in section 5.2 by the implementation of the rotation theory in the sea level equation derived in chapter 4. The techniques for solving the sea level equation for a rotating Earth can be found in section 5.3.

5.1 Earth rotation theory

The rotation of the Earth is variable and changes in both position of the rotation axis and the rotation rate. It is assumed that the rotational changes have a large impact as there are indications that the emergence of the great ice cycles 2 million years ago were triggered by a gradual shift of the rotation axis over the Earth's surface, combined with wandering of the continents and associated changes in the ocean currents [*Sabadini and Vermeersen*, 2004].
The fundamental equations governing the rotation of a body are Euler's dynamical equations. These equations describe the rotational response of a body (expressed in angular momentum $\boldsymbol{H}$) to an applied torque $\boldsymbol{L}$ with respect to an inertial reference frame:

$$\frac{\boldsymbol{dH}}{\boldsymbol{dt}} = \boldsymbol{L} \tag{5.1}$$

It is more convenient to express forces, velocities and torques with respect to a reference frame which is fixed to the rotating body:

$$\frac{d\boldsymbol{H}}{dt} + \boldsymbol{\omega} \times \boldsymbol{H} = \boldsymbol{L} \tag{5.2}$$

in which the angular velocity of the axis is denoted as $\boldsymbol{\omega}$. The angular momentum for a rigid body is defined as:

$$\boldsymbol{H} = \int \rho \boldsymbol{r} \times (\boldsymbol{\omega} \times \boldsymbol{r}) dV = \int \rho (r^2 \boldsymbol{\omega} - (\boldsymbol{r} \cdot \boldsymbol{\omega}) \boldsymbol{r}) dV = \boldsymbol{I} \cdot \boldsymbol{\omega} \tag{5.3}$$

where the inertia tensor $\boldsymbol{I}$ has the following elements:

$$I_{ij} = \int \rho (r_k k \delta_{ij} - r_{ij}) dV \tag{5.4}$$

where ρ and $\boldsymbol{r}$ are respectively the density and the coordinates of the mass element under consideration and δ_{ij} is the Kronecker delta function. Equation 5.3 into equation 5.2 gives:

$$\frac{d}{dt}(\boldsymbol{I}\cdot\boldsymbol{\omega})+\boldsymbol{\omega}\times(\boldsymbol{I}\cdot\boldsymbol{\omega})=\boldsymbol{L} \tag{5.5}$$

The Earth's actual motion differs from the rigid motion in two aspects: the inertia tensor is time dependent because of mass displacements and the motion occurs relative to the body fixed axis $\boldsymbol{r}$. Hence the angular momentum must be written as:

$$\boldsymbol{H}(t)=\boldsymbol{I}(t)\cdot\boldsymbol{\omega}+\boldsymbol{h}(t) \tag{5.6}$$

where the angular momentum vector due to motion is:

$$\boldsymbol{h}(t)=\int\rho\boldsymbol{r}\times\boldsymbol{u}dV \tag{5.7}$$

Substituting equation 5.6 into equation 5.5 gives the Liouville equation [*Munk and MacDonald*, 1960]:

$$\frac{d}{dt}(\boldsymbol{I}(t)\cdot\boldsymbol{\omega}+\boldsymbol{h}(t))+\boldsymbol{\omega}\times(\boldsymbol{I}(t)\cdot\boldsymbol{\omega}+\boldsymbol{h}(t))=\boldsymbol{L} \tag{5.8}$$

Assume a right-handed body fixed Cartesian coordinate system with the origin of this system equal the the center of mass of the Earth model in unperturbed state. The system is oriented in such a way that the x_1 axis is aligned with the Greenwich longitude and the x_2 axis is $90\,^\circ E$ of x_1 (see figure 5.1). Prior to surface loading the rotation vector $\boldsymbol{\omega}$ can

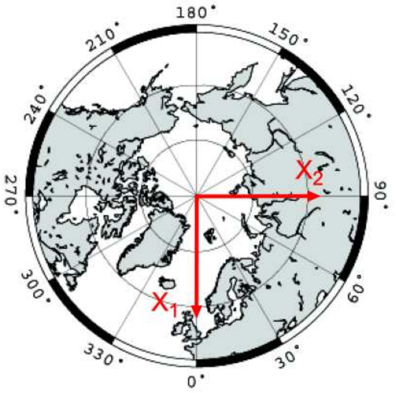

Figure 5.1 Right-handed body fixed Cartesian coordinate system. X$_1$ axis is aligned with the Greenwich longitude and the X$_2$ axis is $90\,^\circ E$ of X$_1$.

be written in the body-fixed reference frame as:

$$\boldsymbol{\omega}_0=(0,0,\Omega) \tag{5.9}$$

where Ω is the mean Earth rotation frequency. To solve the Liouville equation linearization is applied by assuming small deviations from the axis of rotation vector from equation 5.9:

$$\boldsymbol{\omega}_1=(\omega_1,\omega_2,\omega_3)=\Omega(m_1,m_2,1+m_3) \tag{5.10}$$

where m_i are dimensionless quantities that represent the direction cosines of $\boldsymbol{\omega}$ relative to the principal axis. m_1 and m_2 are the components of polar motion or wobble in respectively x_1 and x_2 direction defined above. m_3 gives the change in length of day in radians per sidereal day and $\Omega dm_3/dt$ is also known as the acceleration in diurnal motion[1]. In case of small deviations in the rotation vector the assumption can be made that the changes in $\boldsymbol{h}$ and $\boldsymbol{I}$ are small. This assumption makes it possible to write equation 5.8 as [*Sabadini and Vermeersen*, 2004]:

$$\frac{\dot{m}_1}{\sigma_r} + m_2 = \phi_2 \tag{5.11}$$

$$\frac{\dot{m}_2}{\sigma_r} + m_1 = -\phi_1 \tag{5.12}$$

$$\dot{m}_3 = \dot{\phi}_3 \tag{5.13}$$

in which ϕ_1, ϕ_2 and ϕ_3 are dimensionless excitation functions given in [*Sabadini and Vermeersen*, 2004] and σ_r is the Eulerian free precession frequency of a rigid body defined as:

$$\sigma_r = \frac{C-A}{A}\Omega \tag{5.14}$$

where A is the moment of inertia for an equatorial principal axis and C is moment of inertia for a polar principal axis. The Eulerian free precession frequency of the Earth is about 1/306 revolutions per day and a period of 10 months. The linearized Liouville equation for polar wander can be written in complex notation to achieve a more compact form using equations 5.11, 5.12 and 5.13 and assuming $\boldsymbol{m} = m_1 + im_2$:

$$i\frac{\dot{\boldsymbol{m}}}{\sigma_r} + \boldsymbol{m} = \Phi = \Phi_L + \Phi_R \tag{5.15}$$

and

$$m_3 = -\phi_3 = \frac{\Delta I_{33}}{C} \tag{5.16}$$

where the excitation function Φ can be split into to two parts: direct geodynamic forcing (Φ_L) and induced rotational deformation (Φ_R), ΔI_{33} represents the small perturbations of inertia of the polar principal axis due to both direct geodynamic forcing and induced rotational deformation.

Direct geodynamic forcing

If only mass displacements are considered and the influence of relative motions, time variations of the inertia and external torques are neglected, then the direct geodynamic forcing function of a rigid Earth (in complex notation) is defined as [*Sabadini and Vermeersen*, 2004]:

$$\Phi_L = \phi_1 + i\phi_2 = \frac{\Delta I^L_{13}}{C-A} + i\frac{\Delta I^L_{23}}{C-A} \tag{5.17}$$

where ΔI^L_{i3} (i=1,2,3) are matrix elements of the inertia tensor $\boldsymbol{I}$ representing the small perturbations of inertia of the polar principal axis due to the change in mass along equatorial principal axis. The perturbation of inertia can be divided into separate contributions. First there is the direct effect of the surface mass loads due to the redistribution of ice and water on the Earth's surface. Secondly there is a contribution due to redistribution of mass in the planetary interior induced by the surface mass loads (also referred to as the isostatic adjustment of the Earth). The perturbation of inertia due isostatic adjustment of the Earth is calculated by convolving the perturbation of inertia, due to the direct effect of the surface mass loads, with the surface load Love number of degree 2 (k^L_2) [*Wu and Peltier*, 1984]. This gives the following equation:

$$\Delta I^L_{i3} = \Delta I^S_{i3} + \Delta I^D_{i3} = \Delta I^S_{i3} * (1 + k^L_2) \qquad (i = 1,2,3) \tag{5.18}$$

---

[1] Diurnal motion is the apparent daily motion of stars in orbit around the Earth as a result of the Earth's rotation

where ΔI^S_{i3} (i=1,2,3) denotes the perturbation of inertia due to surface loading and ΔI^D_{i3} (i=1,2,3) is the perturbation of inertia due to isostatic adjustment of the Earth and $*$ is the time convolution.

Induced rotational deformation
The forcing function for induced rotational deformation of a rigid Earth can be written in complex notation as in equation 5.17. But in this case the perturbations in the moments of inertia are the result of the degree 2 contribution of the gravitational potential (ΔI^R_{i3} (i=1,2,3)) as given by *Sabadini and Vermeersen* [2004] in their equations 3.34 and 3.35. This gives:

$$\Phi_R = \frac{\Delta I^R_{13}}{C-A} + i\frac{\Delta I^R_{23}}{C-A} \approx \frac{k^T_2}{k_f}\boldsymbol{m} \tag{5.19}$$

where k^T_2 is the tidal Love number 2 and k_f denotes the fluid Love number (also called the secular Love number) defined as:

$$k_f = \frac{3G(C-A)}{a^5\Omega^2} \tag{5.20}$$

in which G is the universal gravitational constant and a is the mean radius of the Earth. If the Earth is assumed to be rigid Eulerian free precession occurs. But geophysical forcing occurs the so-called Chandler wobble arises, which has a period of four months larger than the Eulerian free precession period as result of the elastic properties of the Earth. This wobble is the result of the adjustment of the equatorial bulge. Assume an initial condition where the rotation axis coincides with the axis perpendicular to the plane of equatorial flattening. As a result of a mass change the rotation axis will change its position to the maximum moment of inertia and the Chandler wobble is the result. If we move ϕ_R to the left side in equation 5.15 and use equation 5.19 we get:

$$i\frac{\dot{\boldsymbol{m}}}{\sigma_r} + \big(1 - \frac{k^T_2}{k_f}\big)\boldsymbol{m} = \Phi_L \tag{5.21}$$

or, rearranged:

$$i\frac{\dot{\boldsymbol{m}}}{\sigma_0} + \boldsymbol{m} = \frac{k_f}{k_f - k^T_2}\Phi_L \tag{5.22}$$

in which

$$\sigma_0 = \big(1 - \frac{k^T_2}{k_f}\big)\sigma_r \tag{5.23}$$

is the Chandler wobble frequency with a four months larger period as a result of the factor k^T_2/k_f. To calculate the polar wander only the secular term of polar wander is evaluated and the periodic term is neglected: $i\dot{\boldsymbol{m}}/\sigma_r = 0$ [*e.g.*, *Vermeersen and Sabadini*, 1996a; *Mitrovica and Milne*, 1998]. The two most commonly used methods to transform the linearized Liouville equation to the Laplace domain and back to the time domain are given by *Sabadini et al.* [1982] and *Wu and Peltier* [1984]. Both theories are basically equivalent to each other as discussed by *Vermeersen and Sabadini* [1996a] and *Mitrovica and Milne* [1998]. In this thesis the method of *Wu and Peltier* [1984] is adopted because it is easier to implement into the existing sea level code. Using equations 5.15 and 5.18 and assuming secular polar wander gives the linearized Liouville equation in the time domain:

$$\boldsymbol{m}(t) = \frac{1}{C-A}[\Delta I^R_{i3}(t) + k^L_2(t) * \Delta I^R_{i3}(t)] + \frac{k^T_2(t)}{k_f(t)} * \boldsymbol{m}(t) \qquad (i = 1, 2) \tag{5.24}$$

and

$$m_3(t) = \frac{1}{C}[\Delta I^R_{33}(t) + k^L_2(t) * \Delta I^R_{33}(t)] \tag{5.25}$$

Traditionally for GIA calculations the linearized Liouville theory is developed within the Laplace-transformed domain, because of the difficulties concerning the calculation of $\boldsymbol{m}$ with respect to the time convolutions [*e.g.*, *Wu and Peltier*, 1984]. The Laplace transformations of equation 5.24 and equation 5.25 are respectively:

$$\boldsymbol{m}(s) = \frac{1}{C-A}\frac{\Delta I_{i3}^{R}(s)[1+k_2^L(s)]}{[1-(k_2^T(s)/k_f)]} \qquad (i=1,2) \tag{5.26}$$

and

$$m_3(s) = \frac{1}{C}\Delta I_{33}^{R}(s)[1+k_2^L(s)] \tag{5.27}$$

where the viscoelastic Love numbers (derived in chapter 3) in the Laplace transformed domain are expressed by:

$$k_2^L(s) = k_2^{L,E} + \sum_{k=1}^{K}\frac{r_k'^{\ell=2,L}}{s+s_k^{\ell=2}} \tag{5.28}$$

$$k_2^T(s) = k_2^{T,E} + \sum_{k=1}^{K}\frac{r_k'^{\ell=2,T}}{s+s_k^{\ell=2}} \tag{5.29}$$

in which s is the Laplace transform variable. The fluid Love number k_f is often approximated by the fluid limit, $s=0$, of the s-domain k_2^T Love number [*e.g.*, *Wu and Peltier*, 1984]:

$$k_f \sim k_2^T(s=0) = k_2^{T,E} + \sum_{k=1}^{K}\frac{r_k'^{\ell=2,T}}{s_k} \tag{5.30}$$

The correctness of this approximation was questioned when *Nakada* [2002] introduced a paradox, namely the predictions of present-day TPW speed for the case of a viscoelastic lithosphere do not converge to the predictions of an elastic lithosphere. *Mitrovica et al.* [2005] suggested that this paradox originates from an inaccuracy in the traditional rotation theory and introduced the revised rotation theory that is insensitive for lithospheric rheology or thickness. The revised rotation theory proposes an alternative theoretical treatment of the rotation theory in which the fluid Love number is calculated for a model without elastic lithosphere (LT=0), and is corrected for the excess ellipticity to include the other geophysical contributions. The excess ellipticity is determined by taking the difference between the observed fluid number, calculated by using the observed polar and equatorial moments of inertia in equation 5.20, and the fluid number obtained by the second-order hydrostatic theory which gives $\beta = 0.9382 - 0.9305 = 0.0077$. The second-order hydrostatic theory treats the Earth as an inviscid fluid to determine e.g. the equilibrium shape of a rotating Earth. Another approach is to adopt the observed fluid Love number and scale it to account for inaccuracies in the Love number theory. These analytical theoretical treatments ultimately lead to identical expressions for the fluid Love number:

$$k_f \sim k_2^T(s=0; LT=0) + \beta \tag{5.31}$$

Although the revised rotation theory is an improvement of the general rotation theory, it is not used in this study because it is not yet implemented in the sea level theory of *Milne and Mitrovica* [1998]. The alternative expression for the fluid Love number in the revised rotation theory has profound implications on the previously adopted transformation from the Laplace domain to the time domain, which is not valid anymore. This holds that the derivation has to be done over again. So *Mitrovica et al.* [2005] solved the the Liouville equation numerically in the time domain (equation 5.24). At the moment J.X.M. Mitrovica solved the transformation and is writing a paper on this subject.
The transformation from the Laplace domain to the time domain gives the following equations [*Milne and Mitrovica*, 1998]:

$$\langle m_i(t)\rangle = \frac{\Omega}{A\sigma_0}\Big[D_1\Delta I_{i3}^R(t) + D_2\int_0^t \Delta I_{i3}^R(t')dt' + \sum_{k=1}^{K-1}E_k(\Delta I_{i3}^R(t) * e^{-\lambda_k t})\Big] \qquad (i=1,2)$$

(5.32)

and

$$m_3(t) = -\frac{1}{C}\Big[D_1 \Delta I_{33}^R(t) + \sum_{k=1}^{K} r_k^{\ell=2,L} (\Delta I_{33}^R(t) * e^{-s_k^{\ell=2} t})\Big] \tag{5.33}$$

where the symbol $\langle\rangle$ signifies that the Chandler wobble has been removed from the response by deleting the corresponding rotational mode [*Mitrovica and Milne*, 1998] and λ_k are the roots of the polynomial:

$$Q(s) = \frac{\sum_{q=1}^{K}\left[\frac{r'^{\ell=2,T}_q}{s_q^{\ell=2}} \prod_{p\neq q}(s + s_p^{\ell=2})\right]}{\sum_{j=1}^{K} \frac{r'^{\ell=2,T}_k}{s_j^{\ell=2}}} \tag{5.34}$$

The constants D_1, D_2 and E_k used in equations 5.32 and 5.33 are defined as:

$$D_1 = 1 + k_2^{L,E} \tag{5.35}$$

$$D_2 = \frac{l_s \prod_{p=1}^{K} s_p^{\ell=2}}{\prod_{p=1}^{K-1} \lambda_p} \tag{5.36}$$

and

$$E_k = \frac{-\left[\frac{l_s \prod_{p=1}^{K}(s_p^{\ell=2} - \lambda_k)}{\lambda_k} + \sum_{q=1}^{K} \frac{r'^{\ell=2,L}_q}{s_q^{\ell=2}} \prod_{p\neq q}(s_p^{\ell=2} - \lambda_k)\right]}{\prod_{q\neq k}^{K-1}(\lambda_q - \lambda_k)} \tag{5.37}$$

where l_s is known as the isostatic factor, which is controlled by the thickness of the lithosphere [*Wu and Peltier*, 1982] and defined as:

$$l_s = 1 + k_2^{L,E} + \sum_{p=1}^{K} \frac{r'^{\ell=2,L}_p}{s_p^{\ell=2}} \tag{5.38}$$

Milne and Mitrovica [1998] derived general expressions which relate the ΔI_{i3}^R in equations 5.32 and 5.33 to the spherical harmonic coefficients of an arbitrary surface load. The expression for the 13-component of the perturbation of the inertia tensor (equation 43a in [*Milne and Mitrovica*, 1998]) is corrected by a minus sign in front of the equation. These expressions are defined as step increments:

$$[\delta \Delta I_{13}^R]^n = -\frac{4}{3}\sqrt{\frac{6}{5}} a^4 \pi \;\; Re[\rho_i \delta I_{21}^n + \rho_w \delta S_{21}^n] \tag{5.39}$$

$$[\delta \Delta I_{23}^R]^n = -\frac{4}{3}\sqrt{\frac{6}{5}} a^4 \pi \;\; Im[\rho_i \delta I_{21}^n + \rho_w \delta S_{21}^n] \tag{5.40}$$

$$[\delta \Delta I_{33}^R]^n = \frac{8}{3\sqrt{5}} a^4 \pi \;\; Re[\rho_i \delta I_{20}^n + \rho_w \delta S_{20}^n] \tag{5.41}$$

in which I_{ij} and S_{ij} are the spherical harmonic expressions for the ice and sea load of degree i and order j. The series of step increments can be written as a time series of inertia perturbations:

$$\Delta I_{i3}^R(t) = \sum_{n=1}^{N} [\delta \Delta I_{i3}^R]^n H(t - t_n) \qquad (i = 1, 2) \tag{5.42}$$

The time convolution used in equations 5.32 and 5.33 can also be written in an alternative analytic expression [*Mitrovica and Milne*, 1998]:

$$\Delta I_{i3}^R(t) * e^{-\lambda_k t} = \frac{1}{\lambda_k} \sum_{n=1}^{K} [\delta \Delta I_{i3}^R]^n H(t - t_n)(1 - e^{-\lambda_k (t - t_n)}) \qquad (i = 1, 2) \tag{5.43}$$

The alternative expression of the convolution makes it possible to look in detail into the physical interpretation of the equation. The rotational response of a viscoelastic planet, as result of the k^{th} surface load increment, involves no instantaneous perturbation in the position of the rotation pole (also discussed in [*Lambeck*, 1980]). After the load is applied the rotation vector undergoes a damped oscillation with a decay time of $1/\lambda_k$.

5.2 Sea level equation for a rotating Earth

On a rotating Earth the geoid and solid surface are perturbed by both a changing rotational potential and a changing surface load. The perturbation of the geoid and solid surface due to the rotational potential are determined in the same way as the surface load problem described in section 4.2. To calculate the sea level response to a changing potential, instead of load Love numbers, tidal Love numbers are introduced (defined in chapter 3). These describe the response of a Maxwell viscoelastic Earth model to a general potential forcing. First the perturbation of the rotational potential will be derived and then the implementation into the sea level equation will be treated. The rotational potential perturbation at the surface of a spherical Earth can be written as [*e.g.*, *Lambeck*, 1980]:

$$U_R(\gamma) = \frac{1}{3}\omega(t)^2a^2 - \frac{1}{3}\omega(t)^2a^2P_{2,0}(cos\gamma) \tag{5.44}$$

in which $\omega(t)$ is defined in equation 5.10 but now dependent on time and γ is the angular distance between $\omega(t)$ and an arbitrary field point (θ, ψ). The Legendre polynomial of degree 2 and order 0 is defined as:

$$P_{2,0}(cos\gamma) = \frac{1}{5}\sum_{m=-2}^{2} Y^{\dagger}_{2,m}(\theta', \psi')Y_{2,m}(\theta, \psi) \tag{5.45}$$

where (θ', ψ') are the coordinates of $\omega(t)$. The perturbation to the rotational potential from the equilibrium value depends on m_i and can be written as [*Milne and Mitrovica*, 1998]:

$$\Lambda(\theta, \psi, t) = \Lambda_{0,0}(t)Y_{0,0}(\theta, \psi) + \sum_{m=-2}^{2} \Lambda_{2,m}(t)Y_{2,m}(\theta, \psi) \tag{5.46}$$

with the individual coefficients defined as:

$$\Lambda_{0,0}(t) = \frac{a^2\Omega^2}{3}[m^2(t) + 2m_3(t)] \tag{5.47}$$

$$\Lambda_{2,0}(t) = \frac{a^2\Omega^2}{6\sqrt{5}}[m_1^2(t) + m_2^2(t) - 2m_3^2(t) - 4m_3(t)] \tag{5.48}$$

$$\Lambda_{2,1}(t) = \frac{a^2\Omega^2}{\sqrt{30}}[m_1(t)(1 + m_3(t)) - im_2(t)(1 + m_3(t))] \tag{5.49}$$

$$\Lambda_{2,2}(t) = \frac{a^2\Omega^2}{\sqrt{5}\sqrt{24}}[(m_2^2(t) - m_1^2(t)) + i2m_1(t)m_2(t)] \tag{5.50}$$

where i represents the complex number $\sqrt{-1}$ and

$$\Lambda_{2,-m}(t) = (-1)^m\Lambda^{\dagger}_{2,m} \tag{5.51}$$

The rotational potential is completely described by degree 0 and degree 2 harmonics. Perturbations of m_3 due to GIA are several orders smaller then the perturbations in m_1 or m_2. This results in the fact that the $\Lambda_{2,1}(t)$ coefficient is dominant in equation 5.46 and accounts for about 99 percent of the signal [*Milne and Mitrovica*, 1998]. So the potential forced sea level response due to GIA is dominated by degree 2 and order 1 harmonic signature, which is also discussed in [*Han and Wahr*, 1989]. The tidal Green's function for the gravitational potential perturbation at the undeformed surface and the radial displacement of the solid surface at degree ℓ are respectively:

$$\Phi^T_\ell(t) = \delta(t) + k^{T,E}_\ell \delta(t) + \sum_{k=1}^{K} {r'}^{\ell,T}_k e^{-s^\ell_k t} \tag{5.52}$$

and

$$\Gamma^T_\ell(t) = \frac{1}{g}\left[h^{T,E}_\ell \delta(t) + \sum_{k=1}^{K} r^{\ell,T}_k e^{-s^\ell_k t}\right] \tag{5.53}$$

The tidal Green's functions depend on time only, in contrast to the load Green's functions (equation 4.4 and 4.3) which depend on both space and time. So the perturbation to the geopotential and solid surface radial displacement are calculated by convolving the time variation of both the rotational potential (equation 5.46) with the Green's functions (equation 5.52 and 5.53). The tidal geoid anomaly and the surface radial displacement are given by:

$$G^T_{\ell,m}(t) = \frac{1}{g}\int_{-\infty}^{t} \Lambda_{\ell,m}(t')\Phi^T_\ell(t-t')dt' + \frac{\Delta\Phi^T(t)}{g}\delta_{\ell,0}\delta_{m,0} \tag{5.54}$$

and

$$R^T_{\ell,m}(t) = \int_{-\infty}^{t} \Lambda_{\ell,m}(t')\Gamma^T_\ell(t-t')dt' \tag{5.55}$$

The time history of the rotational potential is modeled, just as for the load, as a series of Heaviside loading increments:

$$\Lambda_{\ell,m}(t) = \sum_{n=1}^{N} \delta\Lambda^n_{\ell,m} H(t-t_n) \tag{5.56}$$

Filling equation 5.56 into equation 5.54 and 5.55 gives:

$$\begin{aligned} G^T(\theta,\psi,t) = \sum_{\ell,m} \Big\{ &(1+k^{T,E}_\ell)\frac{\Lambda_{\ell,m}(t)}{g} + \sum_{n=1}^{N}\frac{\delta\Lambda^n_{\ell,m}}{g}\sum_{k=1}^{K}\frac{{r'}^{\ell,T}_k}{s^\ell_k}[1-e^{-s^\ell_k(t-t_n)} + \\ &\frac{\Delta\Phi^T(t)}{g}\delta_{\ell,0}\delta_{m,0}\Big\}Y_{\ell,m}(\theta,\psi) \end{aligned} \tag{5.57}$$

and

$$R^T(\theta,\psi,t) = \sum_{\ell,m}\Big\{h^{T,E}_\ell \frac{\Lambda_{\ell,m}(t)}{g} + \sum_{n=1}^{N}\frac{\delta\Lambda^n_{\ell,m}}{g}\sum_{k=1}^{K}\frac{r^{\ell,T}_k}{s^\ell_k}[1-e^{-s^\ell_k(t-t_n)}\Big\}Y_{\ell,m}(\theta,\psi) \tag{5.58}$$

The contribution of the rotational potential to the sea level change is given by the difference between equation 5.57 and 5.58 multiplied by the ocean function. When this contribution is added to the sea level equation for the surface mass loading derived in chapter 4 the following equation is obtained:

$$\begin{aligned} &\sum_{\ell,m} S_{\ell,m}(t)Y_{\ell,m}(\theta,\psi) = \\ &\qquad C(\theta,\psi,t)\sum_{\ell,m}\Bigg\{E^L_\ell T_\ell(\rho_i I_{\ell,m}(t) + \rho_w S_{\ell,m}(t)) + E^T_\ell \frac{\Lambda_{\ell,m}(t)}{g} + \\ &\qquad \sum_{n=1}^{N}\Big[T_\ell(\rho_i \delta I^n_{\ell,m} + \rho_w \delta S^n_{\ell,m})\beta^L_\ell(t-t_n) + \frac{\delta\Lambda^n_{\ell,m}}{g}\beta^T_\ell(t-t_n)\Big] \times \\ &\qquad H(t-t_n) + \frac{\Delta\Phi(t)}{g}\delta_{\ell,0}\delta_{m,0}\Bigg\}Y_{\ell,m}(\theta,\psi) \end{aligned} \tag{5.59}$$

with T_ℓ defined in equation 4.27 and

$$E_\ell^T = 1 + k_\ell^{T,E} - h_\ell^{T,E} \tag{5.60}$$

and

$$\beta_\ell^T(t - t_n) = \sum_{k=1}^{K} \frac{({r'}_k^{\ell,T} - r_k^{\ell,T})}{s_k^\ell}\,[1 - e^{-s_k^\ell(t-t_n)}] \tag{5.61}$$

Equation 5.59 is the spectral form of the sea level equation for a Maxwell viscoelastic Earth model excited by both a surface mass load redistribution and a changing rotational potential.

5.3 Solving the sea level equation for a rotating Earth

The pseudo-spectral approach (as described in section 4.3.3) is used to calculate the sea level for a rotating Earth. The same iterative process is used but $R_{p,q}(t_j)$ from equation 4.30 is now replaced by:

$$\begin{aligned}[R_{p,q}(t_j)]^i &= E_p^L T_p\big(\rho_i I_{p,q}(t_j) + \rho_w S_{p,q}(t_{j-1}) + \rho_w[\delta S_{p,q}^j]^i\big) + E_p^T \frac{\delta\Lambda_{p,q}^j}{g} \\ &+ \sum_{n=1}^{N} T_p(\beta_p^L(t_j - t_n)(\rho_i \delta I_{p,q}^n + \rho_w \delta S_{p,q}^n)) + \beta_p^T(t_j - t_n)\frac{\delta\Lambda_{p,q}^n}{g}\end{aligned} \tag{5.62}$$

In the first step of the iteration the sea level change is defined as the eustatic change in sea level (equation 4.36) from which the perturbation of the rotational potential is calculated. In the second step of the iteration the sea level is determined by using the approximated values. This procedure is repeated until a certain level of convergence is reached between two iterations (equation 4.37). The perturbation of inertia is calculated from the sea-load and ice-load and is used to compute the rotational potential which is used to calculate $R_{p,q}(t_j)$ as can be seen in figure 5.2. In order to determine the rotational potential the rotational roots have to be determined from a polynomial (equation 5.34), which is constructed from Love numbers and isostatic roots. This is done using rootfinding procedures, which will be discussed in the next section.

Rootfinding procedures

There are different methods available to calculate the root of the polynomial described in chapter 5 equation 5.34. The different methods used in this research are based on methods described in Numerical Recipes for FORTRAN 77 [*Press et al.*, 1992]. In this study three methods are selected to determine the rotational roots:

- Laguerre's method and a root polishing method
  In this method the roots of the polynomial of equation 5.34 are determined. This method is a complex method which uses a relation between the polynomial, its roots and derivatives. A major advantage of Laguerre's method is that it is almost guaranteed to converge to some root of the polynomial no matter where the initial approximation is chosen. Although it must be noted that the theoretical proof of the algorithm is limited. To increase the accuracy of the result a root polishing method based on Newton-Raphson is used.
- Eigenvalue method
  Also in this method the roots of the polynomial of equation 5.34 are determined. The eigenvalue method uses the eigenvalues of the matrix A to determine the roots of the characteristic polynomial $P(x) = det[A - xI]$. This characteristic polynomial is again equivalent to a general polynomial [*Press et al.*, 1992].

- Ridder's method
  The roots can also be determined by constructing a polynomial from the isostatic roots and using Ridder's method to find the rotational roots. A general function is determined with a set of parameters x_i [*Vermeersen and Sabadini*, 1996a]:

  $$x_i = \frac{\sigma_r k_i^T}{k_f} \tag{5.63}$$

  where x_i are renormalized strengths of the load relaxation modes i. Ridder's method uses polynomial extrapolation to evaluate a function in an interval and works faster than the much used bisection method, because it uses fewer function evaluations.

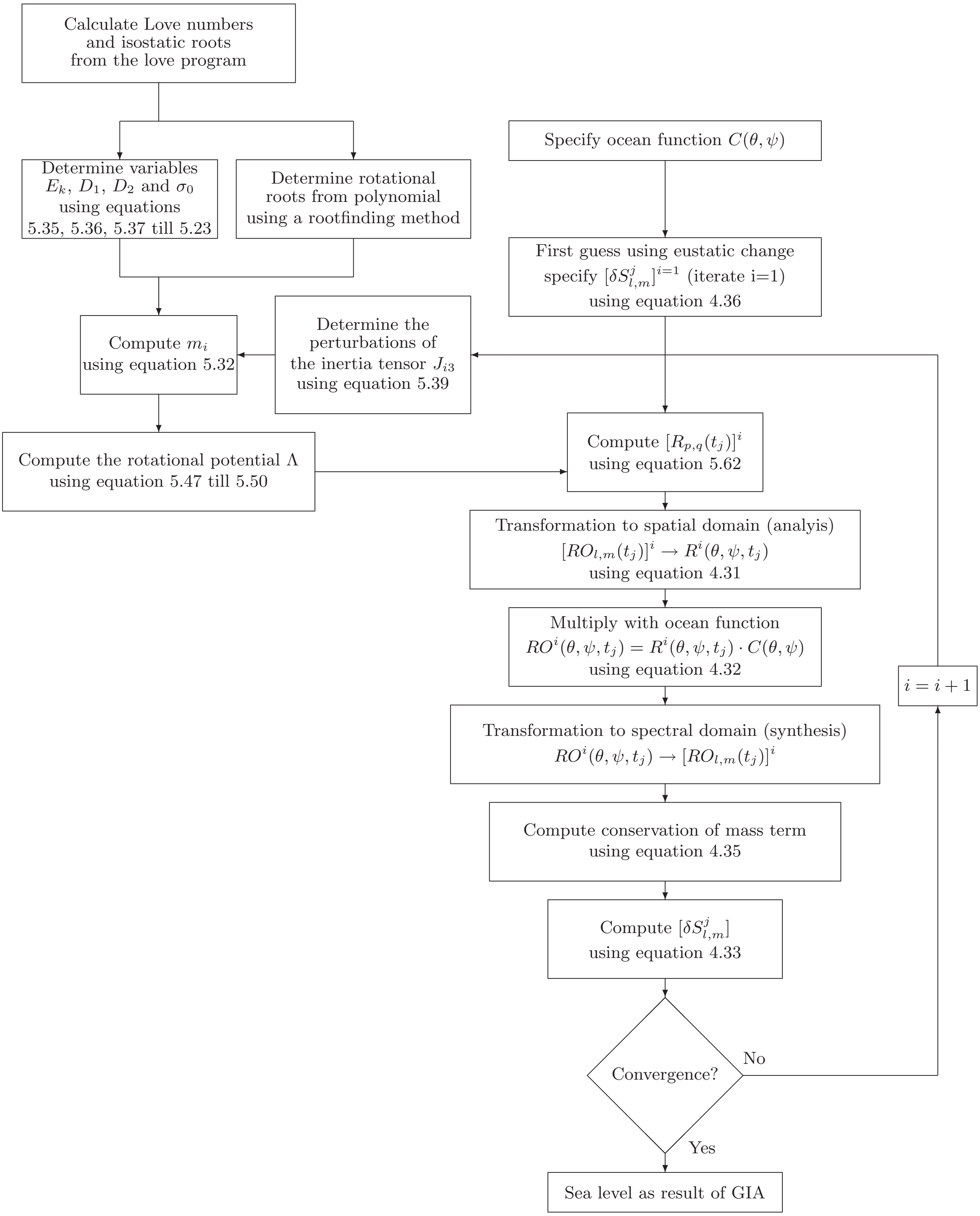

Figure 5.2 Pseudo-spectral solution to the sea level equation including rotation.

Chapter 6

Model description

Now the sea level equation of a rotating Earth is determined it will be used to model GIA with different combinations of Earth models and ice models in chapter 7. But first the input of the model with respect to the selected Earth- and ice models will be introduced in this chapter. A general rigidity and density structure is introduced together with three different mantle viscosity profiles (VM1, VM2, KL) in section 6.1, followed by a discussion on three selected ice models (ICE-3G, ICE-5G and RSES) in section 6.2. Finally in section 6.3 the applied topography is treated shortly.

6.1 Earth models

During the last decades, GIA studies have been frequently used to determine the mantle viscosity, mostly by inversion studies in combination with rotational data. In this section three Earth models will be discussed and each of the considered Earth models will have the same radial density and rigidity structure but a different radial viscosity structure.

6.1.1 Radial rigidity and density structure

The rigidity and density structure used in this thesis is derived from the Preliminary Reference Earth model (PREM) created by *Dziewonski and Anderson* [1981], which contains 94 layers. At each boundary the rigidity and density parameters change discontinuously and inside the layer the variation is assumed to be polynomial. There are two possibilities to derive a model of less layers: by volume-averaging or keeping the discontinuities the same as in PREM (also referred to as fixed boundary). The volume averaged is preferred because it is in closer agreement with models that have more layers or a continuum distribution [*Vermeersen and Sabadini*, 1999]. The volume-averaging procedure sums the contribution of each PREM layer with respect to the rigidity and density properties within the defined layer, which is then weighted according to the radial distance. The rigidity and density parameters for the 6 layer Earth model obtained from the PREM model by volume averaging are found in table 6.1.

6.1.2 Radial viscosity structure

A much used method to determine the radial viscosity structure of the Earth is by analyzing observations related to geodynamical deformation of the Earth. The mantle viscosity can be inferred by observations of the GIA during the ice-age cycles and observations related to mantle convection. Observations of GIA (e.g. coastlines, perturbations in the Earth's gravitational field and changes in Earth's rotation) have been used to constrain both the thickness of the elastic lithosphere and the viscosity of the viscoelastic mantle. Also observations related to mantle convection (e.g. perturbations of large scale geoid

layer	radius $[km]$	density $[kg/m^3]$	rigidity $[N/m^2]$	description
1	6371 - 6250	3188.01	$0.602178 \cdot 10^{11}$	lithosphere
2	6250 - 5951	3460.22	$0.742623 \cdot 10^{11}$	shallow upper mantle
3	5951 - 5701	3885.88	$0.109871 \cdot 10^{12}$	transient zone
4	5701 - 5041	4554.19	$0.183485 \cdot 10^{12}$	shallow lower mantle
5	5041 - 3480	5110.06	$0.245394 \cdot 10^{12}$	deep lower mantle
6	3480 - 0	10925.0	0.00	inviscid fluid core

Table 6.1 Volume averaged density and rigidity stratification from PREM for the 6 layer Earth model.

and gravity anomalies) have been used to constrain mantle viscosity. In this study three different radial viscosity stratifications are used which are mostly based on the inference by GIA observations. These models are VM1, VM2 and the Kaufmann-Lambeck model which are treated in more detail below.

VM1 Earth model

The VM1 model is a simple model of the radial viscoelastic structure used by *Tushingham and Peltier* [1991] to create ICE-3G. The radial viscoelastic structure model was later named VM1 by *Peltier* [2002]. This inference was based upon solutions of the forward problem, in which an a priori model of the deglaciation history (ICE-1) [*Peltier and Andrews*, 1976a] was used. When the VM1 model was employed 15 years ago, the forward modeling of the GIA process showed that RSL, free air gravity, and Earth rotation constraints are very well fitted with a relatively simple model of the radial viscoelastic structure [*Peltier*, 1989]. This results in a radial viscosity structure with a elastic lithosphere thickness of 120 km, an upper mantle viscosity of $1 \cdot 10^{21} Pas$ and a lower mantle viscosity of $2 \cdot 10^{21} Pas$.

VM2 Earth model

The VM2 model is the successor of VM1 and has a completely different mantle viscosity stratification, which is the result of different assumptions as can be seen in figure 6.1). This model also is used by *Peltier* [1994, 2004] to create ICE-4G and ICE-5G. The VM2 model is derived on the basis of Bayesian inversion [*Tarantola and Valette*, 1982], in which VM1 is used as a starting model. The improvement is accomplished by including 23 site-dependent relaxation times from Canada and Fennoscandia (Scandinavia), a relaxation time spectrum for the rebound of Fennoscandia and the observed rate of rotation to constrain the viscosity [*Peltier*, 2002]. The applied viscosity stratification as shown in table 6.2 is a simplification of the VM2 model as derived by *Wang and Wu* [2006].

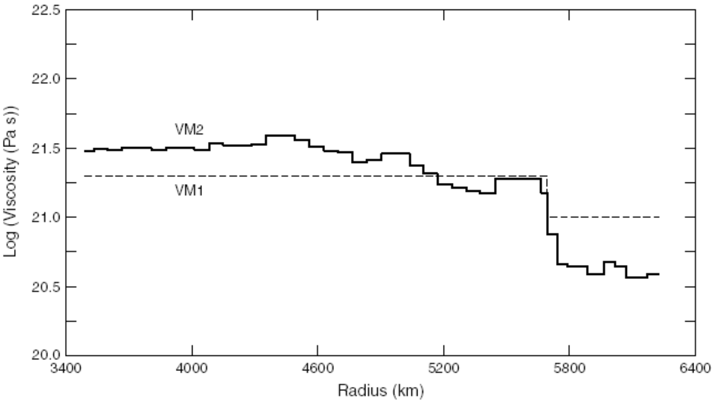

Figure 6.1 Radial profiles of mantle viscosity of VM1 and VM2. Source: [*Peltier*, 2002].

Kaufmann-Lambeck Earth model

The third Earth model is the Kaufmann-Lambeck (KL) Earth model, which is derived by *Kaufmann and Lambeck* [2002] by using an inverse procedure to infer mantle viscosity profiles from observations related to the GIA process and the RSES ice model (see section 6.2.3). A formal inverse procedure is used to infer the radial viscosity profile by solving a damped, weighted, nonlinear inverse problem for the viscosity profile [*e.g.*, *Mitrovica and Peltier*, 1991]. The observational data includes Late Pleistocene and Holocene coastlines, present-day sea level and crustal response, and rotational data. The rotational data includes both the observed TPW speed and observed rate of change of the spherical harmonic degree-two component of the Earth's gravitational field ($\dot{J}_2$). To reduce the least squares misfit not all available data is used. The radial viscosity profile is based on 569 RSL sites from Scandinavia, the observed present-day TPW-speed and the present-day $\dot{J}_2$. The result is a radial viscosity structure with an elastic lithosphere thickness of 80 km, a volume averaged upper mantle viscosity of $7 \cdot 10^{20} Pas$ and a volume averaged lower mantle viscosity of $2 \cdot 10^{22} Pas$. The volume averaged lower mantle viscosity is used because of lack of detailed information of the viscosity stratification suggested by *Kaufmann and Lambeck* [2002]. The simplified model we apply will have a modified elastic lithosphere thickness of 120 km instead of 80 km. This inconsistency will not have a large impact on the simulated present-day TPW, because the relatively high lower mantle viscosity results in a present-day TPW almost insensitive to variations in lithospheric thickness, which is the case in both the classical and revised rotation theory [*Mitrovica et al.*, 2005].

Table 6.2 lists the different viscosity stratifications used in this study.

layer	radius $[km]$	VM1 viscosity $[Pas]$	VM2 viscosity $[Pas]$	KL viscosity $[Pas]$
1	6371 - 6250	elastic	elastic	elastic
2	6250 - 5951	$1 \cdot 10^{21}$	$6 \cdot 10^{20}$	$7 \cdot 10^{20}$
3	5951 - 5701	$1 \cdot 10^{21}$	$6 \cdot 10^{20}$	$7 \cdot 10^{20}$
4	5701 - 5041	$2 \cdot 10^{21}$	$1.6 \cdot 10^{21}$	$2 \cdot 10^{22}$
5	5041 - 3480	$2 \cdot 10^{21}$	$3 \cdot 10^{21}$	$2 \cdot 10^{22}$
6	3480 - 0	0.00	0.00	0.00

Table 6.2 Viscosity stratification of VM1, VM2 and the Kaufmann-Lambeck (KL) Earth model.

6.2 Ice models

In the last years, multiple ice models have been developed which are generally created with the same method. The common approach to create an ice model is by placing constraints on the extent of the ice sheets and the distribution of ice within the ice sheets. The constraints for the extent of the ice sheet are determined by geological evidence in the form of glacial tills, striations, moraines and other features which indicate that an ice sheet once covered the land. With these constraints it is possible to determine the boundaries of the ice sheets at a certain time, which is mostly limited to the last Pleistocene deglaciation. In order to determine the distribution of ice (ice height) within these boundaries mostly RSL data, coral reefs and oxygen isotope records ($\delta^{18}O$) of ocean sediments is used. The relative sea level can be locally constrained at different times by the following observations as *Lambeck* [1998] used for the construction of ice sheets of Fennoscandia:

- Geographical position of isolation basins, which were created when the sea-level retreated. When the age-height observations of a number of basins are combined, in some instances, a sea-level curve of the area in question can be formed.
- Varve records contained in deltaic sediments. A varve is a rhythmic sequence of sediments deposited in annual cycles in glacial lakes at the edge of a glacier.
- Shorelines of distinct ages with relatively constant sea level, which can be correlated over long distances.

- Submerged peat deposits or present depths of shell beds which give an indication of the upper limit of past sea level.

Global constraints on eustatic sea level can be placed by using observations outside the ice covered regions [*Tushingham and Peltier*, 1991]:

- Analyzing age and elevation of the coral reefs using Uranium/Thorium and carbon dating.
- Oxygen isotope ($\delta^{18}O/\delta^{16}O$) ratio variation in sea water found in micro fossils. These marine sediments give a complete record of variation in ^{16}O isotopes in the sea during the past millions of years and are an indication for the changes in global ice volume. The ice volume fluctuations affect the ratio of light ^{16}O and heavy ^{18}O isotopes in sea water. During the glacial period the water in the oceans is depleted in ^{16}O. So during an interglacial period the ice sheets melt, raising the sea level and enriching the oceans again with ^{16}O.

The most important and crucial method to date the coral, sample deposits or sediments is radiocarbon dating. Radiocarbon dating is a radiometric dating method that uses the naturally occurring isotope ^{14}C to determine the age of carbonaceous materials up to 60 kiloyears (kyr) before present (BP[1]). ^{14}C is a radioactive isotope of carbon, with a half-life of 5.73 kyr, and would have disappeared a long time ago, if it was not continuously created through collisions of neutrons generated by cosmic rays with nitrogen in the upper atmosphere. The ^{14}C ends up as a trace component in atmospheric carbon dioxide (CO_2) which is acquired by an organism during its lifetime. When an organism dies, it ceases to acquire new ^{14}C and the proportion of ^{14}C left when the remains of the organism are examined provides an indication of the time lapsed since its death (http://en.wikipedia.org/wiki/Radiocarbon_dating). Carbon dating is used for dating objects not older than 50 kyr BP because at this point all radioactive ^{14}C has decayed. Recently the ^{14}C time is found to deviate from actual, calendar, time with about 15 percent. This is the result of the variation in the level of atmospheric ^{14}C during the span of time that can be radiocarbon dated. The level ^{14}C of is affected by variations in the cosmic ray intensity, ^{14}C release from reservoirs (e.g. organic matter, the ocean, ocean sediments and sedimentary rocks) and human activity. The raw radiocarbon dates are therefore calibrated to give calendar dates. The calibration is accomplished by dating and comparing tree rings and by simultaneously dating a collection of coral samples using both the ^{14}C method and Uranium/Thorium (U/Th) method. The U/Th method can be used to date objects with a certain chemical composition which are older than 50 kyr BP by measuring the decay of U/Th. In practise it is possible to date objects until an age of 800 kyr BP.

With the use of the constraints summarized above, both the radial viscoelastic structure and deglaciation history have to be determined. The solution of this inverse problem can be obtained in an iterative way as explained in the next section. In the first iterative step the deglaciation history is given and the radial viscoelastic structure is determined. In the second step the deglaciation history is refined given an acceptable radial viscoelastic structure.

The evaluated ice models in the next section are the older and frequently used ICE-3G model and the more recent ICE-5G and RSES model. It must be noted that the Earth model used to create the ice model is implicitly present in the ice model and should always be used together to obtain correct results.

6.2.1 ICE-3G ice model

A much used ice model in a wide range of GIA and rotation studies is ICE-3G. This model was developed by *Tushingham and Peltier* [1991] and describes the deglaciation history of

---

[1] BP represents the number of calibrated years before 1950 and bp is used in case of uncalibrated years before 1950

the late Pleistocene deglaciation. ICE-3G starts at the last glacial maximum (LGM) at 18 kyr bp and finishes at 5 kyr bp. When in this thesis a complete ice cycle (glaciation and deglaciation) is considered a 90 kyr linear glaciation is assumed. It must be noted that this timescale is based on ^{14}C and not on the calendar timescale. The deglaciation histories of the Laurentide and Fennoscandian ice sheets are used in the forward solution to get a best fit to RSL data (from coral reefs and $\delta^{18}O$), gravity anomaly measurements and observed drift of the rotation axis. This resulted in an Earth model which has a lithospheric thickness of 120 km and a upper mantle viscosity of $1 \cdot 10^{21}$ Pa s and a lower mantle viscosity of $2 \cdot 10^{21}$ Pa s, also denoted as VM1 (see section 6.1). The inverse solution, to determine the ice thickness, is obtained by varying the ice thickness over areas covered with ice sheets at specified times during deglaciation, until a best fit is obtained between the resulting sea-level curves and dated sea levels at 192 (mostly near-field) sites. The ICE-3G model is constructed using a finite disc grid which consists of 808 circular discs of different sizes. This method might create inaccurate ice sheets because it can result in regions where two discs overlap and areas which are not covered as can be seen in figure 6.3.

In order to obtain the ICE-3G model some assumptions were made. First of all no shoreline evolution is considered for simplicity and isostatic equilibrium at LGM is assumed. Because of the time discretization minor advances and retreats on timescales smaller then 1 kyr are not included. It is also assumed that the ice is melted instantaneously at the time steps (Heaviside loading is applied).

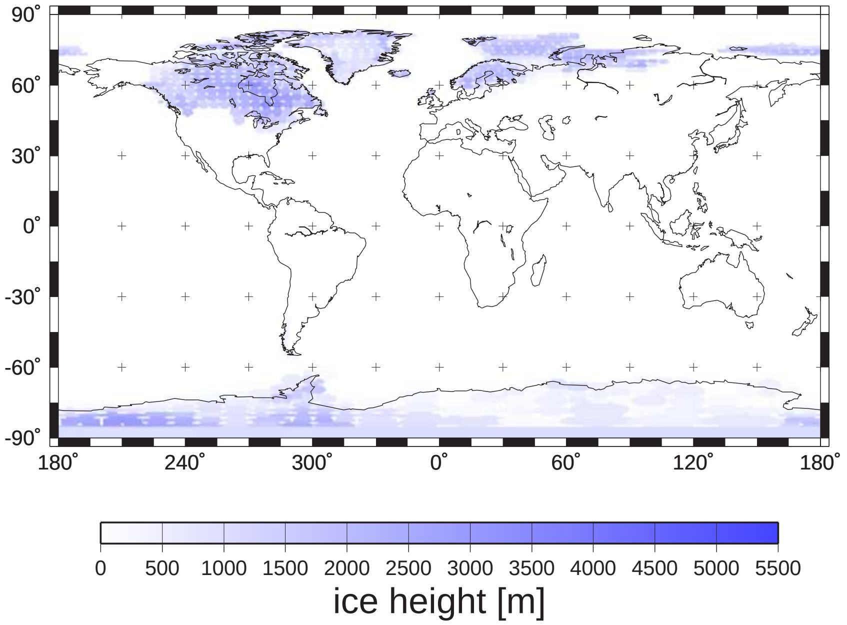

Figure 6.2 Global distribution of the ice melted during the last deglaciation period assumed by the ICE-3G ice model.

Ice model characteristics

The ICE-3G ice model includes ice height data of the last deglaciation period and provides ice height information from 18 kyr bp till 5 kyr bp (see figure 6.6). The model assumes a total ice mass which melts from LGM till the end of deglaciation of $3.66 \cdot 10^{19}$ kg, which gives an equivalent sea level rise of about 101 m in this study. It must be noted that ICE-3G is given in uncalibrated years in contrast with the other ice models. Taking this into account it is somewhat odd that previous studies using the ICE-3G ice model assumed an ice cycle period of 100 kyr, a number that is based on data in calibrated years. The ICE-3G model is not rewritten to calibrated years because in this study the ICE-3G model will be used to compare TPW results from new ice models with older TPW results which were calculated using ICE-3G in uncalibrated years.

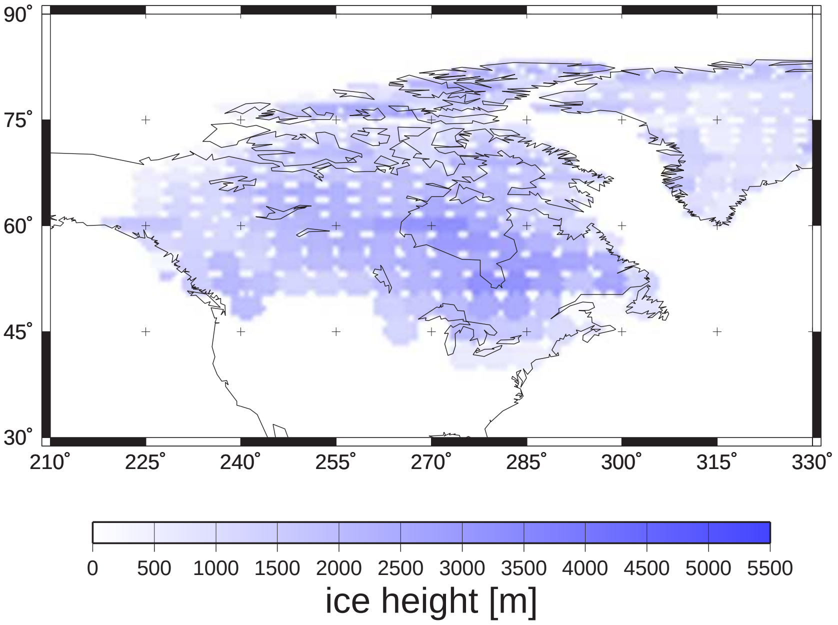

Figure 6.3 Global distribution of the ice melted during the last deglaciation period assumed by the ICE-3G ice model. Zoomed in on the Laurentide ice sheet

6.2.2 ICE-5G ice model

The successor of ICE-3G is the ICE-4G model which is produced by W.R. Peltier of the Department of Physics in the University of Toronto, Canada and published in [*Peltier*, 1994, 1996]. Although this model will not be used in the simulations the model will shortly be discussed here to give a better overview of the evolution of the ICE models developed by Peltier. The method to construct this ice model has not changed much with respect to ICE-3G, but some improvements have been made by using calibrated carbon years instead of uncalibrated carbon years. This means that 3 kyrs are added to the radiocarbon age of 18 kyr bp to get a calendar date of 21 kyr BP for the Last Glacial Maximum (LGM). The calibration is done using the long record of postglacial relative sea level change at Barbados, based on the Uranium/Thorium dating of the coral which allows for an extremely accurate time calibration [*Peltier*, 1995]. Secondly, it is based upon a more accurate spherically symmetric internal viscosity structure of the solid Earth, also known as VM2 (section 6.1.2). The circular discs are no longer used, instead a pointlike ice distribution is implemented. Finally the model is constrained by new and improved observational constraints including data on RSL, coral reefs and $\delta^{18}O$. This results in an increase in land-based ice at certain regions and gives an equivalent sea level rise of 120 m. Just like in ICE-3G the system of Earth, ice and ocean was in a state of isostatic equilibrium at LGM and no time-dependent shorelines were assumed.

ICE-5G is a more recent global ice sheet reconstruction published by *Peltier* [2004]. ICE-5G is considered to be one of the most accurate ice models available at the moment, which is the result of the use of a more complex combination of thermo-mechanical models of ice-sheet evolution and climate models. The refinement with respect to ICE-4G is accomplished by using better models of the individual regions, investigated by different authors, geomorphological analysis, and taking $\dot{g}$ and VLBI observations into account. As a result of these observations extra ice is added to the Hudson Bay region and the eustatic sea level has increased to 125 m instead of 120 m for ICE-4G. In this model time dependent shorelines are used, which has some interesting effects like the fact that the North Sea was assumed to be dry during the LGM, which allowed for ice sheet development in the North Sea basin. ICE-5G is just as ICE-4G based on the VM2 Earth model.

Ice model characteristics

The ICE-5G data record contains a larger amount of information which includes both the deglaciation and glaciation phase from 122 kyr BP till 0.5 kyr after present (AP) (see

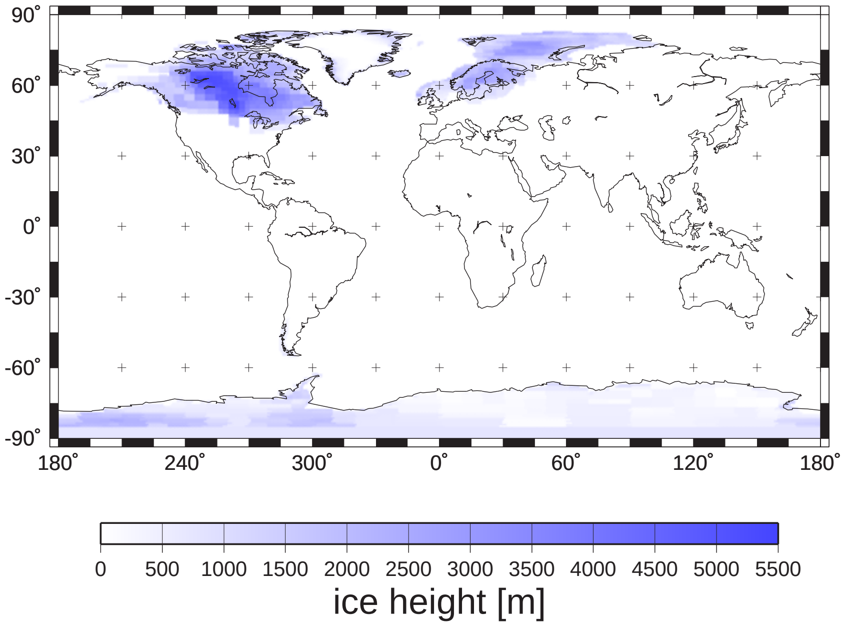

Figure 6.4 Global distribution of the ice melted during the last deglaciation period assumed by the ICE-5G ice model.

figure 6.6). The deglaciation period extends from 122 kyr BP till 30 kyr BP and contains data every 2 kyr. From 30 kyr BP till 18 kyr BP the interval between each data point will be 1 kyr and from 17 kyr BP till 0.5 kyr AP an interval of 0.5 kyr is used. Two extra data points are found at 0.1 kyr BP and 0.1 kyr AP. ICE-5G has a total ice mass which melts from LGM till the end of deglaciation of $4.57 \cdot 10^{19}$ kg which gives an equivalent sea level rise of about 126 m in this study. Originally the ICE-5G ice height data is given in a grid of 256x513 but is transformed to a 256x512 grid by excluding the double point at 0 degrees longitude to avoid the double use of this point. The transformation to the standard 257x512 grid is achieved by transforming the data on the 256x512 grid to spherical harmonic coefficients, truncated at 256 degrees, which are transformed back again to a 257x512 grid.

6.2.3 RSES ice model

The RSES model is developed by K. Lambeck of the Research School of Earth Sciences (RSES) of the Australian National University. The Laurentide ice sheet (over North America) and Greenland follow the model of ICE-1 [*Peltier and Andrews*, 1976a] and the rest of the ice sheets are based on earlier research and published articles by Lambeck and colleagues. The ice sheets of Fennoscandia, Barentsz Sea and British Isles are of a high spatial and temporal resolution and are consistent with the majority of the field evidence for ice-margin retreat and rebound data. The Antarctic and Laurentide ice sheet are on the other hand of coarse resolution and less suitable for high-resolution rebound modeling [*Kaufmann and Lambeck*, 2002]. This ice model is constrained using geomorphological data, sea level curves and assumptions on the local viscosity structure of the Earth. During the construction of each individual ice sheet not a global but a local viscosity structure was assumed. For the construction of the ice sheets of Fennoscandia an extensive database is used as explained in the introduction of this section. In a later study *Kaufmann and Lambeck* [2002] derived a global viscosity structure from the RSES ice model (see section 6.1).

Ice model characteristics

This ice model provides ice height data from 30 kyr BP till 2 kyr BP with a time step of 1 kyr and includes a deglaciation phase till LGM at 21 kyr BP and has a period of relative constant ice mass from 22 kyr till 30 kyr (see figure 6.6). RSES has a total ice mass which

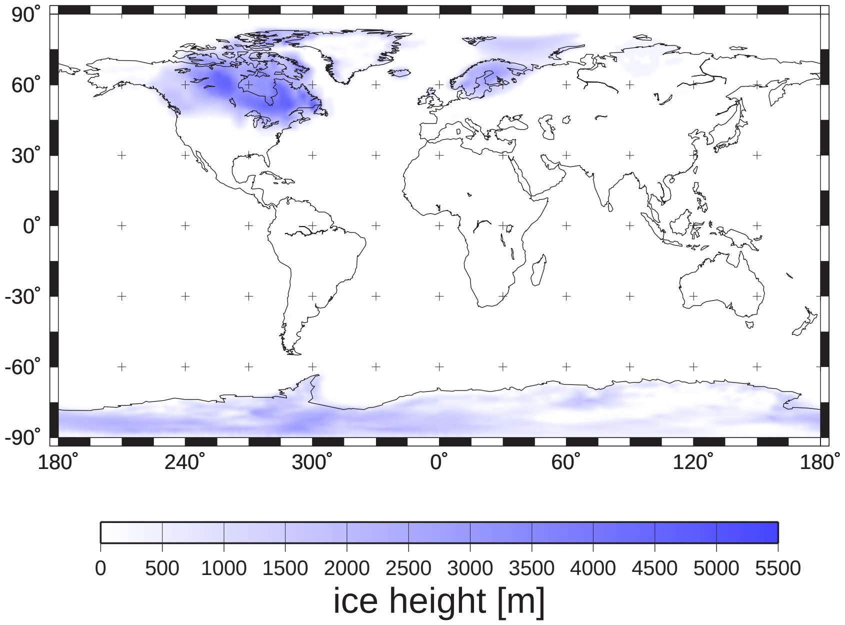

Figure 6.5 Global distribution of the ice melted during the last deglaciation period assumed by the RSES ice model.

melts from LGM till the end of deglaciation of $4.73 \cdot 10^{19}$ kg which gives an equivalent sea level rise of about 130 m in this study.

6.2.4 Ice model implementation

To investigate the present-day TPW and its behaviour correctly, also the glaciation phase and even multiple ice cycles have to be considered because of the relatively long relaxation time of the Earth to the ice load. In this study the late Pleistocene Ice Ages (about 800 kyr till 5 kyr BP) will be reconstructed and used to determine the effect on TPW. The structure of the ice age history will be based on known records of the ice cycles, but simplified to allow for faster computations and to make it easier to implement in the code. From oxygen isotope analysis of ocean sediments ($\delta^{18}O$) a main ice-age rhythm, with a 100 kyr cyclicity, can be identified [*e.g.*, *Shackleton and Opdyke*, 1976; *Shackleton*, 2000]. Further analysis indicates an average glaciation period of 90 kyr followed by a 10 kyr deglaciation period. In this study 8 ice-cycles of 100 kyr will be considered to model the late Pleistocene Ice Ages. For the ice-cycles a simplified saw-tooth loading is assumed as suggested by *Vermeersen et al.* [1997]. The glaciation period of the last ice-cycle will have time steps of 2 kyr to include all the data available in ICE-5G and to exclude any difference in results as resulting from use of different time steps. The last deglaciation period will have time steps of 0.5 kyr and the ice-cycles before the last ice-cycle will have time steps of 10 kyr. The increase in time steps is possible because the inaccuracy introduced by this simplified loading has only limited effect on present-day TPW as a result of the relatively fast relaxation of the loads.

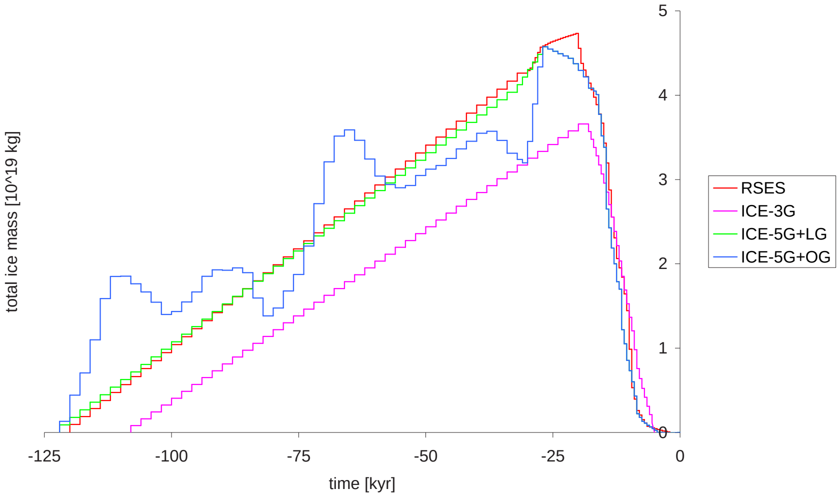

Figure 6.6 Comparison of the total mass distribution of different ice models in time. LG=linear glaciation, OG=original glaciation.

6.2.5 Ice model overview

The three ice-load histories as discussed above will have a large influence on the behaviour of TPW because they all represent a different mass distribution on the Earth, which consequently influences the moments of inertia and the behaviour TPW. The ice-load histories differ with respect to each other in both spatial and temporal distribution of ice. In figure 6.7 and 6.8 and table 6.3 the ice distribution of melted ice since LGM is given for different areas.

Ice sheet	ICE-3G mass [10^{18} kg]	ICE-5G mass [10^{18} kg]	RSES mass [10^{18} kg]
Antarctica	9.13	6.62	10.00
Fennoscandia, Barentsz Sea and British Isles	4.35	7.53	5.45
Kara Sea and East-Siberia	3.10	0.66	0.44
North America	17.10	29.22	29.17
Greenland and Iceland	2.91	1.75	2.25
All	36.59	45.79	47.33

Table 6.3 Ice distribution of the considered ice models over different areas.

6.3 Topography

The used topography is derived from ETOPO2 which is a global elevation database with a resolution of two minutes (about 4 km at the equator) in latitude and longitude. This database, put together from several different institutes, contains information from sources like satellite radar altimetry and shipboard echo-sounding measurements (http://www.ngdc.noaa.gov/mgg/fliers/01mgg04.html). From this elevation database an ocean function is constructed by assigning a value of 1 when the elevation is greater than 0 m and 0 when it is lower than 0 m (see figure 6.9). A consequence of this assumption is that land which lies below zero meters is noted as ocean, so a large part of Holland is virtually covered with water, but this is not of a great importance on a global scale.

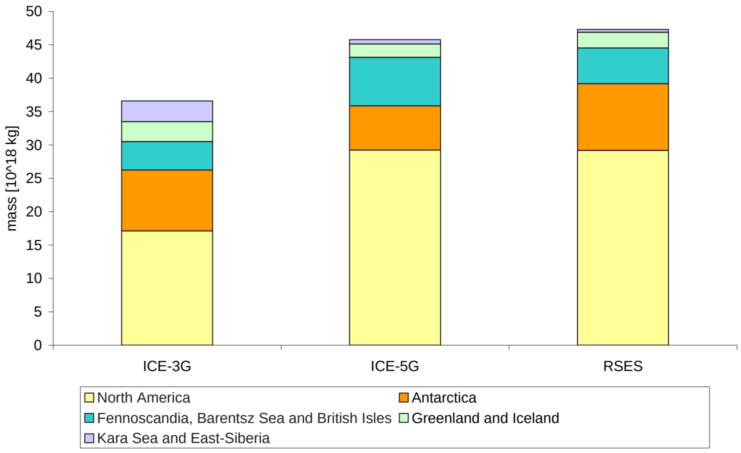

Figure 6.7 Absolute Ice distribution of the considered ice models over different areas at LGM.

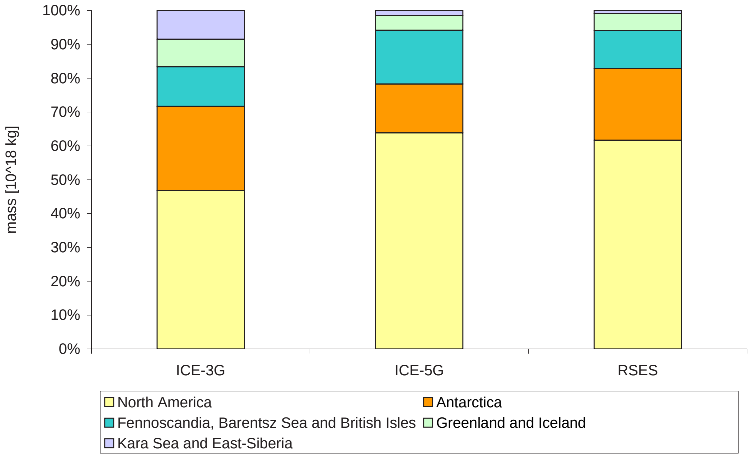

Figure 6.8 Relative ice distribution of the considered with respect to each ice models over different areas at LGM.

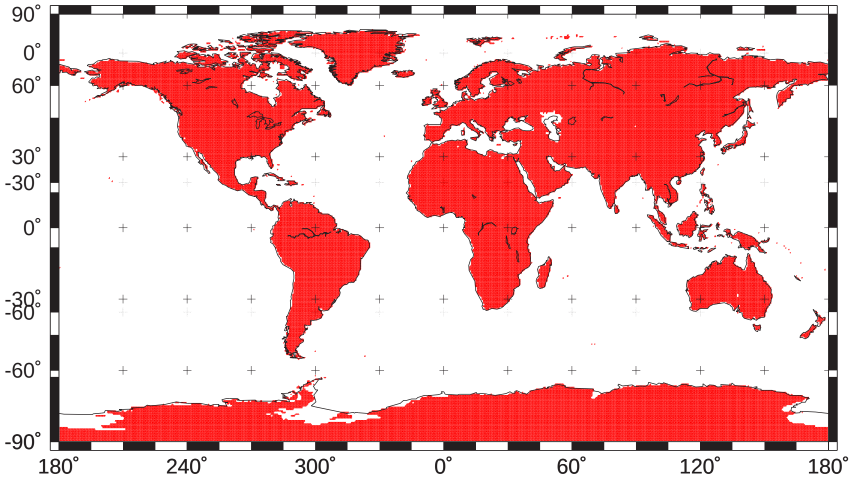

Figure 6.9 Topography (based on ETOPO2) from which the ocean function can be derived. Red: elevation greater than 0 m.

Chapter 7

Results

During the last decades true polar wander (TPW) has been frequently used to constrain the radial mantle viscosity profile of the Earth [*e.g.*, *Vermeersen et al.*, 1998; *Kaufmann and Lambeck*, 2002]. Recent improvements in the field of ice models (ICE-5G and RSES) and the use of the hotspot reference frame make it interesting to investigate the impact on results and conclusions of older research.
In this chapter first the sea level results, including the effects of rotation, are discussed in section 7.2 for three different ice models with corresponding Earth models. In section 7.3 TPW and the influence of ice and Earth models is discussed. Finally the discussion of the impact of the improvements on older research can be found in section 7.4.

7.1 Implementation of TPW in the sea level equation

The implementation of the sea level theory is not always straightforward and in this section some practical issues will be addressed. The program structure and the implementation of the rotation into the sea level equation is described in section 7.1.1. In section 7.1.2 the implementation process in treated and in section 7.1.3 the optimization of the grid is discussed.

7.1.1 Program structure

The theory described in the previous chapters is now implemented into a Fortran code to investigate the effect glacial isostatic adjustment (GIA) has on TPW. The viscoelastic Love numbers, which describe the response of a specified Earth model as discussed in chapter 3, are determined with the Fortran code developed by Dr. L.L.A. Vermeersen of Delft University of Technology. These codes have been frequently used and have been verified with other codes [*e.g.*, *Vermeersen et al.*, 1997]. The pseudo-spectral sea level equation from chapter 4 is solved by a sea level code provided by G. Di Donato of the University of Milan and has been modified and optimized by Ir. W. van der Wal and Ir. H.H.A. Schotman. In this study the traditional rotation theory is added in a self-consistent way as described in chapter 5. In figure 5.2 as detailed description of the implementation of rotation in the sea level equation is given.
In the beginning of the program, before the iterations are started, the rotational parameters and rotational roots are calculated. This is done in a subroutine which reads the viscoelastic Love numbers and calls other subroutines that contain the rootfinding methods (as described in section 5.3). To determine the rotational potential a subroutine is created which computes the perturbations of inertia by using the sea-load and the known ice-load. In first instance the sea-load will be estimated from a eustatic sea level change as result of a certain ice melt or grow. From the perturbations of inertia, rotational roots and parameters the direction of polar wander is determined and subsequently the rotational

potential. The rotational potential is used to calculate the new sea level, which will be used as new input for the iteration. The iteration will continue until the predefined level of convergence is reached.

7.1.2 Implementation process

The new subroutines were tested separately as much as possible. The rotational roots and parameters were tested qualitatively with the help of earlier research [*e.g.*, *Mitrovica and Milne*, 1998; *Martinec and Hagedoorn*, 2005]. The qualitative behaviour of the direction of polar wander was tested using [*Milne and Mitrovica*, 1998] and [*Sabadini and Vermeersen*, 2004]. When the code was completed a start was made to benchmark the complete sea level code which can be found in appendix A. but due to lack of time by the other party the benchmark was ended after the verification of the rotational roots, parameters and the perturbation of inertia.
Some problems which arose during the implementation were with respect to choosing the right normalization (equation 4.21 till 4.24) and using the correct analytic expression for the time convolution (equation 5.43).

7.1.3 Grid optimization

The sea level equation for a rotating Earth is solved with an iterative procedure in the spectral domain as explained in chapter 5. For this study the spherical harmonic expansion is truncated at degree 256, which allows for results with satisfactory accuracy. Higher truncation levels are possible but impractical because there is only limited CPU power available to do the simulations in a reasonable time. A simulation of the sea level on a rotating Earth during the late Pleistocene (including 180 sea level calculations) takes approximately 8 hours to finish on a R12000[1] workstation when a truncation level of 256 is used. To do the spherical harmonics computation with a high accuracy the number of nodes on which the ice-load and ocean function is given should be optimized. The optimization is dependent on the method selected to calculate the spherical harmonics coefficients, which will be explained below. To obtain the spherical harmonics coefficients, first a Fourier transformation is applied along the parallels of the grid followed by the computation of spherical harmonics coefficients from the obtained Fourier coefficients. The most efficient method to obtain the spherical harmonics coefficients is the so-called Gauss-Legendre quadrature [*Sneeuw*, 1994]. The Gauss-Legendre quadrature requires the nodes to be given on a Gauss-grid, which is still quite close to an equi-angular grid. In this Gauss-grid the latitude circles are chosen to coincide with the zeros of the Legendre polynomial of degree $\ell+1$. The Gauss-Legendre quadrature requires less nodes ($2\ell \times (\ell+1)$) than other methods, like the Gauss method of least squares ($2\ell \times (2\ell+1)$), to compute the spherical harmonics coefficient up to degree ℓ. So when a truncation level of 256 is applied, subsequently a grid of 257x512 nodes is used to optimize the spherical harmonics computation.

7.2 Sea level results

The implementation of rotation in the sea level equation has a relatively small but non-negligible effect on the sea level. These effects are first discussed on a global scale followed by a discussion on local scale in comparison with observations from different sites.

7.2.1 Relative sea level results on global scale

The global predictions of the present-day speed of relative sea level (RSL) without rotation for the ICE-3G(VM1), ICE-5G(VM2) and RSES(KL) models is given in figure 7.1.

---

[1] A Silicon graphics workstation with a 270 Mhz processor and 2048 MB of RAM

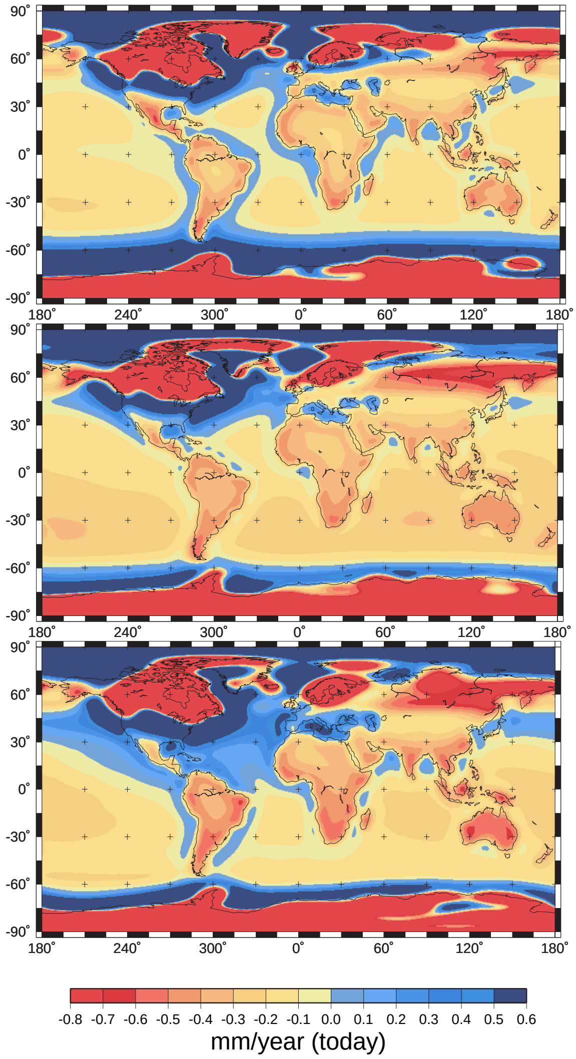

Figure 7.1 Global predictions of the present-day speed of RSL without rotation for respectively (from top till bottom) the ICE-3G(VM1), ICE-5G(VM2) and RSES(KL) model.

In this case eight ice cycles are simulated on a spherically symmetric, incompressible, Maxwell-viscoelastic Earth model as explained in the previous chapter. The predictions show a large RSL fall in the former glaciated areas and a large sea level rise in the area surrounding it. In the far field the RSL change is positive and relatively small. The details of the GIA phenomena are treated in more detail in section 2.2.

The ICE-3G(VM1) model shows a straightforward RSL signal with continental leveraging near continents. The ICE-5G(VM2) model has, with respect to the ICE-3G(VM1), about the same near field GIA effect even though the total ice mass present at last glacial maximum (LGM) is much higher. This is partly the result of a relatively low upper mantle viscosity of $6 \cdot 10^{20}$ Pas, which leads to a faster relaxation of the Earth. Although it must be noted that the present-day speed RSL is the result of a complex interaction between the Earth and the loads and there are many causes to a certain result. The continental leveraging effect is negligible because of the low upper mantle viscosity, which has a large influence on small scale effects, and causes a faster relaxation of the Earth to the load. The RSES(KL) model has a more dominant near field GIA effect, than the other models. This is among others caused by the high lower mantle viscosity of $2 \cdot 10^{22}$ Pas, which causes the large scale GIA effect to relax slowly. The rotation induced component of RSL is mostly dominated by the degree 2, order 1 harmonic coefficient, which accounts for 99 percent of the signal as can be seen in figure 7.2. This dominance can be traced back to

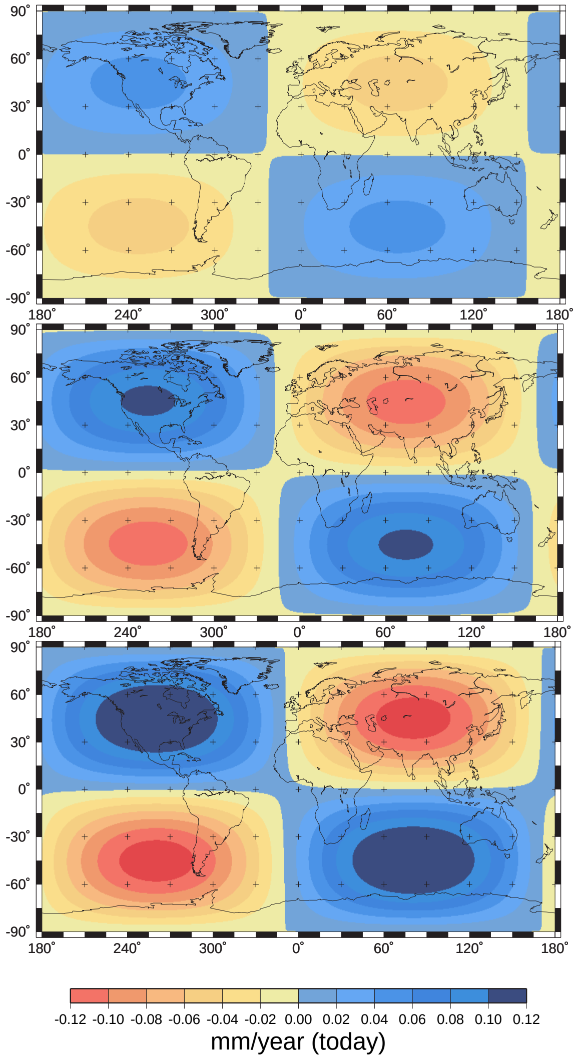

Figure 7.2 Global predictions of the present-day speed of RSL solely due to variations in the Earth's rotation of respectively (from top till bottom) the ICE-3G(VM1), ICE-5G(VM2) and RSES(KL) model. Note that the scale is different from figure 7.3 and 7.1.

equation 5.49, which is dependant in first order on the direction of TPW (m_1 and m_2). The positioning of the degree 2, order 1 signal on the Earth is determined by the direction of the TPW. The rotational potential will show a maximum change along the meridian, which points in the direction of TPW at mid-latitudes. In case of ICE-3G(VM1) this will be about 70 °W and 76 °W for ICE-5G(VM2) and RSES(KL). A minimum change is shown at both 90 longitudinal degrees from this meridian and along the equator. The RSL changes shown in figure 7.2 reflect this pattern. The magnitude of the 2,1 signal is dependant on the TPW speed and thus the amount of mass distribution and response of the Earth. Note that the net effect of the rotational induced RSL change is zero because the total mass is conserved. The more mass that is displaced and the higher the viscosity of the lower Earth layers is, the greater the magnitude of the rotational effect is.

When observing the figures it can be concluded that ICE-3G(VM1) has the weakest rotational signal and RSES(KL) the strongest. This is the result of the fact that the RSL change is determined as the geoid rate of change minus the radial displacement of the Earth (equation 4.2).

A larger ice mass present at LGM in the ICE-5G(VM2) model with respect to ICE-3G(VM1) model, gives a larger geoid height change at present day. Because a roughly similar viscosity stratification gives an equal radial displacement, the rotation induced RSL change will increase.

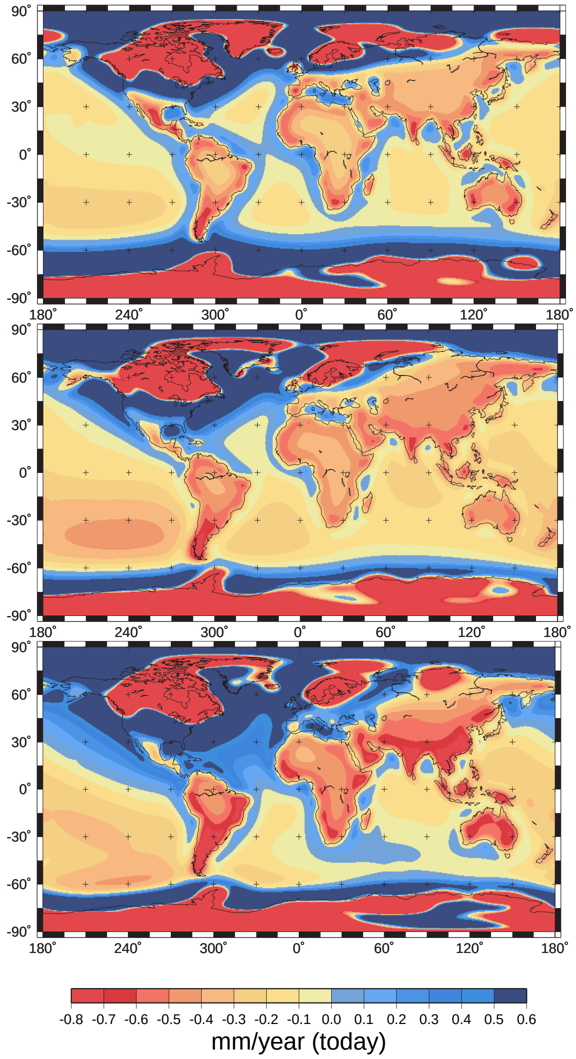

Figure 7.3 Global predictions of the present-day speed of RSL with rotation of respectively (from top till bottom) the ICE-3G(VM1), ICE-5G(VM2) and RSES(KL) model.

The RSES(KL) model with respect to the ICE-5G(VM2) model has a slightly higher rotational induced RSL change. This is the result of the higher lower mantle viscosity, which leads to a lower radial displacement of the Earth and a similar ice mass at LGM which gives an about equal geoid height change. Finally in figure 7.3 the rotational effects are taken into account in the GIA induced RSL. In the far field and near the maximum of the 2,1 signal the effects of rotation can be as large as effects like ocean syphoning or continental levering. The rotational induced RSL change has only a small contribution to the whole signal but at far-field areas it can have a significant effect which can not be neglected. This is especially the case at periods between ice ages (at present) when the GIA effect on the relative sea level is small.

7.2.2 Relative sea level results on local scale

In this chapter the RSL with and without rotation is discussed at different sites and compared with observations. The RSL curves describes the RSL from the LGM till present. In case of the ICE-3G(VM1) model the LGM is located at 18 kyr before present (bp) in the ^{14}C timescale. In case of ICE-5G(VM2) and the RSES(KL) model the LGM is located at 21 kyr before present (BP), in calibrated (calendar) years.
Three different locations are chosen such to demonstrate the spatial distribution of the

minimum and maximum amplitudes of the rotation induced RSL signal near and further away from uplifting areas (see figures 7.1 and 7.2). The location should also have an acceptable amount of sea level observations available. The chosen sites are Brigantine (United States), Bahia Blanca (Argentina) and Merseyside (England).

Firstly the sea level at Brigantine (United States) is considered in figure 7.4. Brigantine is chosen because it is located near the former Laurentide ice sheet and close to a maximum positive value of the rotational signal. The melting of the ice after LGM gives a decrease in polar wander, because mass is moved away from the poles in the direction of the equator. This decrease in polar wander has a direct effect on the rotational potential and thus the RSL. When the ice melt stops the relaxation of the Earth continues and mass is redistributed over the Earth which gives a rise in RSL. The rotation induced RSL can have a significant maximum difference of 13 m during the deglaciation period as can be observed with the RSES(KL) model. The observations fit quite good with the predictions of RSL of ICE-5G(VM2) and RSES(KL), although the observations are only available of the last 8 kyr. Note that the rotational induced RSL signal is relatively small at LGM with respect to the GIA induced RSL signal, but is of larger importance near the present as the GIA induced RSL signal approaches zero.

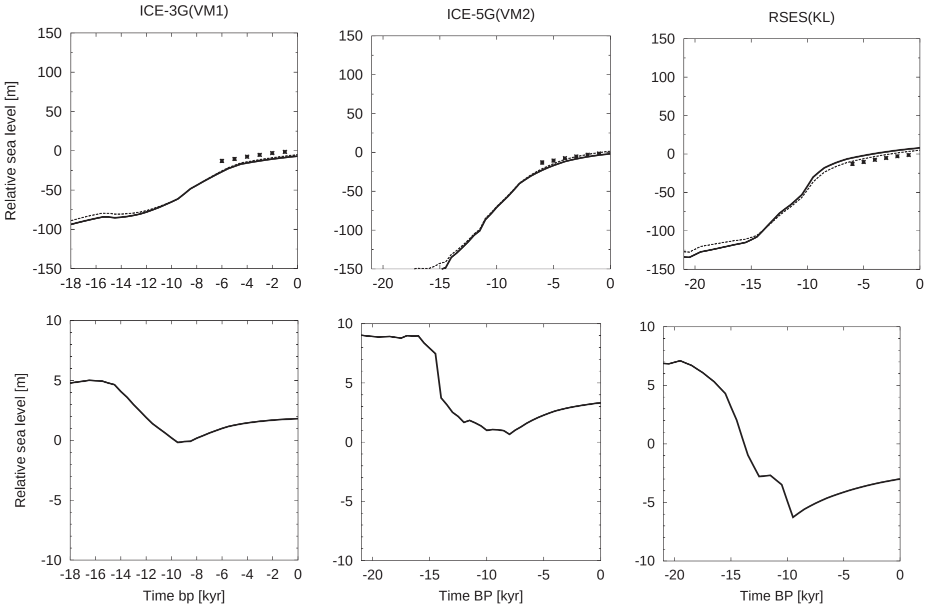

Figure 7.4 Sea level curve of Brigantine (United States) at 39.5 degrees latitude and 285.5 degrees longitude. Different ice models are used: Left: ICE-3G(VM1) in ^{14}C time, middle: ICE-5G(VM2) in calibrated time, right: RSES(KL) in calibrated time. The upper figures hold the sea level with and without rotational effects where the solid line is the sea level without rotational effects, the dashed is the sea level with rotational effects and the observations are indicated by crosses with error bars. The lower figures hold the rotation induced component the sea level.

Secondly Bahia Blanca (Argentina) is chosen because it is located further away from former GIA and close to a maximum negative of the globally distributed rotational signal. At Bahia Blanca the rotational induced RSL shows the opposite behaviour as in Brigantine and is the result of the same causes. The observations fit quite good with the predictions of RSL of ICE-5G(VM2) and RSES(KL). Thirdly Merseyside (England) is located near the former glaciated area of British Isles and near a minimum of the globally distributed rotational signal. In this case it is clear that the rotation induced RSL is negligible over the whole deglaciation period. The observations fit quite good with the predictions of RSL of ICE-3G(VM2) and ICE-5G(VM2), but less well with RSES(KL).
It can be concluded, as in the previous section, that the effect of rotation on RSL is non-negligible and its contribution depends on the location on the Earth.

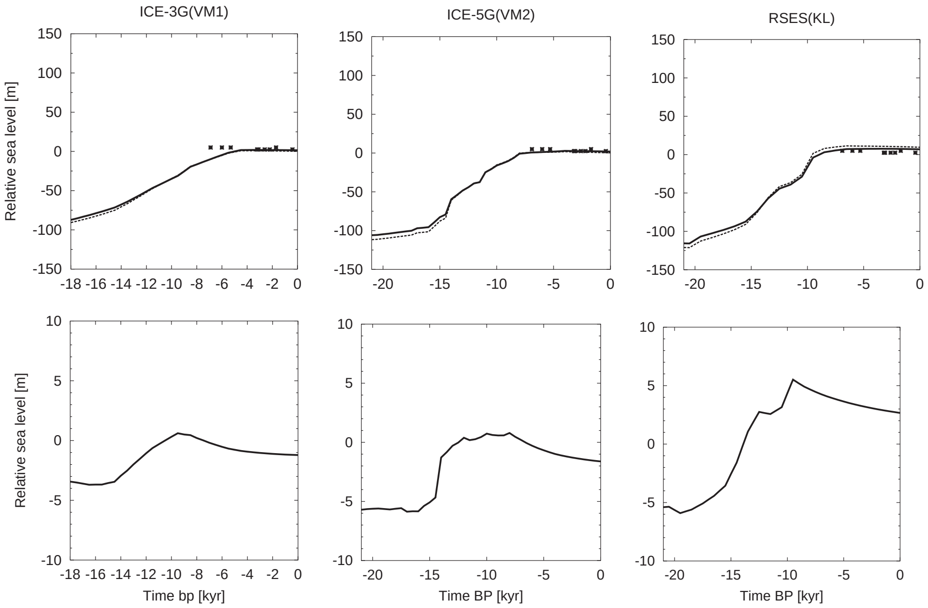

Figure 7.5 Sea level curve of east Bahia Blanca (Argentina) at -39.6 degrees latitude and 297.9 degrees longitude. The same description applies here as in figure 7.4.

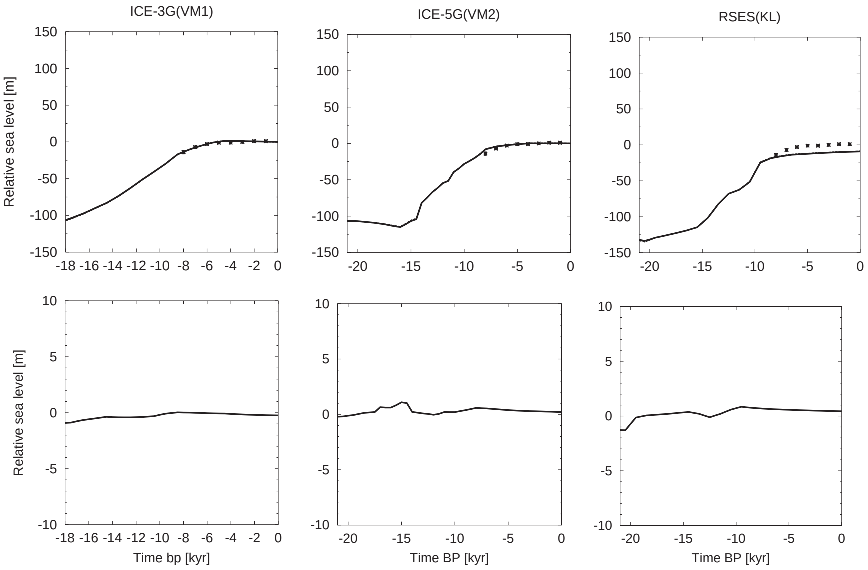

Figure 7.6 Sea level curve of Merseyside (England) at 53.5 degrees latitude and 356.8 degrees longitude. The same description applies here as in figure 7.4.

7.3 TPW and the influence of ice and Earth models

First the assumption of linear glaciation is discussed in section 7.3.1 followed by a discussion of the results of different TPW simulations using ice models and original Earth models in section 7.3.2. Finally in section 7.3.3 the relation between TPW and the lower mantle viscosity is discussed.

7.3.1 TPW simulation with linear glaciation

The results presented in this section are based on model predictions on a spherically symmetric, incompressible, Maxwell-viscoelastic Earth model. In earlier studies glacial cycles were mostly assumed to be structured as a saw-tooth with linear glaciation period and a more detailed deglaciation period. In this section the assumption of a linear glaciation history on present-day TPW-speed and path is investigated using the ICE-5G(VM2) model, because it describes both a glaciation and deglaciation period. One model will have a linear glaciation history and the other the original glaciation history. Both models will have the same time steps as in the original ice-load history as discussed in section 6.2.2. The results are presented in figure 7.7 and table 7.1.

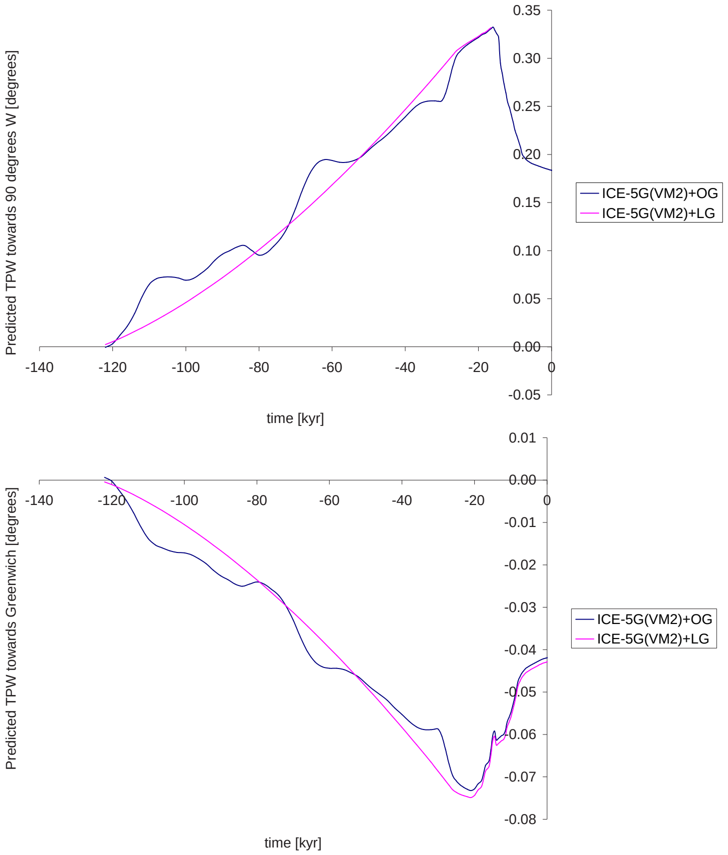

Figure 7.7 Predicted TPW with a linear and original glaciation history during the last ice-cycle. First figure: TPW in the direction of $90°$W, second figure: TPW in the direction of Greenwich.

From figure 7.7 it can be concluded that the assumption of a linear glaciation history is a very reasonable assumption, even though the original glaciation history differs significantly as can be seen in the comparison of total mass distribution of different ice models (figure 6.6). The results show that present-day TPW-speed and path differ about 1 percent, which is mainly caused by a small discrepancy in TPW towards Greenwich.

model	glaciation	speed $[^\circ Myr^{-1}]$	path [longitude °W]
ICE-5G(VM2)	original	1.06	77.5
ICE-5G(VM2)	linear	1.08	77.1

Table 7.1 Predicted present-day TPW-speed and path with a linear and original glaciation history during the last ice-cycle. The predicted present-day TPW-speed is the average TPW-speed of the last 1000 year.

This is probably caused by the melting of the ice of the Greenland ice sheet shortly before last glacial maximum (LGM). Due to the melting of the ice during the original glaciation the shift of the rotation axis will be, with respect to the TPW as result of linear glaciation, smaller because the melting of Greenland will counteract the motion caused by the growing of the dominant Laurentide ice sheet. The ice sheet on Greenland is positioned between the two axes along which the rotation is defined (see figure 5.1), but this effect is mostly visible in the TPW towards Greenwich. This is because the melting of the Greenland ice sheet is of relatively large importance for the determination of the TPW towards Greenwich and of minor importance in the determination of TPW towards 90°W, as a result of the dominant presence of the Laurentide ice sheet.
Of minor importance is the difference in the ice mass growth and the geographical location of the ice close before LGM. There is a gradual increase in ice mass in case of linear glaciation and the sudden large increase in ice mass at 35 kyr BP. As can be seen in figure 7.7 this effect is not completely relaxed at present-day. But the impact which the application of the original glaciation will have on older research is not significant.

7.3.2 TPW simulation with different ice models and corresponding Earth model

In this section the present-day TPW of three different ice-load histories with their corresponding Earth stratification are compared. The verification of results using the ICE-3G(VM1) model will be done, followed by the verification of results using observations and finally the ice models with corresponding Earth model are compared with each other.

The ICE-3G deglaciation history has been used for mantle inversions and GIA research frequently, but lately this model has been exceeded by the ice models RSES and ICE-5G (see section 6.2). The TPW will be simulated with the ICE-3G, ICE-5G and RSES ice models and corresponding Earth models. Because an ice model is usually created with a specific Earth model, this Earth model is implicitly present in the ice model. So to obtain correct TPW results the corresponding Earth model has to be used. In case of ICE-3G and ICE-5G the corresponding Earth models (VM1 and VM2 respectively) will be applied that were used to create the ice models. For RSES a single corresponding Earth model did not exist because regional Earth models were used to create the ice model, instead the Kaufmann-Lambeck (KL) Earth model will be applied. The stratification of the applied Earth models are explained in more detail in the previous chapter. The results of the TPW simulations of the ice models with original Earth model are presented in figure 7.8 and table 7.2.

model	glaciation	speed $[^\circ Myr^{-1}]$	path [longitude °W]
ICE-3G(VM1)	linear	1.33	70.1
ICE-5G(VM2)	original	1.83	76.1
RSES(KL)	linear	1.21	76.0

Table 7.2 Predicted present-day TPW-speed and path using an ice-load history with corresponding Earth model.

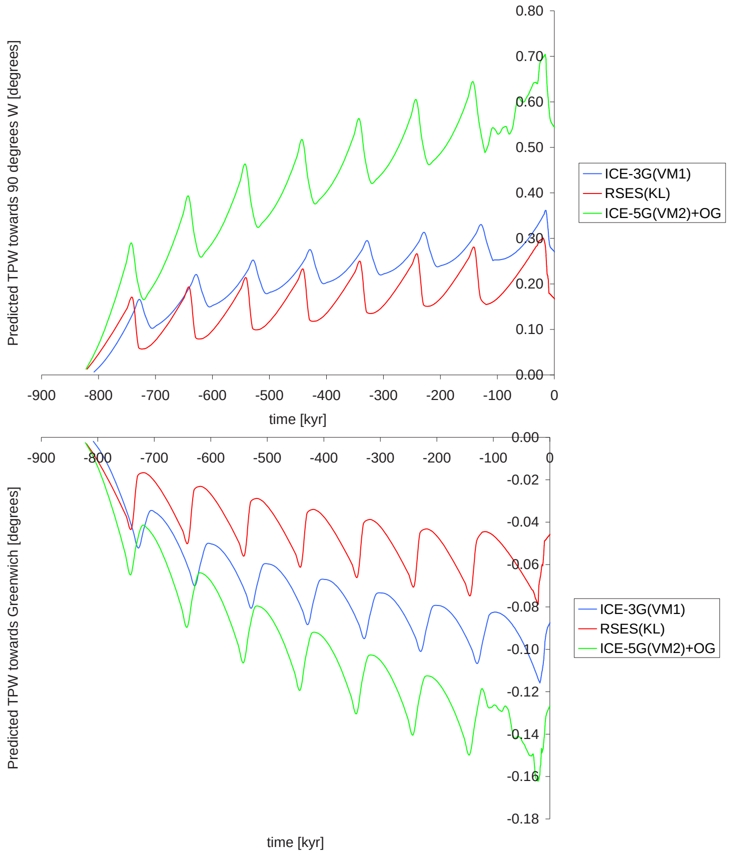

Figure 7.8 Predicted TPW-speed using an ice-load history with corresponding Earth model. First figure: TPW in the direction of 90°E, second figure: TPW in the direction of Greenwich.

Verification of results using ICE-3G(VM1)

The correctness of the TPW results can be verified, till some degree, by comparing the ICE-3G(VM1) model with two earlier obtained results from *Vermeersen et al.* [1997] and *Mitrovica et al.* [2001].

- The first study is done by *Vermeersen et al.* [1997] and investigates the rotational response of the Earth to Pleistocene deglaciation. For this study a volume-averaged 5-layer Earth model is used together with a saw-tooth ice-load history as input. It must be noted that in this paper the ice and water distribution is assumed to be redistributed eustatically over the oceans. There will be a noticeable difference with respect to the moments of inertia and TPW, which are based on a graviationally self-consistent redistribution. This result differs about 9 percent with the predicted present-day TPW-speed obtained in this study, which is most likely the result of the assumption of eustatic redistribution of water. The small differences in the radial density and rigidity stratification and the difference in time steps are negligible.
- The second study is carried out by *Mitrovica et al.* [2001] and investigates the rotational response of the Earth to Pleistocene deglaciation but now self-gravitating compressible Earth models are used. The secular TPW speed is about 60 percent lower than the results obtained in this study. *Mitrovica et al.* [2001] simulated the TPW with a similar mantle viscosity stratification but with a thinner elastic lithosphere of 95 km. The difference is possibly the result of the use of an incompressible Earth model in this study instead of a compressible Earth model. At low viscosities of the lower mantle the effect of compressibility on present-day TPW-speed is relatively large in comparison with higher viscosities [*e.g.*, *Mitrovica and Milne*, 1998; *Vermeersen et al.*, 1996b]. This effect is about 25 till 30 percent for a viscosity of $2 \cdot 10^{21} Pas$ for the

lower mantle [*Mitrovica and Milne*, 1998]. Another cause of the difference could be the use of a thicker elastic lithosphere (120 km) together with a relatively low lower mantle viscosity which will overestimate the results of an elastic lithosphere thickness of 95 km with about 15 till 20 percent [*Mitrovica et al.*, 2005]. A final cause of the difference could be the difference in the radial rigidity and density stratification used by [*Mitrovica and Milne*, 1998] which is not given in detail but is assumed to be based on PREM like the other Earth models used. The differences in the radial viscosity stratification are most likely the explanation for the discrepancies in TPW results.

Verification of results using observations

In this section the predicted present-day TPW-speed and path resulting from an ice model with corresponding Earth model (table 7.2) are compared with the observed TPW-speed ($1.12\,^{\circ}Myr^{-1}$) and path ($68.4\,^{\circ}$W) in the hotspot reference frame using the Hipparcos star catalog.

When these results are compared it appears, at a first glance, that the present-day TPW-speed of the RSES(KL) model comes closest with 8 percent difference and the present-day TPW path of the ICE-3G(VM1) model resembles the observations the best with 2 percent difference. Both rotational observables of the ICE-3G(VM1) model differ at maximum with 20 percent to the observations, the RSES(KL) model with 10 percent and ICE-5G(VM2) shows a discrepancy of more than 60 percent. The reason these models produce different results is because in this thesis the effect of compressibility is not taken into account, other forcings causing TPW are not taken into account and recent deglaciation events are neglected in the ice model. It must be noted that all the used Earth models were constructed using earlier TPW observational data, which also has an indirect effect on the present-day TPW-speed and path. These probable causes will be explained in more detail below.

- When the results are compared with observations, a compressible model is preferred over an incompressible model because it is a better approximation of the Earth. So when compressibility is taken into account, the present-day TPW-speed for the ICE-3G(VM1) and ICE-5G(VM2) model drop with 25 percent for models have an average lower mantle viscosity of $2 \cdot 10^{21} Pas$ as can be seen in figure 2 of [*Mitrovica and Milne*, 1998]. It is assumed that the behaviour of present-day TPW-speed as a result of changing lower mantle viscosity for the compressible and incompressible model is the same in this study. This changes the present-day TPW-speed of ICE-3G(VM1) into $1.00\,^{\circ}Myr^{-1}$ and ICE-5G(VM2) into $1.37\,^{\circ}Myr^{-1}$. In the RSES(KL) model compressibility has only a marginal effect on the present-day TPW-speed as a result of the relatively high lower mantle viscosity of $2 \cdot 10^{22} Pas$.
- The discrepancies could also be due to the neglect of other forcings than GIA in the TPW simulations like: tectonic processes associated with mountain building [*Vermeersen et al.*, 1994], subduction of oceanic lithosphere [*Ricard et al.*, 1992] and mantle convection. The influence of mantle convection on present-day TPW can be as large as $0.39\,^{\circ}Myr^{-1}$ towards $24\,^{\circ}$W [*Steinberger and O'Connell*, 1997]. This counteracts the larger predicted present-day TPW-path from the ICE-5G(VM2) and RSES(KL) model but decreases the part of the TPW-speed which is caused by GIA.
- Any recent deglaciation events which are not taken into account in the ice model can have a large influence on the predicted present-day TPW. A recent decrease in ice mass of Antarctica, Greenland and mountain glaciers might lead to a higher predicted present-day TPW-speed [*Gasperini et al.*, 1986].

Until now all the studies that use TPW observations assumed that the observed TPW is only caused by GIA. This assumption is made because TPW caused by other phenomena are out of the scope of this thesis. When, for example, mantle convection is also taken into account as one of the drivers of TPW then this will have a profound effect on the observed TPW as result of GIA. When the results of *Steinberger and O'Connell* [1997] are subtracted from the observed TPW, the present-day TPW-speed as result of GIA will drop and the present-day TPW-path will be pointing more in the direction of the meridian longitude 90°W. For older mantle inversion studies, which used the observed present-day TPW, this will result in a higher predicted lower mantle viscosity than was concluded in first instance.

Comparison between ice models with corresponding Earth model

Before the models can be compared properly with each other they will be separated into an Earth and ice model to get more insight in what part of the model is responsible for certain behaviour. To investigate to what extent the Earth models influence the present-day TPW, the present-day TPW will be simulated with a simplified Laurentide ice sheet in combination with different Earth models. A simplified Laurentide ice model is chosen, because it is a simple forcing which makes it relatively easier to interpret the results. The simple ice-load is a parabolic ice distribution on North America with a maximum height of 4000 m at LGM. The maximum height of the ice sheet is located at 90°W and 60°N with a radius of 15°. The ice-load history consists of 8 glacial cycles with 90 kyr of glaciation and 10 kyr of deglaciation with time steps of 10 kyr. The results are presented in figure 7.9 and table 7.3.

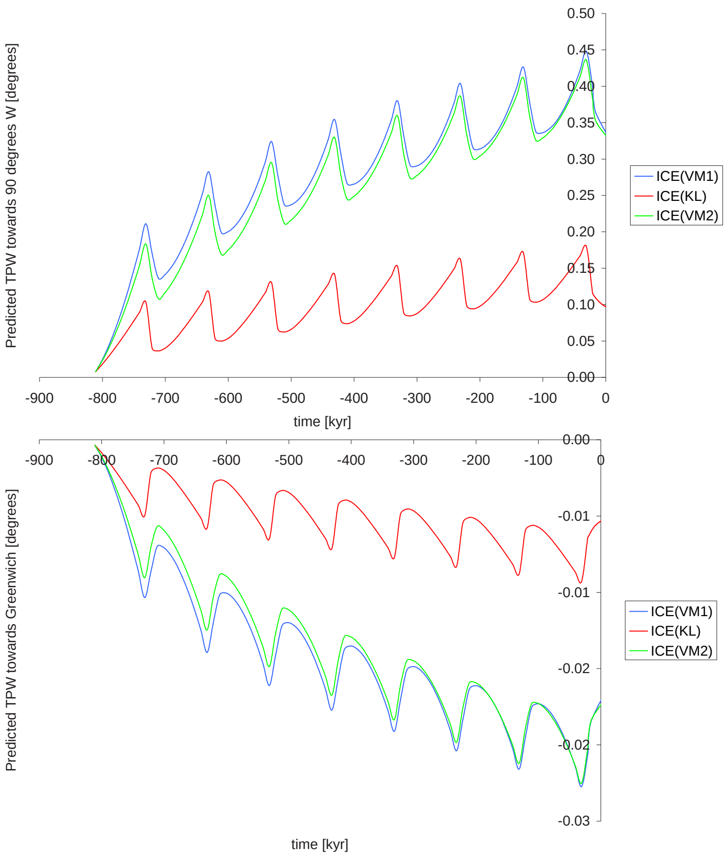

Figure 7.9 Predicted TPW with a simplified ice-load and three Earth models.

To investigate to what respect the ice models influence the present-day TPW, the present-day TPW will be simulated with the same Earth model (VM2) and different ice models. The results are presented in figure 7.10 and table 7.4.

From table 7.4 it can be seen that the ice models can differ significantly in both TPW-speed and path and from table 7.3 it can be concluded that the Earth model has a large influence on the TPW-speed but not on the TPW-path. These findings can be explained as

model	glaciation	speed [$^\circ Myr^{-1}$]	path [longitude °W]
ICE(VM1)	linear	1.51	87.1
ICE(VM2)	linear	1.03	87.0
ICE(KL)	linear	0.51	87.3

Table 7.3 Predicted present-day TPW-speed and path with a simplified ice-load and three Earth models. The predicted present-day TPW-speed is the average TPW-speed of the last 1000 year.

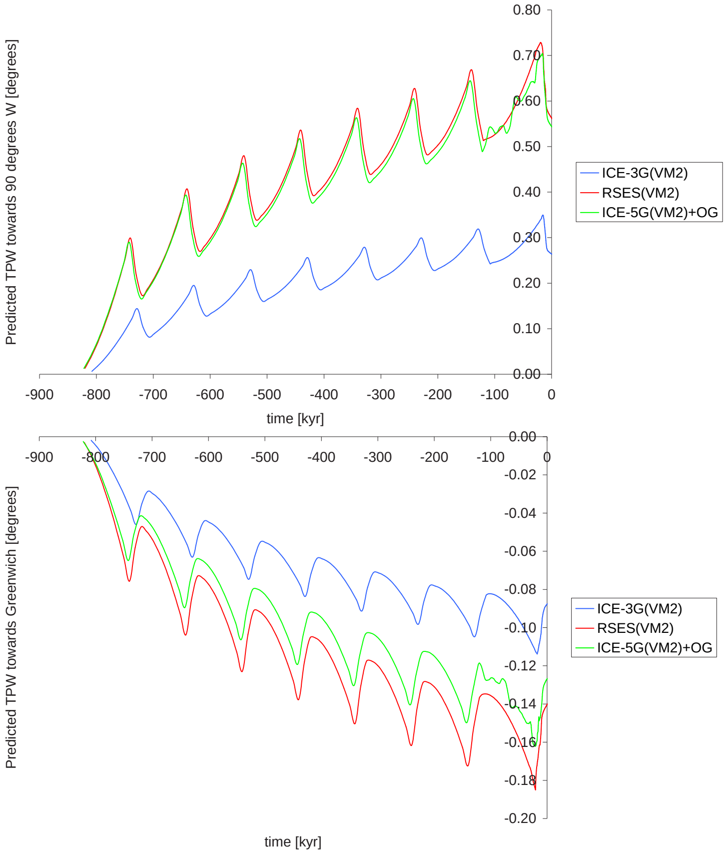

Figure 7.10 Predicted TPW using three ice-load histories and the VM2 Earth model. First figure: TPW in the direction of 90°E, second figure: TPW in the direction of Greenwich.

model	glaciation	speed [$^\circ Myr^{-1}$]	path [longitude °W]
ICE-3G(VM2)	linear	0.96	68.9
ICE-5G(VM2)	original	1.83	76.1
RSES(VM2)	linear	1.92	75.1

Table 7.4 Predicted present-day TPW-speed and path using three ice-load histories and the VM2 Earth model. The predicted present-day TPW-speed is the average TPW-speed of the last 1000 year.

the differences in TPW-speed, which are the result of the amount of ice distributed relative to the axis of rotation in combination with the reaction of the Earth to the changing loads.

ICE-5G(VM2) and ICE-3G(VM1)

When the results of the ICE-3G(VM1) and ICE-5G(VM2) models are investigated there are some distinct differences to be observed:

- There is a 38 percent discrepancy in present-day TPW-speed between the ICE-

5G(VM2) model and the ICE-3G(VM1) model. This discrepancy can be explained by the different ice distribution of both ice models and a different lower mantle viscosity of both Earth models.

  - A higher TPW-speed for ICE-5G(VM2) is the result of the 25 percent more ice at LGM on the Northern Hemisphere which is included in ICE-5G. Also the less equally distributed ice around to the North Pole has to be taken into account. In ICE-5G there is relatively more ice on Fennoscandia, Barentsz Sea and Laurentide ice sheet (see figure 6.8). This gives an even higher predicted TPW-speed towards both Greenwich and 90°W than the 25 percent increase in mass would suggest. The increase in mass for ICE-5G is of great influence on the present-day TPW, even though the present-day TPW-speed as result of ICE-5G(VM2) is also somewhat lower because less mass is melted at the end of deglaciation in comparison to ICE-3G (see figure 6.6).
  - The average lower mantle viscosity of VM2 is considerably higher than VM1, as can be seen in figure 6.1. A shift in the average lower mantle viscosity from $2 \cdot 10^{21} Pas$ for VM1 to $1.6 \cdot 10^{21} Pas$ for the upper lower mantle and $3 \cdot 10^{21} Pas$ for the lower lower mantle for VM2 can already result in a predicted present-day TPW-speed which will be about 15 till 20 percent lower as can be seen in figure 9 of [*Vermeersen et al.*, 1997]. This shows the impact a change in the lower mantle viscosity has on present-day TPW, which is larger in the lower regions of mantle viscosity until about $3 \cdot 10^{21} Pas$. The lower mantle viscosity determines for a large part the viscous behaviour of a planet and thus how fast the Earth can return to its original isostatic equilibrium and thus the damping of TPW motion. This effect is visible in the long-term TPW trend that appears as a result of the long glaciation phase followed by a short deglaciation phase. After an ice-cycle is completed the Earth is still out of isostatic equilibrium and the long-term linear trend appears. This trend is mainly dependent on the lower mantle viscosity which is visible in the relaxation times of some viscoelastic modes, which are longer than an ice-cycle period of 100 kyr. The lower upper mantle viscosity has only a negligible effect on the predicted present-day TPW-speed.

- The TPW-path of ICE-3G(VM1) is directed 7° more West than ICE-5G(VM2). This shift is caused in ICE-3G(VM1) by a relatively larger predicted present-day TPW-speed towards 90°W than the predicted present-day TPW-speed towards Greenwich. This is the result of the ice at LGM which is, in case of ICE-3G, more equally distributed over the West and East Hemisphere as result of relatively more mass at the Antarctica ice sheet and less mass on the Laurentide ice sheet with respect to ICE-5G (see figure 6.8).

ICE-5G(VM2) and RSES(KL)

When the results of the recent ICE-5G(VM2) and RSES(KL) models are investigated there are also some interesting phenomena to observe.

- The present-day TPW-speed of the ICE-5G(VM2) model is 52 percent higher in comparison to the RSES(KL) model. From table 7.4 it appears that the ice models ICE-5G and RSES almost have the same response when the same Earth model is used. This difference is not caused by the ice model without Earth model, but the difference is mainly the result of the different Earth models used as can be seen in figure 7.9 and table 7.3. The large difference in the mantle viscosity of both VM2 and KL is the result of slightly different observational data and the very different a priori model which was used for the refinement. The small difference in the predicted present-day TPW-speed could also be the result of the difference in the ice model, because ICE-5G has a slightly slower melting of the ice at the middle of the deglaciation period as can be seen in figure 6.6.
- The present-day TPW-path is nearly the same because the ice with respect to the axis towards Greenwich and 90 °W is nearly equally distributed. Where ICE-5G has more

ice on the East Laurentide and Fennoscandia/Barentsz Sea, the RSES ice model has more ice on West North America as can be seen in figure 7.11.

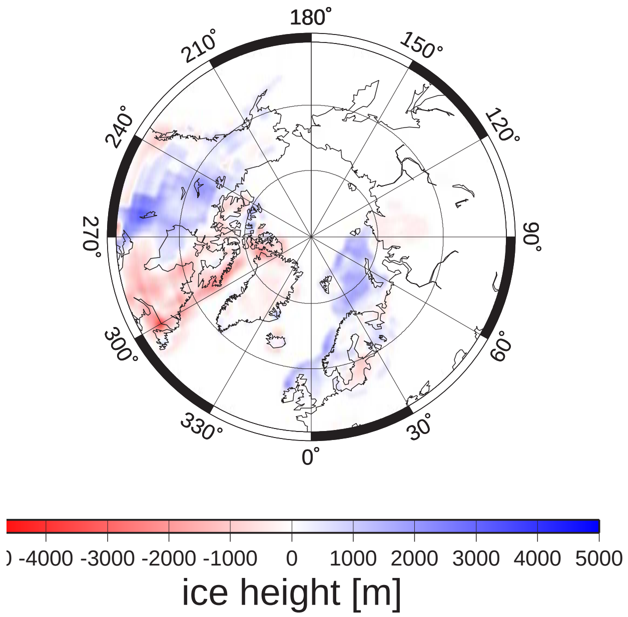

Figure 7.11 Difference in ice height between the ICE-5G and RSES ice model. Blue represents the presence of more ice in the ICE-5G model and red in the RSES model.

ICE-3G(VM1) and RSES(KL)

The predictions for TPW for the ICE-3G(VM1) and RSES(KL) model also have some distinct difference, especially the predicted present-day TPW-path.

- The predicted present-day TPW-speed differs about 10 percent. Firstly this can be the result of the 25 till 30 percent more ice mass of RSES at LGM which leads to a higher present-day TPW-speed. Secondly this can be the result of the higher lower mantle viscosity of the KL Earth model, which is responsible for a 40 till 45 percent lower present-day TPW-speed as can be seen in figure 9 of [*Vermeersen et al.*, 1997].
- As mentioned before the RSES and ICE-5G ice models are the quite similar and produce the same present-day TPW-path as a result of the similar effect of ice distribution on the present-day TPW-path. So in case of ICE-3G the ice is more equally distributed over the West and East Hemisphere as a result of relatively more mass at the Antarctica ice sheet and less mass on the Laurentide ice sheet with respect to RSES (see figure 6.8).

7.3.3 TPW and lower mantle viscosity

As mentioned earlier TPW is highly dependent on the lower mantle viscosity. In this section only the lower mantle viscosities of the used Earth models are changed and the rest of the viscosity stratification is unadapted. The result is presented in figure 7.12. More research on this dependency has been done by [*e.g., Sabadini and Vermeersen*, 2004; *Peltier*, 1996]. When the used models are split in an Earth and ice model, the ice model is considered to have the strongest influence on the predicted TPW-speed apart from the varying lower mantle viscosity. The influence of the Earth model, not considering the lower mantle viscosity, is negligible. In this case the total mass of the ice and its distribution determines the magnitude of the present-day TPW, as was also the case with the simulation of TPW with similar Earth model discussed in section 7.3.2.

The recent developments in ice models and reference frame will have impact on a lower mantle inversion. Although it is trivial to draw conclusions from the use of recent ice models on the lower mantle viscosity, because the ice models were created with the Earth

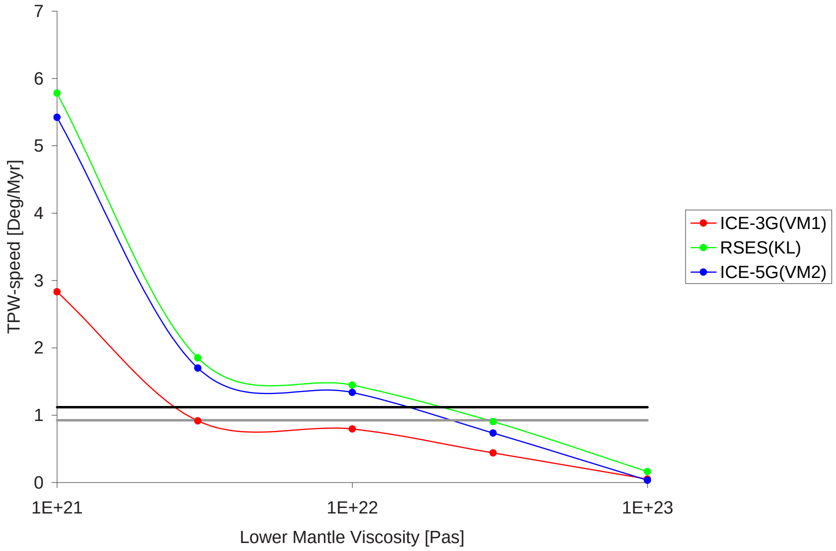

Figure 7.12 Dependency of TPW-speed on different lower mantle viscosities of different models. The gray line depicts the observed present-day TPW, with a value of 0.925 $^{\circ}Myr^{-1}$, as given by *McCarthy and Luzum* [1996] and the black line gives the observed present-day TPW, with a value of 1.12 $^{\circ}Myr^{-1}$, as given by *Argus and Gross* [2004].

models. When the hotspot reference frame is used instead of the predictions by [*McCarthy and Luzum*, 1996] for a mantle inversion from present-day TPW data, a significant change in lower mantle viscosity can be observed. For the ICE-5G(VM2) and RSES(KL) model this gives about a 40 percent lower lower mantle viscosity and about 20 percent lower lower mantle viscosity for ICE-3G(VM1).

Relative to older research [*e.g.*, *Sabadini and Vermeersen*, 2004] the qualitative behaviour of the TPW-speed with respect to the lower mantle viscosity of ICE-3G(VM1) is the same. But the value of the TPW-speed itself is somewhat different when comparing with [*Sabadini and Vermeersen*, 2004], especially with respect to the crossing of the predictions and the observations. This is the result of a different forcing, namely a different eustatic sea level change and ice distribution at LGM. Beside different Earth and ice models also the number of layers, depth of the boundary between the lower and upper mantle and the upper mantle viscosity have influence of the TPW-speed as a function of the lower mantle viscosity [*Vermeersen et al.*, 1997].

7.4 Discussion

In this section a qualitative investigation is performed on previous mantle inversion research, which uses TPW observations as a constraint. It is examined if recent developments (new ice models and the hotspot-reference frame) will have effect on the results and conclusions drawn in previous studies.

Vermeersen et al. [1998] performed a mantle viscosity inversion using, at that time, a new SLR analysis and observed present-day TPW. In this study the SLR data of four geodetic satellites was used over a time span of 14 years to obtain the zonal components of the geopotential (J_n). The observational present-day TPW-speed value of $0.925 \pm 0.022\,^{\circ}Myr^{-1}$ used in this study is taken from *McCarthy and Luzum* [1996] and uses an average lithosphere frame. In this study the ICE-3G ice model and a radial density and rigidity stratification, including an elastic lithospheric thickness of 120 km is used. For a 2-layer viscosity model this resulted in an upper mantle viscosity in the range of $10^{20} Pas$ to a few times $10^{20} Pas$ and a lower mantle viscosity of $5 \cdot 10^{21} Pas$ when the TPW observation is included. Uneven and even harmonics of the geopotential give different results for the lower mantle viscosity, which could be the result of inaccuracies in the deglaciation history of ICE-3G and other

forcings.
But what are the consequences if a recent ice model (ICE-5G or RSES) or the observed present-day TPW-speed relative to the hotspot reference frame ($1.12\,^{\circ}Myr^{-1}$) is assumed? In general the recent ice models account for more ice mass melted during the last deglaciation (25 to 30 percent) and a different distribution of ice which can result in an even larger present-day TPW-speed (till 200 percent) as can be seen in table 7.4.
Firstly a higher present-day TPW-speed will be expected when more ice mass is present at LGM, which will result after mantle inversion in a higher lower mantle viscosity.
Secondly a larger observed present-day TPW-speed will constrain the lower mantle after a mantle inversion to a lower viscosity. These results contradict each other, but it is assumed that the ice model has a larger influence on the lower mantle viscosity and so it is expected that the lower mantle viscosity will increase. This would be in better agreement with the results of even/uneven harmonics of the geopotential change without taken into account the present-day TPW-speed.

In the research done by *Vermeersen et al.* [1997] the rotational response of the Earth to Pleistocene deglaciation is studied by means of a multilayered viscoelastic Earth model. In this study a simplification is used, namely the ice and water distribution is redistributed eustatically over the oceans. A forward simulation is performed using the ICE-3G ice model regarding both the second-degree component of the geopotential ($\dot{J}_2$) and the present-day TPW-speed. The mantle viscosity is constrained by comparing the simulations and the observations from *McCarthy and Luzum* [1996] of both present-day TPW-speed and $\dot{J}_2$. In this research the present-day TPW-speed and $\dot{J}_2$ is plotted against the lower mantle viscosity and compared directly with the observed present-day TPW-speed and $\dot{J}_2$. The lower mantle viscosity is determined from the area where the observed and simulated present-day TPW and $\dot{J}_2$ cross. In this way also the depth of viscosity contrast and upper mantle viscosity is examined. For a 2-layer viscosity model this results in an upper mantle viscosity of 1 till $5 \cdot 10^{20} Pas$ and a lower mantle viscosity of 2.5 till $4 \cdot 10^{21} Pas$. A higher observed TPW-speed has some important consequences for the interpretation of the results as performed by *Vermeersen et al.* [1997] and results in a decrease in lower mantle viscosity. When a recent ice model is used, that contains more ice mass and has a different distribution of ice, this would lead to a significant increase in present-day TPW-speed, as can be seen in figure 7.12.

The results of two important mantle viscosity inversion studies are used in this study, namely the studies of *Peltier* [1998] who derived the VM2 model and *Kaufmann and Lambeck* [2002] who derived the so-called Kaufmann-Lambeck model. These mantle viscosity stratifications were both constrained by the observed present-day TPW-path for an average plate motion [*McCarthy and Luzum*, 1996]. If the higher observed present-day TPW-speed is used as a constraint in the inference of the mantle viscosity this will most likely result in a lower lower mantle viscosity for both models.

In general the mantle viscosity inversion studies are somewhat biased because usually an ice model, which is most likely based on an Earth model and observations, is used together with new observations to place inferences on the mantle viscosity. If the observations are the same, the Earth model which was used to construct the ice model will be the outcome of the investigation. Even though the mantle viscosity inversion study provides more insight in the behaviour of the Earth it should be used with care. An alternative solution is to use an ice-dynamical model (e.g. IMAU-model from the University of Utrecht [*Bintanja et al.*, 2002]) where the influence of an Earth model is much lower. This ice model is based as much as possible on independent information such as geomorphical evidence (e.g. glacial moraines and erratic boulders) and glacialogical model constraints.

Chapter 8

Conclusions and Recommendations

In this study the effect of changes in the rotation vector are implemented in an existing model that solves the sea level equation. This model is used to perform a sensitivity analysis of different ice-load histories on glacial isostatic adjustment (GIA) induced rotational changes. The prediction of the rotation observables are tested against the rotation observations in the hotspot reference frame. Further the model is used to investigate if recent developments in the area of ice models and the hotspot reference frame impose any possible changes in the results and conclusions of older mantle inversion research. Section 8.1 summarizes the most important conclusions. Recommendations for further research on the thesis subject are formulated in section 8.2

8.1 Conclusions

From this research the following conclusions can be drawn:

- The traditional rotation theory has been successfully implemented in the existing code that calculates the sea level equation. This is done self-consistently, i.e. the effect on the potential field of the induced changes in the rotation vector was taken into account in the computation of the induced changes. The results of this model are verified firstly by a benchmark of the perturbation of inertia and the rotational parameters and secondly by a comparison of the predicted TPW with TPW from older publications.
- The assumption of a linear glaciation phase in a saw-tooth ice-loading, which is frequently used in older research, is very reasonable and causes minor differences in the predicted present-day TPW in relation to a more detailed glaciation model.
- The predicted TPW observables of recent ice models and the present-day TPW observations in the hotspot reference frame can differ significantly. The ICE-3G ice model has a difference of 20 percent, the RSES ice model shows a relative small discrepancy of about 10 percent and the ICE-5G model has a larger difference of 60 percent. This difference is most likely caused by the fact that compressibility is not taken into account, other forcings are neglected and possible recent deglaciation events are not included. The fact that TPW data is used to construct these ice models could bias the outcome of this result.
- The use of recently developed ice models and the hotspot reference frame has a significant effect on the results and conclusions of older mantle inversion research. For most mantle inversion studies this will result in a stratification with a lower lower mantle viscosity, which can be as large as 20 to 40 percent.

8.2 Recommendations

The recommendations for this research are:

- It is advised to continue the benchmark of the sea level equation for a rotating Earth beyond the comparison of perturbation of inertia and rotational parameters. Further benchmarking should be focused on comparing the perturbation of inertia as a result of both ice and sea load followed by a comparison of RSL predictions at certain sites.
- A compressible Earth model is preferred, because in case of low lower mantle viscosities this can have a large impact on the predicted present-day TPW.
- The revised rotation theory should be implemented in the sea level equation for a rotating Earth to remove the inaccuracy introduced by the traditional rotation theory. The derivation of the revised rotation theory from the Laplace domain to the time domain should be continued, to allow for the implementation of the theory into the sea level equation for a rotating Earth.
- More studies could be done on the present-day TPW caused by other forcings than GIA, like tectonic processes associated with mountain building, subduction of oceanic lithosphere and mantle convection. When the effects of these forcings are known a better estimate of the TPW observables as a result of GIA can be given. With these better estimates of the TPW observables the mantle viscosity can be better constrained.
- It would be interesting to perform a new mantle viscosity inference research in combination with a new ice model and the TPW observations in the hotspot reference frame, as the use of a different reference frame can have a large impact on the mantle viscosity inversion.
- An ice-dynamical model could be used that is based on as much as possible Earth-model independent information such as geomorphical evidence (e.g. glacial moraines and erratic boulders) and glacialogical model constraints, because the used ice models are created using certain Earth models which make the conclusions sometimes biased.

Appendix A

Benchmark comparisons

The Fortran codes are tested with other codes to verify the correctness by using the same input and comparing the results. Two separate benchmarks were done. In the first benchmark the perturbation of inertia was tested (section A.1), in the second benchmark some rotational parameters were tested (section A.2)

A.1 Perturbation of inertia

The benchmark of the perturbation of inertia is done in cooperation with Dr. Jan Hagedoorn at GeoForschungsZentrum Potsdam who developed, together with Professor Zdeněk Martinec, a code to calculate the rotational response of a viscoelastic Earth directly in the time domain [*Martinec and Hagedoorn*, 2005]. This rotational theory is still under development and is developed until the forward computation of the perturbation of inertia from surface and internal loading.

A.1.1 Model parameters

Earth model
The Earth model is a spherically symmetric, self-gravitating, incompressible, Maxwell viscoelastic 4 layer Earth model also used by *Martinec and Hagedoorn* [2005]. The elastic structure is a simplified version of the original PREM model (see table A.1).

layer	radius $[km]$	density $[kg/m^3]$	rigidity $[N/m^2]$	viscosity $[Pas]$	description
1	6371 - 6271	4449.4	$0.67 \cdot 10^{11}$	elastic	lithosphere
2	6271 - 5701	4449.4	$1.4519 \cdot 10^{11}$	$5 \cdot 10^{20}$	upper mantle
3	5701 - 3480	4449.4	$1.4519 \cdot 10^{11}$	$1 \cdot 10^{22}$	lower mantle
4	3480 - 0	10986.9	0.00	0.00	inviscid fluid core

Table A.1 4 layer Earth model used for perturbation of inertia benchmark.

Load history
The ice model is based on the global ICE-3G deglaciation history (discussed in section 6.2.1). A 100 kyr glaciation phase is assumed and the maximum extent is scaled with RSL from far-field sites. The data is irregularly spread in time as result of the transformation from uncalibrated years to uncalibrated years, in which the data was originally given. These ice heights are linearly interpolated with time steps of 10 years. Also fixed coastlines are assumed.

Topography
The topography file is based upon the ETOPO5 global topography in a Gaussian grid of

512 x 1024 points. ETOPO5 is a global elevation database with a horizontal resolution of five minutes (about 9 km at the equator) in latitude and longitude.

A.1.2 Output

Due to lack of computation power the ice heights are not linearly interpolated and the ice height on the given times are used for the simulation. For the direct perturbation of inertia as result of ice and sea load only an average difference of 0.4 percent was found, despite of the fact that no linear interpolation of the ice heights was used.

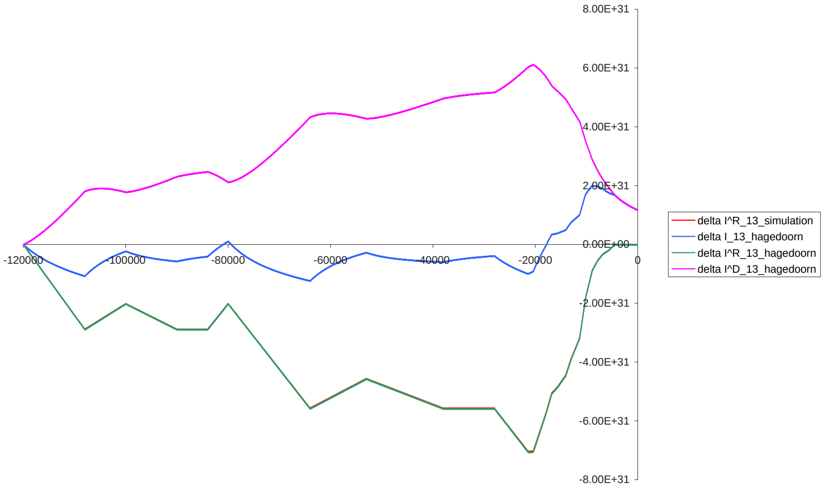

Figure A.1 Perturbation of inertia of degree 1 and order 3, where δI^R of the simulation and Hagedoorn are almost on top of each other.

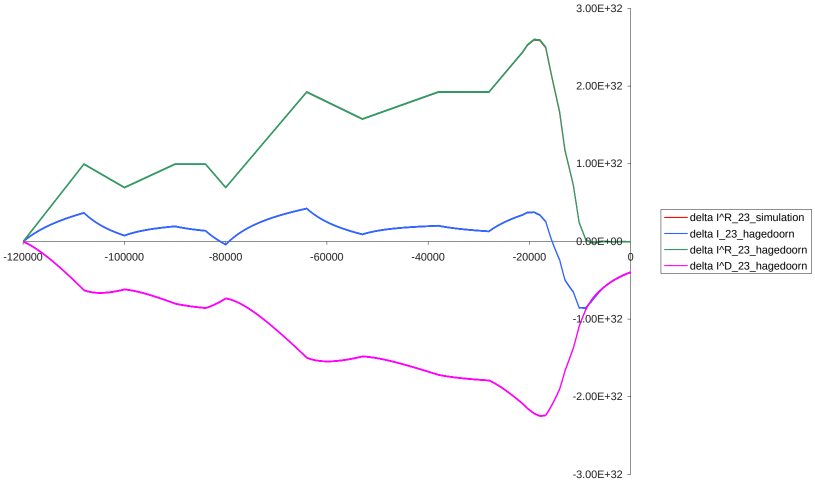

Figure A.2 Perturbation of inertia of degree 2 and order 3, where δI^R of the simulation and Hagedoorn are almost on top of each other.

A.2 Rotational parameters

The benchmark of the rotational parameters is done together with Dr. Glenn Milne from the University of Durham who developed the theory on which the self-consistent implementation of rotation in the sealevel code is based [*Milne and Mitrovica*, 1998].

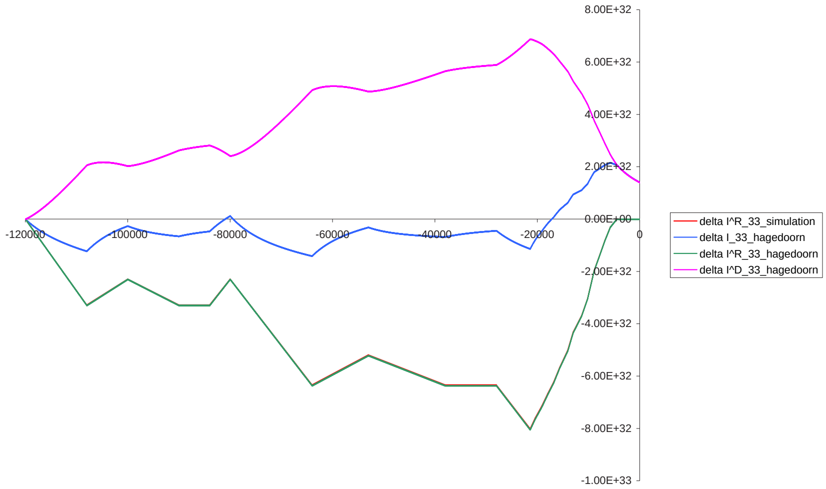

Figure A.3 Perturbation of inertia of degree 3 and order 3, where δI^R of the simulation and Hagedoorn are almost on top of each other.

A.2.1 Model parameters

Earth model

For the benchmark we assume a Maxwell viscoelastic, incompressible, self-gravitating Earth model. Further a 5 layer fixed boundary model (based on PREM) will be used with a viscosity contrast at 670 km and a lithosphere thickness of 100 km as shown in table A.2.

layer	radius $[km]$	density $[kg/m^3]$	rigidity $[N/m^2]$	viscosity $[Pas]$	description
1	6371 - 6271	4120	$7.28 \cdot 10^{10}$	elastic	lithosphere
2	6271 - 5951	4120	$9.54 \cdot 10^{10}$	$1 \cdot 10^{21}$	shallow upper mantle
3	5951 - 5701	4220	$1.10 \cdot 10^{11}$	$1 \cdot 10^{21}$	transition zone
4	5701 - 3480	4508	$1.99 \cdot 10^{11}$	$2 \cdot 10^{21}$	lower mantle
5	3480 - 0	10925	0.00	0.00	inviscid fluid core

Table A.2 5 layer Earth model used for benchmark.

Load history

The loading history is represented by a simplified parabolic ice sheet on Greenland with a radius of 10 degrees (see figure A.4) which instantaneously melts at 10 kyr before present.

Topography

The topography file is based upon the ETOPO2 global topography in a Gaussian grid of 512 x 1024 points. ETOPO2 is a global elevation database and is the successor of ETOPO5 and has an increased resolution of two minutes (about 4 km at the equator) in latitude and longitude.

A.2.2 Output

Glenn Milne uses a method which is capable of calculating the Love numbers for a compressible Earth instead of an incompressible Earth as in Delft. Problems arose when he tried to calculate the Love numbers for an incompressible Earth. It was decided to directly use the Love numbers calculated in Delft, because the intention was not to verify the Love number calculation routine. The rotational parameters correspond nicely as can be seen in table A.3. It must be noted that Milne scales his Love numbers by dividing with the corresponding degree, in first instance this gave a discrepancy but was solved afterward.

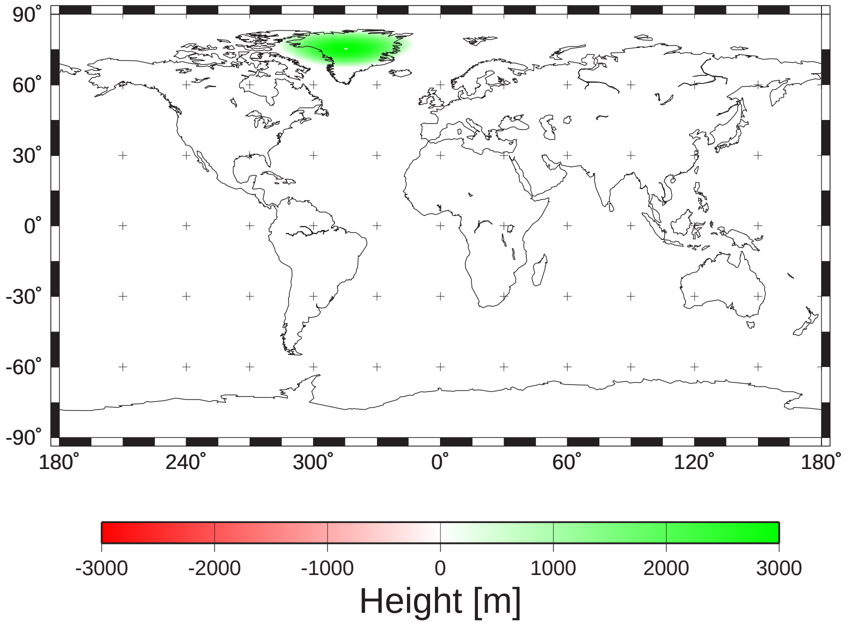

Figure A.4 Ice load-distribution on Greenland at LGM.

Unfortunately due to lack of time on the side of Glenn Milne the benchmark was stopped at this point. Further benchmarking should be focused on comparing the perturbation of inertia as result of both ice and sea load followed by a comparison of RSL predictions at certain sites.

parameter	Milne	Delft
λ_1	$1.360012868110 \cdot 10^{-5}$	$1.360012733618 \cdot 10^{-5}$
λ_2	$1.901739492600 \cdot 10^{-3}$	$1.901739560344 \cdot 10^{-3}$
λ_3	$9.057738235687 \cdot 10^{-2}$	$9.057738276403 \cdot 10^{-2}$
λ_4	0.618301272958	0.618301290392
λ_5	3.015297746428	3.015297751653
λ_6	3.042085759717	3.042085769663
λ_7	3.435453527906	3.435453611664
λ_8	3.461576155423	3.461576091314
E_1	$2.1955395 \cdot 10^{-2}$	$2.1955390 \cdot 10^{-2}$
E_2	0.1834799	0.1834799
E_3	$4.2494338 \cdot 10^{-2}$	$4.2494332 \cdot 10^{-2}$
E_4	0.2604155	0.2604155
E_5	$3.9907576 \cdot 10^{-5}$	$3.9904058 \cdot 10^{-5}$
E_6	$8.9070236 \cdot 10^{-6}$	$8.9003609 \cdot 10^{-6}$
E_7	$8.2485050 \cdot 10^{-5}$	$8.2426382 \cdot 10^{-5}$
E_8	$1.7363449 \cdot 10^{-4}$	$1.7367961 \cdot 10^{-4}$
ℓ_s	0.5097450	0.5097450
D_1	0.8689550	0.8689550
D_2	$2.6085360 \cdot 10^{-2}$	$2.6085358 \cdot 10^{-2}$

Table A.3 Results comparison.

Bibliography

Argus, D.F., and R.S. Gross (2004), An estimate of motion between the spin axis and the hotspots over the past century, *Geophys. Res. Lett.*, *31*, L06614.

Bintanja, R., R.S.W. van de Wal, and J. Oerlemans (2002), Global ice volume variations through the last glacial cycle simulated by a 3-d ice-dynamical model, *Quart. Int.*, *95–96*, 11–23.

Biot, M.A. (1954), Theory of stress-strain relations in anisotropic viscoelasticity and relaxation phenomena, *J. of Appl. Phys.*, *97*, 1463.

Dahlen, F.A. (1976), The passive influence of the oceans upon rotation of the Earth, *Geophys. J.R. Astron. Soc.*, *46*, 363–406.

Dziewonski, A.M., and D.L. Anderson (1981), Preliminary Reference Earth Model, *Phys. Earth Planet. Int.*, *25*, 297–356.

Farrell, W.E., and J.A. Clark (1976), On postglacial sea-level, *Geophys. J. Int.*, *46*, 647–667.

Forno, G.D., P. Gasperini, and E. Boschi (2005), Linear or nonlinear rheology in the mantle: a 3D finite-element approach to postglacial rebound modeling, *J. Geodyn.*, *39*, 183–195.

Gasperini, P., and R. Sabadini (1989), Lateral heterogeneities in mantle viscosity and post-glacial rebound, *Geophys. J. Int.*, *98*, 413–428.

Gasperini, P., R. Sabadini, and D.A. Yuen (1986), Excitation of the earth's rotational axis by recent glacial discharges, *J. Geophys. Res.*, *13*, 533–536.

Gross, R.S. (1997), A combination of eop measurements: Space96, in *1996 IERS Annual Report, Observatoire de Paris*, p. II29.

Gross, R.S. (2000), The excitation of the Chandler wobble, *Geophys. Res. Lett.*, *27*, 2329–2332.

Gross, R.S. (2002), Combinations of Earth Orientation Measurements: SPACE2001, COMB2001, and POLE2001, *NASA STI/Recon Technical Report*, *2*, 45.389.

Gross, R.S., and J. Vondrák (1999), Astrometric and space-geodetic observations of polar wander, *Geophys. Res. Lett.*, *26*, 2085–2088.

Han, D., and J. Wahr (1989), Post-Glacial rebound analysis for a rotating Earth in *Slow Deformations and Transmission of Stress in the Earth*, eds., Cohen S. and Vanicek, P., *AGU Mono*, *49*, 1–6.

Heiskanen, W.A., and H. Moritz (1967), *Physical geodesy*, Freeman, San Francisco.

Hilst, R.D. van der, R.S. Widiyantoro, and R. Engdahl (1997), Evidence for deep mantle circulation from global tomography, *Nature*, *386*, 578–584.

Imbrie, J., and K.P. Imbrie (1979), *Ice Ages: Solving the Mystery*, Enslow Publishers, Hillside, New Jersey, United States of America.

Karato, S. (1989), Plasticity-crystal structure systematics in dense oxides and its implications for the creep strength of the Earth's deep interior: a preliminary result, *Phys. Earth Planet. Inter.*, *55*, 234–240.

Kaufmann, G., and K. Lambeck (2002), Glacial isostatic and the radial viscosity profile from inverse modeling, *J. Geophys. Res.*, *107*, B11.

Kaufmann, G., and D. Wolf (2005), Effects of lateral viscosity variations on postglacial rebound: an analytical approach, *Geophys. J. Int.*, *137*, 489–500.

Lambeck, K. (1980), *The Earth's Variable Rotation: Geophysical Causes and Consequences*, Cambridge University Press, Cambridge, United Kingdom.

Lambeck, K. (1988), *Geophysical Geodesy, the Slow Deformations of the Earth*, Oxford University Press, New York.

Lambeck, K. (1998), Sea-level change, glacial rebound and mantle viscosity for northern Europe, *Geophys. J. Int.*, *134*, 102–144.

Lee, E.H. (1989), Stress analysis in viscoelastic bodies, *Quart. of Appl. Math.*, *13*, 183.

Martinec, Z. (1999), Spectral, initial value approach for a viscoelastic relaxation of a spherical earth with a three-dimensional viscosity - I. Theory, *Geophys. J. Int.*, *137*, 469–488.

Martinec, Z., and J. Hagedoorn (2005), Time-domain approach to linearized rotational response of a three-dimensional viscoelastic earth model induced by glacial-isostatic adjustment : I. inertia-tensor perturbations, *Geophys. J. Int.*, *163*, 443–462.

McCarthy, D.D., and B.J. Luzum (1996), Path of the mean rotational pole from 1899 to 1994, *Geophys. J. Int.*, *125*, 623–629.

Melosh, H.J. (1980), Cratering mechanics: Observational, experimental and theoretical, *Ann. Rev. Earth Planet. Sci.*, *8*, 65–93.

Milne, G.A., and J.X. Mitrovica (1998), Postglacial sea level change on a rotating Earth, *Geophys. J. Int.*, *133*, 1–19.

Milne, G.A., Mitrovica J.X., and J.L. Davis (1999), Near-field hydro isostacy: the implementation of a revised sea-level equation, *Geophys. J. Int.*, *139*, 464–482.

Milne, G.A., J.L Davis, J.X. Mitrovica, H.G. Scherneck, J.M. Johansson, M. Vermeer, and H. Koivula (2001), Space-geodetic constraints on glacial isostatic adjustment in Fennoscandia, *Science*, *291*, 2381–2385.

Mitrovica, J.X., and G.A. Milne (1998), Glaciation-induced perturbations in the Earth's rotation: A new appraisal, *J. Geophys. Res.*, *103*, 985–1005.

Mitrovica, J.X., and W.R. Peltier (1991), On postglacial geoid subsidence over the equatorial oceans, *J. Geophys. Res.*, *96*, 20053–20071.

Mitrovica, J.X., G.A. Milne, and J.L. Davis (2001), Glacial isostatic adjustment on a rotating Earth, *Geophys. J. Int.*, *147*, 562–578.

Mitrovica, J.X., J. Wahr, I. Matsuyama, and A. Paulson (2005), The rotational stability of an ice-age earth, *Geophys. J. Int.*, *161*, 491–506.

Mound, J.E. (2005), Electromagnetic torques in the core and the resonant excitation of decadal polar motion, *Geophys. J. Int.*, *160*, 721–728.

Munk, W.H., and G.J.F. MacDonald (1960), *The Rotation of the Earth: A Geophysical Discussion*, Cambridge University Press, Cambridge, United Kingdom.

Nakada, M. (2000), Effect of the viscoelastic lithosphere on polar wander speed caused by the Late Pleistocene glacial cycles, *Geophys. J. Int.*, *143*, 230–238.

Nakada, M. (2002), Polar wander caused by the Quaternary glacial cycles and fluid love number, *Earth Planet. Sci. Lett.*, *200*, 159–166.

Nakiboglu, S. M., and K. Lambeck (1980), Deglaciation effects on the rotation of the earth, *Geophys. J.R. Astron. Soc.*, *62*, 49–58.

Peltier, W.R. (1974), The impulse response of a Maxwell Earth, *Rev. Geophys.*, *12*, 649–669.

Peltier, W.R. (1976b), Glacial isostatic adjustment, II. The inverse problem, *Geophys. J.R. Astron. Soc.*, *46*, 669–706.

Peltier, W.R. (1989), *Mantle viscosity, Mantle Convection, Plate Tectonics and Global Dynamics, pp. 389–478*, Gordon Beach Science Publishers, New York, United States of America.

Peltier, W.R. (1994), Ice age paleotopography, *Science*, *265*, 195–201.

Peltier, W.R. (1995), VLBI baselines from the ICE-4G model of postglacial rebound, *Geophys. Res. Lett.*, *22*, 465–468.

Peltier, W.R. (1996), Mantle viscosity and ice age sheet topography, *Science*, *273*, 1359–1365.

Peltier, W.R. (1998), The inverse problem for mantle viscosity, *Inverse problems*, *14*, 441–478.

Peltier, W.R. (2002), Global glacial isostatic adjustment: palaeogeodetic and space-geodetic tests of the ICE-4G (VM2) model, *J. Quart. Sci*, *17*, 491–510.

Peltier, W.R. (2004), Global glacial isostacy and the surface of the Ice-Age Earth: The ICE-5G (VM2) Model and GRACE, *Ann. Rev. Earth Planet. Sci.*, *32*, 111–149.

Peltier, W.R., and J.T. Andrews (1976a), Glacial isostatic adjustment, I. The forward problem, *Geophys. J.R. Astron. Soc.*, *46*, 605–646.

Peltier, W.R., W.E. Farrell, and J.A. Clark (1978), Glacial isostasy and relative sea level: A global finite element model, *Tectonophys.*, *50*, 81–110.

Peltier, W.R., P. Wu, and D.A. Yuen (1981), *The viscosities of the Earth's mantle, in Anelasticity in the Earth, Geodynamics Series 4, eds. F.D. Stacey, M.S. Paterson and A. Nichols, pp. 59-77*, American Geophysical Union and Geophysical Society of America, Washington, United States of America.

Press, W.H., S.A. Teukolsky, W.T. Vetterling, and B.P. Flannery (1992), *Numerical Recipes in Fortran 77 2nd Edition*, Cambridge University Press, San Francisco.

Ranalli, G. (1995), *Rheology of the Earth*, Chapman and Hall, London, United Kingdom.

Ricard, Y., R. Sabadini, and G. Spada (1992), Isostatic deformations and polar wander induced by redistribution of mass within the earth, *J. Geophys. Res.*, *97,14*, 223–14,236.

Sabadini, R., and W.R. Peltier (1981), Pleistocene deglaciation and the earth's rotation: Implications on mantle viscosity, *Geophys. J.R. Astron. Soc.*, *66*, 573–578.

Sabadini, R., and L.L.A. Vermeersen (2004), *Global Dynamics of the Earth*, Kluwer Academic Publishers, Dordrecht, The Netherlands.

Sabadini, R., D.A. Yuen, and E. Boschi (1982), Polar wandering and the forced responses of a rotating, multilayered, viscoelastic planet, *J. Geophys. Res.*, *87*, 2885–2903.

Sabadini, R., D.A. Yuen, and R. Widmer (1985), Constraints on short-term mantle rheology from the $\dot{J}_2$ observation and the dispersion of the 18.6 y tidal love number, *Phys. Earth Planet. Inter.*, *38*, 235–249.

Schubert, G., D.L. Turcotte, and P. Olson (2001), *Mantle Convection in the Earth and Planets*, Cambridge University Press, Cambridge.

Shackleton, N.J. (2000), The 100.000-year ice-cycle identified and found to lag temperature, carbon dioxide, and orbital eccentricity, *Science*, *289*, 1897–1902.

Shackleton, N.J., and N.D. Opdyke (1976), Oxygen isotope stratigraphy of Pacific core V28-239, *Mem. Geol. Soc. Am.*, *145*, 449–464.

Sneeuw, N. (1994), Global spherical harmonic analysis by least-squares and numerical quadrature methods in historical perspective, *Geophys. J. Int.*, *118*, 707–716.

Steinberger, B. (1998), Plumes in a convecting mantle: Models and observations for individual hot-spots, *J. Geophys. Res.*, *105*, 11.127–11.152.

Steinberger, B., and R.J. O'Connell (1997), Changes of the Earth's rotation axis owing to advection of mantle density heterogeneities, *Nature*, *387*, 169–173.

Steinberger, B., and R.J. O'Connell (1998), Advection of plumes in mantle flow: Implications for individual hot-spots, *Geophys. J. Int.*, *132*, 412–434.

Tarantola, A., and B. Valette (1982), Inverse problems is quest for information, *J. Geopys.*, *50*, 159–170.

Tromp, J., and J.X. Mitrovica (1999), Surface loading of a viscoelastic sphere - I. general theory, *Geophys. J. Int.*, *137*, 847–855.

Tushingham, A.M., and W.R. Peltier (1991), ICE-3G: A new global model of late Pleistocene deglaciation based on geophysical predictions of postglacial relative sea level change, *J. Geophys. Res.*, *96*, 4497–4523.

Vermeersen, L.L.A. (2004), *Geophysical Applications of Satellite Measurements (lecture note)*, Delft Institute for Earth-Oriented Space Research, Delft, The Netherlands.

Vermeersen, L.L.A., and R. Sabadini (1996a), Significance of the fundamental rotational relaxation mode in polar wander simulations, *Geophys. J. Int.*, *127*, F5–F9.

Vermeersen, L.L.A., and R. Sabadini (1999), Polar wander, sea level variations and ice age cycles, *Surv. Geophys.*, *20*, 415–440.

Vermeersen, L.L.A., R. Sabadini, G. Spada, and N.J. Vlaar (1994), Mountain building and earth rotation, *Geophys. J. Int.*, *117*, 610–624.

Vermeersen, L.L.A., R. Sabadini, and G. Spada (1996b), Compressible rotational deformation, *Geophys. J. Int.*, *126*, 735–767.

Vermeersen, L.L.A., A. Fournier, and R. Sabadini (1997), Changes in rotation induced by Pleistocene ice masses with stratified analytical Earth models, *J. Geophys. Res.*, *102*, 27689–27702.

Vermeersen, L.L.A., R. Sabadini, R. Devoti, V. Luceri, P. Rutigliano, C. Sciaretta, and G. Bianco (1998), Mantle viscosity inferences from joint inversions of pleistocene deglaciation-induced changes in geopotential with a new SLR analysis and polar wander, *Geophys. Res. Lett.*, *25*, 4261–4264.

Wang, H., and P. Wu (2006), Effects of lateral variations in lithospheric thickness and mantle viscosity on glacially induced surface motion on a spherical, self-gravitating Maxwell Earth, *Earth Planet. Sci. Lett.*, *244*, 576–589.

Wu, P. (1978), *The response of a Maxwell earth to applied surface mass loads: Glacial isostatic adjustment*, MSc thesis, University of Toronto, Canada.

Wu, P., and W.R. Peltier (1982), Viscous gravitational relaxation, *Geophys. J.R. Astron. Soc.*, *70*, 435–485.

Wu, P., and W.R. Peltier (1983), Glacial isostatic adjustment and the free air gravity anomaly as a constraint on deep mantle viscosity, *Geophys. J.R. Astron. Soc.*, *76*, 753–791.

Wu, P., and W.R. Peltier (1984), Pleistocene deglaciation and the Earth's rotation: A new analysis, *J. Geophys. Res.*, *89*, 11303–11316.

Wu P., Z. Ni, and G. Kaufmann (1998), *Postglacial rebound with lateral heterogeneities: from 2D to 3D modeling, in Dynamics of the Ice Age Earth: A modern perspective, ed. Wu P., pp.557-582*, Trans Tech Publ., Zurich, Switzerland.